

THERMO-MECHANICAL FATIGUE ANALYSIS
OF A STATIONARY JET ENGINE COMPONENT

A THESIS SUBMITTED TO
THE GRADUATE SCHOOL OF NATURAL AND APPLIED SCIENCES
OF
THE MIDDLE EAST TECHNICAL UNIVERSITY

BY

118967

118967

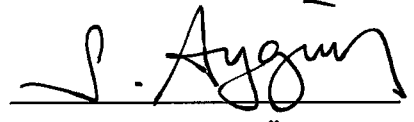
ERDEM ACAR

**T.C. YÜKSEKÖĞRETİM KURULU
DOKÜMANTASYON MERKEZİ**

IN PARTIAL FULFILLMENT OF THE REQUIREMENTS FOR THE DEGREE OF
MASTER OF SCIENCE IN
THE DEPARTMENT OF AERONAUTICAL ENGINEERING

SEPTEMBER 2002

Approval of Graduate School of Natural and Applied Sciences.



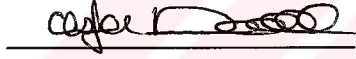
Prof. Dr. Tayfur Öztürk
Director

I certify that this thesis satisfies all the requirements as a thesis for the degree of Master of Science.



Prof. Dr. Nafiz Alemdaroğlu
Head of Department

This is to certify that we have read this thesis and that in our opinion it is fully adequate, in scope and quality, as a thesis for the degree of Master of Science.



Prof. Dr. Mustafa Doruk
Co-Supervisor



Prof. Dr. Mehmet A. Akgün
Supervisor

Examining Committee Members

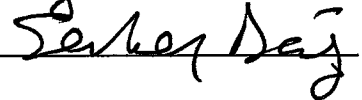
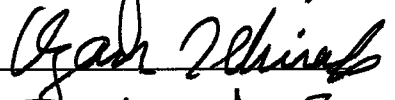
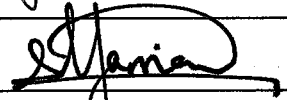
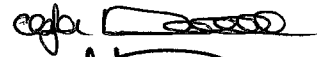
Prof. Dr. Mehmet A. Akgün

Prof. Dr. Mustafa Doruk

Prof. Dr. Yavuz Yaman

Assoc. Prof. Dr. Ozan Tekinalp

Dr. Serkan Dağ



ABSTRACT

THERMO-MECHANICAL FATIGUE ANALYSIS OF A STATIONARY JET ENGINE COMPONENT

Acar, Erdem

M.S., Department of Aeronautical Engineering

Supervisor: Prof. Dr. Mehmet A. Akgün

Co-Supervisor: Prof. Dr. Mustafa Doruk

September 2002, 109 pages

In this thesis, thermo-mechanical fatigue life of a stationary component of F110-GE-100 jet engine is assessed. Two-dimensional axisymmetric finite element model of the component itself, the neighbouring components and also the surrounding gas are generated by using a finite element package program, MARC, in order to perform thermal, stress and fracture mechanics analyses. Thermal analysis is performed to calculate temperature histories of engine components throughout a given mission. Stress analysis is performed to identify fracture-critical locations and to describe stress histories of the components. After determining the critical location, fracture mechanics calculations are performed by modeling a crack of various lengths at the critical location in order to describe crack propagation path and to calculate mode I and II stress intensity factors. Combining the outputs of thermal, stress and fracture mechanics analyses, fatigue lives and creep rupture

times are calculated with a crack growth life prediction program, AFGROW. A linear damage summation method is used to assess thermo-mechanical fatigue life of the component of interest.

Keywords: Thermo-mechanical Fatigue, Creep, Fracture Mechanics, Finite Element Method, High Temperature, Life Assessment



ÖZ

SABİT BİR JET MOTORU PARÇASININ TERMO-MEKANİK YORULMA ANALİZİ

Acar, Erdem

Yüksek Lisans, Havacılık Mühendisliği Bölümü

Tez Yöneticisi: Prof. Dr. Mehmet A. Akgün

Ortak Tez Yöneticisi: Prof. Dr. Mustafa Doruk

Eylül 2002, 109 sayfa


Bu tezde F110-GE-100 jet motorunun sabit bir parçasının termo-mekanik yorulma ömrü hesabı yapılmıştır. Isıl, gerilme ve kırılma mekaniği analizlerini yapmak için, bir sonlu elemanlar paket programı olan MARC kullanılarak parçanın kendisinin, komşu parçaların ve çevredeki gazın iki boyutlu merkezi aksenal simetrik sonlu elemanlar modeli oluşturulmuştur. Belirli bir görev süresince motor parçalarının sıcaklık geçmişini hesaplamak için ısıl analiz yapılmıştır. Kırılma-kritik bölgeleri teşhis etmek ve parçaların gerilme geçmişlerini tanımlamak için gerilme analizi yapılmıştır. Kritik bölgeyi belirledikten sonra, çeşitli uzunluklarda çatlak modelleyerek mod I ve II gerilme gerilme şiddeti faktörleri hesaplamak ve çatlak ilerleme rotasını belirlemek için kırılma mekaniği hesaplamaları yapılmıştır. Isıl, gerilme ve kırılma mekaniği analizlerinin sonuçlarını birleştirerek, bir çatlak ilerleme ömür hesabı programı olan AFGROW ile yorulma ömrü ve sürünme



kopma zamanları hesaplanmıştır. İlgilenilen parçanın termo-mekanik yorulma ömrü hesabı için bir lineer hasar toplama metodu kullanılmıştır.

Anahtar Kelimeler: Termo-mekanik Yorulma, Sürünme, Kırılma Mekanığı, Sonlu Elemanlar Metodu, Yüksek Sıcaklık, Ömür Hesabı





To my family

ACKNOWLEDGEMENTS

I would like to express my sincere appreciation to my thesis supervisor, Prof. Dr. Mehmet A. Akgün for his invaluable support and guidance throughout this study.

I also express my appreciation to my thesis co-supervisor, Prof. Dr. Mustafa Doruk for his support and guidance.

I also want to thank to Dr. Serkan Dağ for his support and guidance in this study.

Special thanks to 1st Air Supply and Maintenance Center, Eskişehir for supplying the required data in this study.

I gratefully thank to my parents and my sister for their great support and understanding over all my life.

Finally I would like to thank to all my friends, especially Bekir Narin, Murat Ilgaz and Özhan Öksüz for their great understanding.

TABLE OF CONTENTS

ABSTRACT	iii
ÖZ.....	v
DEDICATION	vii
ACKNOWLEDGEMENTS	viii
TABLE OF CONTENTS	ix
LIST OF TABLES	xii
LIST OF FIGURES.....	xiii
NOMENCLATURE.....	xv
CHAPTER	
1 INTRODUCTION.....	1
1.1 INTRODUCTION	1
1.2 FAILURE MECHANISMS IN JET ENGINES	2
1.3 ENGINE MONITORING AND LIFING POLICIES	4
1.4 SCOPE OF THE PRESENT WORK	7
1.5 LITERATURE SURVEY.....	7
1.5.1 General Linear Accumulation Damage Models	8
1.5.2 Damage Rate Models.....	8
1.5.3 TMF/SRP Models.....	8
1.5.4 Modified J-Integralmodels.....	9
1.5.5 Empirical Models.....	9
1.6 OUTLINE OF THE THESIS.....	9
2 THERMO-MECHANICAL FATIGUE LIFE PREDICTION.....	10
2.1 INTRODUCTION	10

2.2	FATIGUE LIFE PREDICTION	11
2.2.1	Stress-Life Approach	11
2.2.2	Strain-Life Approach	12
2.2.3	Fracture Mechanics Approach	14
2.2.3.1	Loading Modes	16
2.2.3.2	Stress Intensity Factor	17
2.2.3.3	Fatigue Crack Growth Curves	17
2.2.3.4	Mixed Mode Fatigue Crack Growth	19
2.2.3.5	Prediction of Mixed Mode Crack Growth Directions	20
2.2.3.6	Prediction of Mixed Mode FCGR	21
2.2.4	Variable Amplitude Loading	23
2.2.4.1	Cycle Counting	23
2.2.4.2	Damage Summing Method for Stress-Life Approach	26
2.2.4.3	Damage Summing Method for Strain-Life Approach	27
2.2.4.4	Crack Propagation Under Variable Amplitude Loading	27
2.3	CREEP LIFE PREDICTION	32
2.4	THERMO-MECHANICAL FATIGUE LIFE PREDICTION	36
2.4.1	General Linear Accumulation Damage Models	36
2.4.2	Damage Rate Models	40
2.4.3	TMF/SRP Models	44
2.4.4	Modified J-Integral Models	45
2.4.5	Empirical Models	46
3	THERMAL AND STRESS ANALYSIS	47
3.1	INTRODUCTION	47
3.2	DESCRIPTION OF THE STRUCTURE ANALYZED	47
3.3	FINITE ELEMENT METHOD	51
3.4	THERMAL ANALYSIS	52

3.5 STRESS ANALYSIS	56
4 FRACTURE MECHANICS CALCULATIONS BY FEM AND LIFE ASSESSMENT	59
4.1 INTRODUCTION	59
4.2 USE OF QUARTER POINT ELEMENTS	59
4.3 CALCULATION OF SIF BY FEM	60
4.3.1 Displacement Correlation Technique (DCT).....	61
4.3.2 Quarter Point Displacement Technique (QPDT).....	62
4.3.3 Displacement Extrapolation Technique (DET)	63
4.4 FRACTURE MECHANICS MODELS GENERATED.....	63
4.5 TMF LIFE PREDICTION BY AFGROW	67
5 CONCLUSION	73
REFERENCES	75
APPENDICES	
A CALCULATION OF CONVECTIVE VELOCITIES GIVEN TO THE BLADE NODES.....	81
B CORRECTION FACTOR FOR MODULUS OF ELASTICITY OF THE BLADES IN AN AXISYMMETRIC MODEL	86
C CALCULATION OF THE SPRING STIFFNESSES AT THE MODEL INTERFACE.....	89
D CREEP CRACK GROWTH DATA EXTRAPOLATION.....	94
E TEMPERATURE AND PRESSURE VALUES OF GAS STREAM, COOLING AIR, AND CRITICAL LOCATION	98

LIST OF TABLES

TABLE

4.1	Fatigue Life Prediction Results	68
4.2	Hold Periods	70
4.3	Creep Rupture Time Results	71
4.4	TMF Life Prediction Results	72
E.1	Numerical Values of the Temperature Profile of Gas Stream Entering LPT Stator Vanes	102
E.2	Numerical Values of the Temperature Profile of Gas Stream Leaving LPT Stator Vanes	103
E.3	Numerical Values of the Temperature Profile of Cooling Air Impinging on LPT Stator Vanes	104
E.4	Numerical Values of the Total Pressure Profile of Gas Stream Entering LPT Stator Vanes	105
E.5	Numerical Values of the Total Pressure Profile of Gas Stream Entering LPT Stator Vanes	105
E.6	Numerical Values of the Temperature Profile of Cooling Air Impinging on LPT Stator Vanes	107
E.7	Numerical Values of the Temperature Profile of the Critical Location.....	108
E.8	Numerical Values of the Maximum Principal Stress Profile of the Critical Location	109

LIST OF FIGURES

FIGURES

2.1	Initiation and Propagation Portions of the Fatigue Life	15
2.2	Three Loading Modes.....	17
2.3	Three Regions of Crack Growth Rate Curve	18
2.4	Polar Stress Components in a Stress Element Near a Crack Tip	20
2.5	An Irregular Fatigue Loading History	23
2.6	Rain-flow Cycle Counting Applied to History of Fig. 2.5	24
2.7	Fatigue Loading History Composed of Blocks of Constant Amplitude Cycles	25
2.8	Use of a Constant Amplitude S-N Curve with the Palmgren-Miner Rule	26
2.9	Crack Growth Retardation After an Overload.....	28
2.10	Plastic Zone Parameters Used in Wheeler and Willenborg Models.....	29
2.11	A Typical Strain vs. Time Curve at a Constant Stress at Elevated Temperature.....	33
2.12	SRP Cycle Types Showing (a) pp Type, (b) cp Type, (c) pc Type, and (d) cc Type	44
3.1	Low Pressure Turbine Assembly.....	48
3.2	First Stage LPT Nozzle Outer Band and Impingement Cover	50
3.3	Nozzle, Nozzle Support and Pin.....	50
3.4	The Pin.....	51
3.5	Finite Element Mesh of the Components and Velocity Vectors of Surrounding Gas	53
3.6	Temperature Distribution when $EPLA = 130^\circ$	56
3.7	Springs Simulating the Parts not Modeled	58

4.1	Local Coordinates Measured from a 2-D Crack Front.....	61
4.2	Nodal Lettering for SIF Computations.....	62
4.3	The Critical Location from Where a Crack is Expected to Initiate.....	64
4.4	Maximum Principal Stress Profile of the Critical Location.....	65
4.5	Maximum Effective SIF Variation with Crack Length.....	66
4.6	β Factor Variation with Crack Length.....	66
4.7	Crack Growth Direction Changing with Time.....	67
4.8	Fatigue Crack Growth Curves.....	69
A.1	3-D Finite Element Mesh.....	82
A.2	Temperature Distribution in the Midplane of the Plate.....	82
A.3	2-D Axisymmetric Finite Element Mesh.....	83
A.4	Temperature Distribution in the Midplane of the Plate with Convective Velocity Given to the Plate Nodes.....	84
A.5	Temperature Distribution of the Plate with No Convective Velocity Given to the Plate Nodes.....	85
C.1	First Stage and Second Stage LPT Support.....	91
C.2	Impingement Cover Laid Out Flat.....	93
D.1	Hold Time (t_h) in an Arbitrary Stress Profile.....	94
D.2	Creep Crack Growth Curves for Inconel 718 at 800 K, 866 K, and 922 K.....	96
D.3	Temperature History of the Critical Location.....	97
D.4	Creep Crack Growth Curves Obtained by Linear Extrapolation.....	97
E.1	Temperature Profile of Gas Stream Entering LPT Stator Vanes.....	99
E.2	Temperature Profile of Gas Stream Leaving LPT Stator Vanes.....	99
E.3	Temperature Profile of Cooling Air Impinging on LPT Outer Band.....	100
E.4	Total Pressure Profile of Gas Stream Entering LPT Stator Vanes.....	100
E.5	Total Pressure Profile of Gas Stream Leaving LPT Stator Vanes.....	101
E.6	Total Pressure Profile of Cooling Air Impinging on LPT Outer Band.....	101

NOMENCLATURE

CCGR	: Creep Crack Growth Rate
FCGR	: Fatigue Crack Growth Rate
FEA	: Finite Element Analysis
FEM	: Finite Element Method
HCF	: High Cycle Fatigue
IP	: In-Phase
LCF	: Low Cycle Fatigue
LEFM	: Linear Elastic Fracture Mechanics
NDI	: Non-Destructive Inspection
OP	: Out-of-Phase
SIF	: Stress Intensity Factor
SRP	: Strain Range Partitioning
TMF	: Thermo-Mechanical Fatigue
β	: Geometry Factor
E	: Modulus of Elasticity
G	: Shear Modulus
K	: Stress Intensity Factor
K_{IC}	: Plain Strain Fracture Toughness
ν	: Poisson's Ratio

Other variables are defined where they first appear within the text.

CHAPTER 1

INTRODUCTION

1.1 INTRODUCTION

A jet engine is a complex system composed of many different components, which operate in a very harsh and damaging environment. The components are usually subjected to external forces and heat flux whose magnitude and direction vary with time in the operating conditions. Passenger aircraft engines work in nearly steady conditions in each phase of a flight while military aircraft engines work in highly transient conditions due to frequent maneuvers. Hence, the engine components are subjected to constantly changing temperatures and forces. In such hazardous and complex conditions, the components may fail in service, which is unacceptable. Life assessment of engine components is therefore a must.

A thorough understanding of the failure mechanisms affecting jet engine components is essential for life assessment purposes. These failure mechanisms are low cycle fatigue, high cycle fatigue, thermo-mechanical fatigue, creep, corrosion, erosion, fretting and wear.

1.2 FAILURE MECHANISMS IN JET ENGINES

Since the thermal and mechanical loading that the components are subjected fluctuate often in a random manner, it is frequently found that failure occurs at lower stress levels relative to the stress levels expected in case of steady (or constant) loading conditions. This phenomenon is known as fatigue. The process of fatigue is usually divided into two phases; crack initiation (primary stage) and crack propagation (secondary stage).

Low Cycle Fatigue (LCF) failures occur if the amplitude of the cyclic stresses applied to a component is rather high and hence the number of cycles to failure is low. In this case, the accumulated strain energy per reversal and the scale of plastic deformation are significantly high. For this reason, under LCF, a component will spend a very small proportion of its life in the primary, crack initiation stage and the majority of its life in the secondary, crack propagation phase of the fatigue failure. Most of the critical components within jet engines, disks, shafts and pressure vessels like the combustion chamber outer casing are subjected to very high loading cycles and therefore they are life limited by LCF. The mechanical loading on these components is caused by centrifugal forces and thermal loads (on disks), torsion and bending forces (on shafts), high pressure (within the casings) and thermal gradients within the components. The cyclic nature of these forces is due to variations in engine power setting. Hence LCF for a jet engine can be characterised as loading cycles caused by variations in rotational speed, temperature distribution in parts or engine internal pressure due to throttle movement.

High Cycle Fatigue (HCF) occurs if the amplitude of cyclic stresses on a component is lower (relative to that in LCF). The transition point from LCF to HCF is generally assumed to occur when the total strain comprises equal portions of the elastic and plastic strain. However, for convenience, LCF is often considered to lead to failure in less than 10^5 cycles and HCF lead to failure in more than 10^7

cycles. Intermediate range may be considered to fall into either region depending on design application. In case of HCF, crack initiation often tends to be a time-consuming process. HCF is primarily a function of engine design. A component fails in HCF due to a large number of stress cycles that it is subjected to. The layout of the engine itself is the cause of many HCF drivers. For example, the presence of both upstream and downstream obstructions in the gas path can create perturbations in the flow that will cause the turbo-machinery blades to deflect each time they pass. Another strong HCF driver is intake effect. Intake distortion of airflow can create uneven velocity and pressure distributions at the compressor face that induce flutter. One other HCF driver is out-of-balance. An out-of-balance rotor will create small amplitude vibration on components near itself leading to HCF.

Thermo-Mechanical Fatigue (TMF) damage is caused by a combination of the external loads and cyclic compressive or tensile loads induced by thermal gradients across components. Thermal and mechanical load cycles tend to happen simultaneously since thermal loading affects mechanical loading. TMF is particularly significant for turbine blades and vanes, and especially cooled blades and vanes.

Creep is a time-dependent inelastic deformation of metals and alloys, which occurs under stresses at temperatures above about half of the melting point temperature expressed in Kelvin. The higher the temperature and the greater the load, the faster will be the rate of deformation. In a jet engine, the components that suffer most from creep are the hot parts of the turbine disks and turbine blades. A creep process can be divided into three stages, primary, secondary and tertiary, respectively. The primary stage depicts rapid extension at a decreasing rate. The secondary stage shows a relatively constant creep rate. This stage is the important part of the curve for most applications. The tertiary stage shows an acceleration of the creep rate.

Corrosion is an irreversible chemical damage occurring in engine components in aggressive environments. Corrosion may reduce life of engine components in three ways; by reducing a load bearing area, by reducing aerodynamic efficiency and by blockage (of cooling channels).

Erosion is the cumulative damage to components in an airstream caused by small hard particles carried in the gas path. Erosion is most often apparent in compressors; particularly those used in aircraft that routinely operate in dusty or sandy conditions. The typical effects of erosion within jet engine components are removal of material from rotor tips, thus reducing performance, and reducing the chord width of the blades, hence reducing aerodynamic performance.

There are two sources of damage to contacting surfaces; fretting and wear. Fretting is due to relative oscillatory motion of very small amplitudes between two components. This can occur in joints that are bolted, keyed, press fitted, shrunk or riveted. Unlike fretting, wear is the result of large scale, unavoidable relative movement between two components. Typical examples of wear include a piston in the bore of an actuator, bearings, air seals and blade tips on abradable seals.

Individually each mechanism is inconsequential in terms of reduction in mechanical strength and performance loss. However, when many mechanisms take place at one particular area of a component, then the strength and performance loss of that component can be severely compromised. The life of a component is reduced more severely than would be expected by separate considerations of each mechanism.

1.3 ENGINE MONITORING AND LIFING POLICIES

Jet engine components are exposed to widely varying thermo-mechanical loading conditions. Various failure modes progress in a complex manner. Two of the more

important variables that influence these processes are the material that a component is made from, and the way in which the engine is used.

Various failure mechanisms can cause jet engine components to fail catastrophically and without warning. Therefore engine life usage monitoring systems are used to ensure that the components do not fail in service. Engine usage monitoring systems exist for the following reasons:

- to allow aircraft to be operated safely,
- to ensure that as much life as possible is extracted from components to reduce costs,
- to allow performance levels to be pushed to higher levels with lighter and smaller components.

There are two main approaches to the design of life-critical parts in jet engines. In all components, metallurgical defects may become the initiation point for a crack, which may in turn lead to component failure. The first approach aims to retire the components before a crack is detectable. This approach is known as 'Safe Life' or 'Life to First Crack'. The lifing method is based on the probability that no more than 1 in 1000 components will have developed a detectable crack. However, this approach carries a penalty in that many components will be retired prematurely. The second approach tolerates a growing crack and aims to remove component when the crack is detectable. This approach is called the 'Damage Tolerance' approach. However, this approach carries additional costs of a highly structured and organised inspection system.

Whichever lifing policy is used it is necessary to know how engines are used in service in order to calculate how much life has been consumed. This can be done either by monitoring the usage of a representative sample of the fleet or by

monitoring engines individually. The latter requires a higher initial investment but allows a higher proportion of life to be consumed safely. In any case, the following must be known before the service life of components can be assessed.

- the environment and loads to which a component is subjected,
- the macroscopic response of components to applied loads and environmental stresses and strains,
- the microscopic response of the component material to the local stress, temperature and environment conditions.

Magnitudes, variations and exposure times for the temperatures and stresses are the major factors controlling the lives of jet engine components.

Temperature gradients across components are dependent on conductive heat transfer within the component material and convective heat flow at the component surfaces. Engine thermal analysis is usually performed using a finite element or finite difference based software.

Finite element based stress analysis is performed to obtain transient and steady-state stresses in every location of a component taking into account external forces and thermal expansion stress. Principal stresses obtained from calculation results are used to assess the integrity of a component and to identify fracture critical locations.

Combined with a thermal analysis, the outputs of stress calculations may be used to describe stress as a function of time and identify the maximum stress points in the mission and to identify critical and life limiting locations. The expected life is calculated based on stress and temperature history in the critical areas that are identified from the design mission.

1.4 SCOPE OF THE PRESENT WORK

In this thesis, two-dimensional axisymmetric finite element models of a segment of F110-GE-100 engine are generated for thermal and stress analyses by using MARC. Most of the F-16 aircraft in Turkey are powered by this engine. The segment modeled includes the high pressure turbine (HPT) and the nozzle and the nozzle support for the first stage low pressure turbine (LPT). Thermal analysis, which takes both conductive heat transfer within components and convective heat transfer at component surfaces into account, provides temperature distribution throughout the model for a given mission profile. Combined with gas pressure loads, the outputs of thermal analysis are used to perform elastic, temperature dependent static calculations to determine the critical and life-limiting locations. A certain set of components, namely, the pins connecting the first stage LPT nozzle to its support, is known to be critical from practical experience. After confirming this with analysis, two dimensional through the thickness cracks are modeled in MARC to calculate stress intensity factors at different crack lengths. The calculated stress intensity factors and creep crack growth rate data obtained from literature are then used in thermo-mechanical fatigue life calculations, which are performed by using a crack growth life prediction program, AFGROW. Material properties are taken temperature dependent. Gas temperature, pressure and mass flow rate histories in a typical mission are inputs to the study. The ultimate output is the number of hours an engine can be operated in a typical mission before the critical component fails.

1.5 LITERATURE SURVEY

The models of thermo-mechanical fatigue life prediction used for superalloys [1] can be classified into five types: general damage models, damage-rate models, thermo-mechanical fatigue/strain-range partitioning methods (TMF/SRP), modified

J-integral models, and empirical models. These models are briefly explained below, and more detailed explanations are given in Chapter 2.

1.5.1 GENERAL LINEAR ACCUMULATION DAMAGE MODELS

Neu and Sehitoglu [2-5] have developed a general model for high-temperature fatigue, including thermal mechanical fatigue. This model incorporates damage accumulation due to fatigue, environment (oxidation), and creep processes. Damages per cycle from fatigue, environmental attack (oxidation), and creep are summed up to obtain a total damage per cycle.

Chen and colleagues [6] used linear damage summation method in order to predict the fatigue and creep-fatigue behaviour of a nickel-based superalloy at high temperature. The basis of this method is that the creep-fatigue life of the component is assumed to be governed by the independent accumulation of damage due to fatigue and creep.

1.5.2 DAMAGE-RATE MODELS

Miller and colleagues [7] used a physically measurable quantity, such as crack length, as specific definitions of damage. The TMF life prediction model is based on the concept of microcrack propagation and explicitly accounts for damage due to fatigue, creep and oxidation.

1.5.3 TMF/SRP MODELS

Among the principal alternative approaches that treat the creep-fatigue interaction is the SRP approach of Manson, Halford and Hirschberg [8,9]. SRP is based on the observation that the inelastic strain range is the controlling variable on fatigue life.

1.5.4 MODIFIED J-INTEGRAL MODELS

A model by Nissley [10] was developed to predict TMF crack initiation and estimate Mode I crack growth in gas turbine hot-section gas-path superalloys. The model is based on a strain-energy-density fracture mechanics approach modified to account for thermal exposure and single-crystal anisotropy.

1.5.5 EMPIRICAL MODELS

Bernstein and colleagues [11] developed a model to predict the TMF life of industrial gas turbine blades. The model is a semi-empirical approach, similar to most engineering models that are actually used to predict LCF. The formulation does not attempt to separately model the different mechanisms (i.e., fatigue, creep, and environmental attack).

Kanasaki and colleagues [12] have carried out axial-strain-controlled LCF tests of a carbon steel in oxygenated high-temperature water under TMF-IP (in-phase) and TMF-OP (out-of-phase) conditions. Based on the assumption that the fatigue damage increased in a linear proportion to the increment of strain during cycling, a fatigue-life prediction method was proposed.

1.6 OUTLINE OF THE THESIS

The next chapter of the thesis includes fatigue, creep and thermo-mechanical life assessment methodologies. The description of the finite element models generated for thermal analysis, stress analysis is explained in the third chapter. Chapter 4 includes the description of fracture mechanics calculation and life assessment. The last chapter includes the conclusions related with performed studies in the thesis.

CHAPTER 2

THERMO-MECHANICAL FATIGUE LIFE PREDICTION

2.1 INTRODUCTION

Jet engine components are subjected to randomly fluctuating thermo-mechanical loading conditions. It is necessary to know the way an engine is used in order to calculate how much life has been consumed. This can be achieved by monitoring the engine usage to determine the working environment of an engine. The response of a component to applied thermo-mechanical loads, and stress and temperature profiles applied to the component can be obtained from numerical simulation based on engine usage. Since engine components are exposed to thermo-mechanical loads, not only fatigue but also creep affects the life of components. Therefore, a life prediction model that includes these two effects is required for thermomechanical fatigue life prediction. Before discussing thermo-mechanical fatigue (TMF) life prediction techniques, it may be useful to give an overview of fatigue and creep life prediction methods. Sections 2.2 and 2.3 will go over fatigue and creep life prediction, respectively. Section 2.4 will review TMF life prediction and describe various approaches found in the literature.

2.2 FATIGUE LIFE PREDICTION

There are three primary fatigue analysis methods. These are the stress-life approach, the strain-life approach, and the fracture mechanics approach. Fatigue process can be divided into two phases; initiation life and propagation life. The initiation life encompasses the development and early growth of a small crack. The propagation life is the portion of the total life spent growing a crack to failure. However, it is often very difficult to define the transition from initiation to propagation. Generally, initiation is assumed to be the portion of life spent developing a crack size that can be detected by standard nondestructive inspection (NDI). NDI minimum detectable flaw size is around 0.015 inches (0.381 mm).

2.2.1 Stress-Life Approach

The stress-life, S-N, method is the first approach used in an attempt to understand and quantify metal fatigue. The basis of the stress-life method is the Wöhler or S-N diagram, which is a plot of alternating stress, S, versus cycles to failure, N

The S-N approach is used in design applications where the applied stress is primarily within the elastic range of the material and the resultant lives (cycles to failure) are long (HCF). S-N method does not work well in LCF applications where the applied strains have a significant plastic component. In this range a strain-based approach is more appropriate.

The S-N curve in the high-cycle region is sometimes described by the Basquin Equation [13]

$$N \sigma_a^p = C \tag{2.1}$$

where N is the number of cycles to failure, σ_a is the stress amplitude, C and p are empirical constants.

However, Basquin's equation does not take mean stress effects into account. Mean stress effects have been included via the relationships given below.

$$\frac{\sigma_a}{S_e} + \left(\frac{\sigma_m}{S_u}\right)^2 = 1 \quad (\text{proposed by Gerber}) \quad (2.2)$$

$$\frac{\sigma_a}{S_e} + \frac{\sigma_m}{S_y} = 1 \quad (\text{proposed by Soderberg}) \quad (2.3)$$

$$\frac{\sigma_a}{S_e} + \frac{\sigma_m}{S_u} = 1 \quad (\text{proposed by Goodman}) \quad (2.4)$$

$$\frac{\sigma_a}{S_e} + \frac{\sigma_m}{\sigma_f} = 1 \quad (\text{proposed by Morrow}) \quad (2.5)$$

where σ_m is the mean stress, S_e is the endurance limit, S_u is the ultimate strength, S_y is the yield strength, and σ_f is the true fracture stress.

2.2.2 Strain-Life Approach

The strain-life method is based on the observation that in many components the response of the material in critical locations is strain or deformation dependent. When the load levels are low, stresses and strains are linearly related, thus load-controlled and strain-controlled tests are equivalent. At high load levels, in the LCF regime, the applied strains have a significant plastic component and the cyclic stress-strain response and material behaviour are best modeled under strain-controlled conditions.

The elastic component of strain is often described in terms of a relation between the true stress amplitude and the number of reversals by Basquin [13] formula

$$\frac{\Delta\sigma}{2} = \frac{\Delta\varepsilon_e \cdot E}{2} = \sigma'_f (2N_f)^b \quad (2.6)$$

where $\Delta\sigma/2$ is true stress amplitude, $\Delta\varepsilon_e/2$ is true elastic strain amplitude, $2N_f$ is reversals to failure (1 reversal = $\frac{1}{2}$ cycle), σ'_f is fatigue strength coefficient, and b is fatigue strength exponent.

Coffin [14] and Manson [15] working independently described the plastic component of strain by the formula

$$\frac{\Delta\varepsilon_p}{2} = \varepsilon'_f (2N_f)^c \quad (2.7)$$

where $\Delta\varepsilon_p/2$ is plastic strain amplitude, ε'_f is fatigue ductility coefficient, and c is fatigue ductility exponent.

An expression may now be developed that relates total strain range, which is the sum of the elastic and plastic strains range, to life to failure.

$$\frac{\Delta\varepsilon}{2} = \frac{\sigma'_f}{E} (2N_f)^b + \varepsilon'_f (2N_f)^c \quad (2.8)$$

The effect of mean strain is generally negligible on the fatigue life of the component. On the other hand, mean stress may have a significant effect on the fatigue life.

Modifications to the strain-life equation have been made to account for mean stress effects. Morrow [16] suggested that the mean stress effect could be taken into account by modifying the elastic term in the strain-life equation by the mean stress σ_0 . The strain life equation, accounting for mean stress is, then,

$$\frac{\Delta\varepsilon}{2} = \frac{\sigma'_f - \sigma_0}{E} (2N_f)^b + \varepsilon'_f (2N_f)^c \quad (2.9)$$

Equation (2.9) however incorrectly predicts that the ratio of elastic to plastic strain is dependent on mean stress. Manson and Halford [17] modified both the elastic and plastic terms of the strain-life equation to maintain the independence of the elastic-plastic strain ratio from mean stress:

$$\frac{\Delta\varepsilon}{2} = \frac{\sigma'_f - \sigma_0}{E} (2N_f)^b + \varepsilon'_f \left(\frac{\sigma'_f - \sigma_0}{\sigma'_f} \right)^{c/b} (2N_f)^c \quad (2.10)$$

Smith, Watson, and Topper [18] have proposed another equation to account for mean stress effects.

$$\sigma_{\max} \frac{\Delta\varepsilon}{2} = \frac{(\sigma'_f)^2}{E} (2N_f)^{2b} + \sigma'_f \varepsilon'_f (2N_f)^{b+c} \quad (2.11)$$

For the application of this equation, the term σ_{\max} is evaluated as

$$\sigma_{\max} = \frac{\Delta\sigma}{2} + \sigma_0 \quad (2.12)$$

2.2.3 Fracture Mechanics Approach

The fatigue life of a component is made up of crack initiation and propagation stages. This is illustrated schematically in Figure 2.1. The size of the crack at the

transition from initiation to propagation is usually unknown and often depends on the point of view of the analyst and the size of the component being analysed. The distinction between the initiation life and propagation life is important. At low strain amplitudes, up to 90% of the life may be taken up with initiation, while at high amplitudes the majority of the fatigue life may be spent propagating a crack. Generally, initiation is assumed to be the portion of life spent developing a crack size that can be detected by standard nondestructive inspection (NDI). NDI minimum detectable flaw size is around 0.015 inches. Fracture mechanics approaches are used to estimate the propagation life.

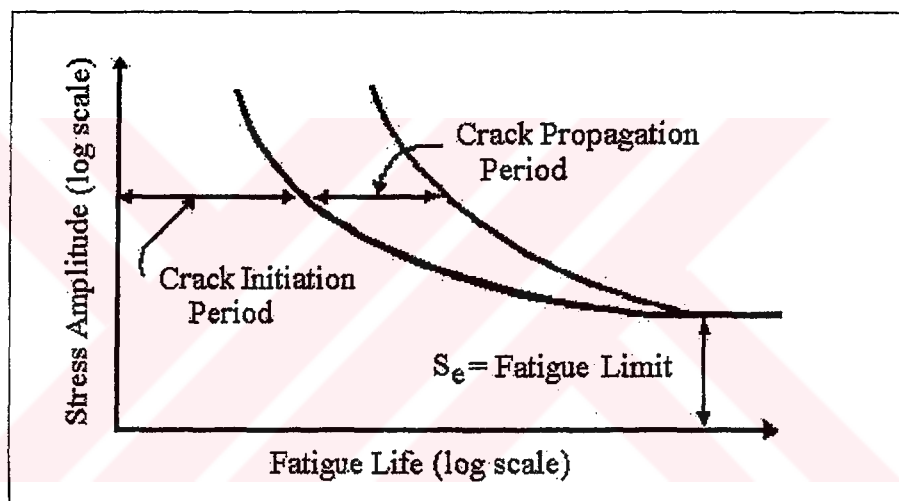


Fig. 2.1 Initiation and Propagation Portions of the Fatigue Life

Fracture mechanics approaches require that an initial crack size be known or assumed. For components with imperfections or defects (such as welding porosities, inclusions and casting defects, etc.) an initial crack size may be known. Alternatively, for an estimate of the total fatigue life of a defect-free material, fracture mechanics can be used to determine propagation. Strain-life approaches

may be used to determine initiation life, with the total life being the sum of these two estimates.

Linear elastic fracture mechanics (LEFM) principles are used to relate the stress magnitude and distribution near the crack tip to:

- Remote stresses applied to the cracked component
- The crack size and shape
- The material properties of the cracked component

LEFM is based on the application of the theory of elasticity to bodies containing cracks or defects. The assumptions used in elasticity are also inherent in LEFM: namely, small displacements and general linearity between stresses and strains. The basis of LEFM remains valid, if this region of plasticity remains small in relation to the overall dimensions of the crack and cracked body. High strength materials used primarily in the engine components have relatively low fracture resistance and they fail below their collapse strength, hence they can be analysed by using LEFM concepts.

2.2.3.1 Loading Modes

There are generally three modes of loading, which involve different crack surface displacements (Figure 2.2). These three modes are: mode I (opening or tensile mode) in which the crack faces are pulled apart, mode II (sliding or in-plane shear mode) in which the crack surfaces slide over each other, and mode III (tearing or anti-plane shear mode) in which the crack surfaces move parallel to the leading edge of the crack and relative to each other.

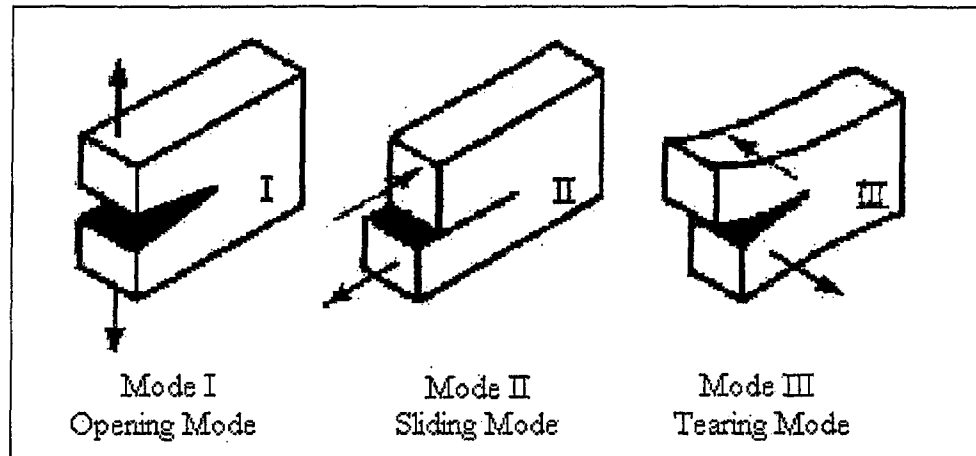


Fig. 2.2 Three Loading Modes

2.2.3.2 Stress Intensity Factor

The stress intensity factor, K , defines the magnitude of the local stresses around the crack tip with the general form given by

$$K = \beta \sigma \sqrt{\pi a} \quad (2.13)$$

where σ is the remote stress applied to a component

a is the crack length

β is the geometry factor

2.2.3.3 Fatigue Crack Growth Curves

LEFM concepts are used to describe crack growth behaviour. The fatigue crack growth rate (FCGR) da/dN is obtained by taking derivative of the crack length, a , versus cycles, N . The plots of the $\log da/dN$ versus $\log \Delta K$ for a given R (load

ratio, $\frac{\sigma_{\max}}{\sigma_{\min}}$) has a sigmoidal shape that divides the curve into three regions.

(Figure 2.3)

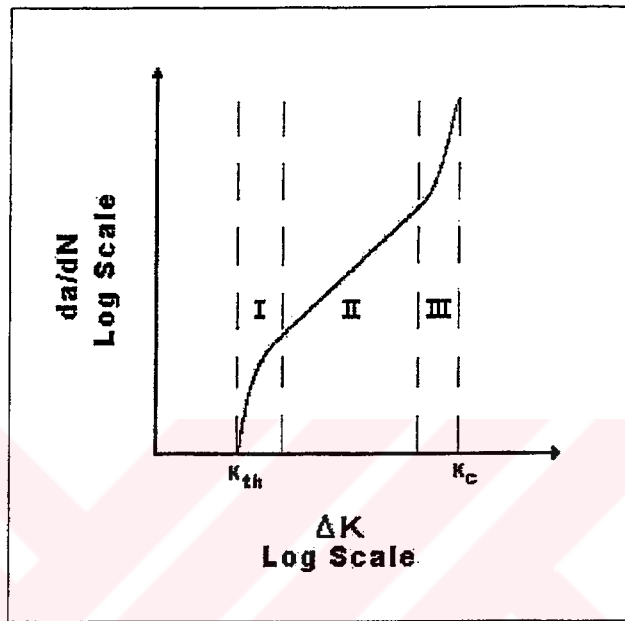


Figure 2.3 Three Regions of Crack Growth Rate Curve

Region I is bounded by a threshold value ΔK_{th} below which there is no observable fatigue crack growth.

Region II is characterised by a linear log-log relationship between da/dN and ΔK . The Paris equation describes the crack growth curves in Region II as:

$$\frac{da}{dN} = C(\Delta K)^m \quad (2.14)$$

where C and m are material constants and

$$\Delta K = \beta \Delta \sigma \sqrt{\pi a} \quad (\text{stress intensity range})$$

Region III is a region of accelerated crack growth. The Forman relation usually gives the influence of stress ratio on the Paris formula as:

$$\frac{da}{dN} = \frac{C(\Delta K)^m}{(1-R) K_c - \Delta K} \quad (2.15)$$

where K_c is the fracture toughness for the material and R is the stress ratio.

In general FCGR da/dN is defined as

$$\frac{da}{dN} = f(\Delta K, R) \quad (2.16)$$

Then, cycles to failure, N_f , may be calculated as

$$N_f = \int_{a_i}^{a_f} \frac{da}{f(\Delta K, R)} \quad (2.17)$$

where a_i is the initial crack length and a_f is the final (critical) crack length.

2.2.3.4 Mixed Mode Fatigue Crack Growth

Traditional applications of fracture mechanics have been concentrated on cracks growing under an opening or mode I mechanism. However, many service failures occur from cracks subjected to mixed mode loadings. A characteristic of mixed mode fatigue cracks is that they usually propagate in a non-self similar manner. In other words, a crack changes its growth direction when subjected to mixed mode loadings. Therefore, under mixed mode loading conditions, not only the FCGR is of importance, but also crack growth direction. Several criteria have been proposed

regarding the crack growth direction under mixed mode loadings. Also, several parameters have been suggested to correlate mixed mode FCGR.

2.2.3.5 Prediction of Mixed Mode Crack Growth Directions

Various criteria for crack growth direction under mixed mode loadings have been proposed. The most widely used two criteria are the maximum tangential stress criterion (MTS criterion) and the minimum strain energy density criterion (S-criterion).

MTS Criterion

This criterion is proposed by Erdogan and Sih [19]. This criterion states that: (i) Crack propagation starts from the crack tip along the radial direction on which the tangential stress becomes maximum; and (ii) Fracture starts when the maximum tangential stress is equal to the fracture stress in uniaxial tension. Mathematically, condition (i) for the crack growth direction can be expressed as

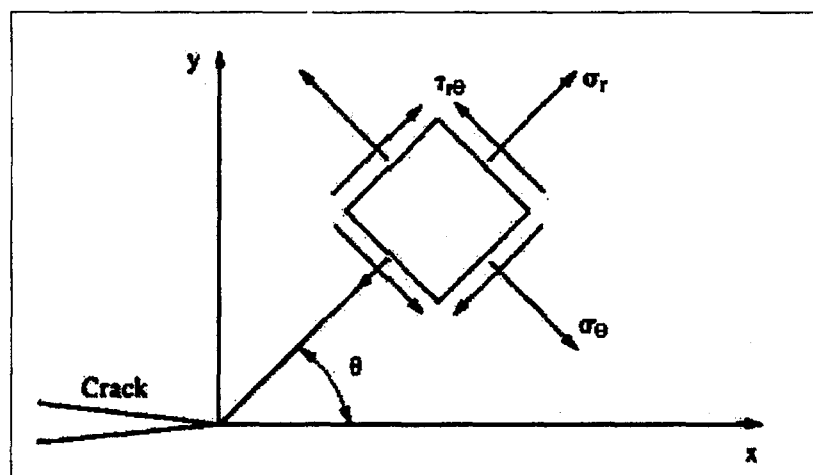


Fig 2.4 Polar Stress Components in a Stress Element Near a Crack Tip

$$\frac{\partial \sigma_{\theta}}{\partial \theta} = 0 \text{ and } \frac{\partial^2 \sigma_{\theta}}{\partial \theta} < 0 \quad (2.18)$$

where σ_{θ} is the maximum tangential stress (Fig 2.4).

If Westergaard expressions are used to describe the stress field near the crack tip for a mixed mode I and II loading case, it can be shown that the above criterion for the crack growth direction is the solution of the following equation:

$$K_I \sin \theta + K_{II} (3 \cos \theta - 1) = 0 \quad (2.19)$$

S - Criterion

This criterion was proposed by Sih [20], and is based on the local density of the energy field in the crack tip region. The crack is assumed to grow in a direction along which the strain energy density factor S reaches a minimum value and fracture occurs when this factor reaches a critical value. The strain energy density factor S can be written as:

$$S = a_{11} k_1^2 + 2 a_{21} k_1 k_2 + a_{22} k_2^2 + a_{33} k_3^2 \quad (2.20)$$

where a_{ij} : the coefficients relating polar angle (θ), elastic modulus (E) and Poisson's ratio (ν), and $k_i = K_i / \sqrt{\pi}$ ($i = I, II, III$).

2.2.3.6 Prediction of Mixed Mode FCGR

A number of parameters have been suggested to correlate FCGR under mixed mode loading conditions. Most commonly used parameters are given below.

Effective Stress Intensity Factors

The FCGR can be expressed by using Paris equation as a function of an effective stress intensity factor:

$$\frac{da}{dN} = C (\Delta K_{\text{eff}})^m \quad (2.21)$$

where $K_{\text{eff}} = \sqrt{K_I^2 + K_{II}^2}$ for mixed mode I and II loadings.

This criterion states that fracture condition is

$$K_I^2 + K_{II}^2 = K_{IC}^2 \quad (2.22)$$

where K_{IC} is the fracture toughness under mode I loading.

J-Contour Integral

This criterion was proposed by Hellen and Blackburn [21] in order to use path independent line integrals to study the problem of crack growth under mixed mode loadings. In a two-dimensional problem, a vector, \mathbf{J} , is defined as:

$$\mathbf{J} = J_I \bar{\mathbf{i}} + J_{II} \bar{\mathbf{j}} \quad (2.23)$$

with

$$J_k = \int_{\Gamma} (w n_k - u_{i,k} T_i) ds \quad k = I, II \quad (2.24)$$

where Γ is the contour integration, w is the strain energy density, n_k is the k component of the unit outward normal to the contour of integration, u_i is the displacement, T_i is the traction, and ds is the arc length element for the integration

contour. This criterion states that: (i) the crack extends along the direction of vector \mathbf{J} , and (ii) fracture occurs when this vector \mathbf{J} reaches a critical value.

2.2.4 Variable Amplitude Loading

Up to this point, most of the discussion about fatigue behaviour has dealt with constant amplitude loading. In contrast, most service loading histories have variable amplitude and can be quite complex. It is necessary to reduce the complex history into a number of blocks of constant amplitude cycles.

2.2.4.1 Cycle Counting

For a highly irregular nominal stress history, such as Fig. 2.5, care must be taken in defining cycles. In particular, it is very important that small stress excursions, such as 2-3-2', be considered as temporary interruptions of larger stress excursions, such as 1-4. Otherwise, the significance of larger stress excursions is lost, and major errors in life prediction can result [22]. Therefore, a method is needed to detect (or count) cycles. The range pair [23] and rain-flow [24] cycle counting methods, and also some related methods derived from these [25, 26] are quite similar to each other, and all share in handling small excursions in the desired manner.

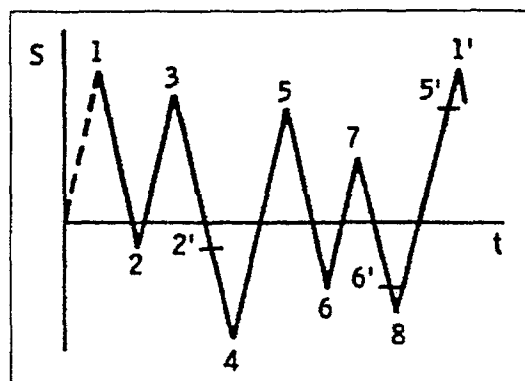


Figure 2.6 illustrates the rain-flow cycle counting method using the history of Fig. 2.5. This method is analogous to water flow in rainy weather on the roof of a pagoda. The loading history is plotted with the time axis vertical, and water flowing down the resulting pagoda-roof-like structure is subjected to a set of rules. Water is injected at each point of stress reversal in order and flows by gravity subjected to the following:

- a) For water moving toward the left and down, the flow disappears if it comes opposite a reversal point farther to the right than, or equal to, the one from which it started.
- b) For water moving toward the right and down, the flow disappears if it comes opposite a reversal point farther to the left than, or equal to, the one from which it started.
- c) The flow disappears to avoid meeting water from a roof above.

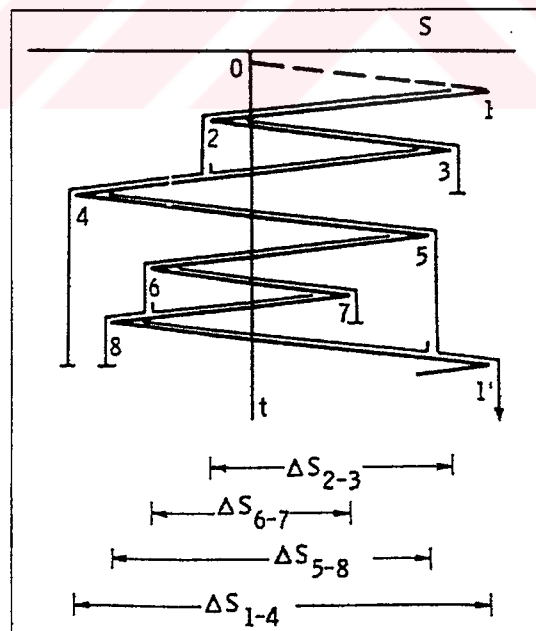


Fig. 2.6 Rain-flow Cycle Counting Applied to History of Fig. 2.5

For example, in Fig. 2.6, the water from 1 disappears opposite 1' due to rule (a), reversal point 1' being equal to 1. The water from 2 disappears opposite 4 due to rule (b), reversal point 4 being farther to the left than 2. And the water from 3 disappears under 2 due to rule (c), to avoid meeting the water flowing down from 2. Once the rain-flow rules are followed for the entire history, the horizontal length of each continuous rain-flow is taken to be the range of a half cycle. In most cases, the majority of these half cycles will occur in pairs that may be combined to form cycles. In Fig. 2.6, all half cycles can be paired, so that four full cycles are counted, these corresponding in Fig. 2.5 to stress excursions 2-3-2', 6-7-6', 5-8-5' and 1-4-1'. An important point to note is the placement of the maximum value in the spectrum. Some fracture mechanics experts prefer to place the overall maximum value at the end of the spectrum to minimize the effect on crack growth retardation (more conservative result). Others may prefer to place the maximum peak in the order that the peak occurs in the original sequence.

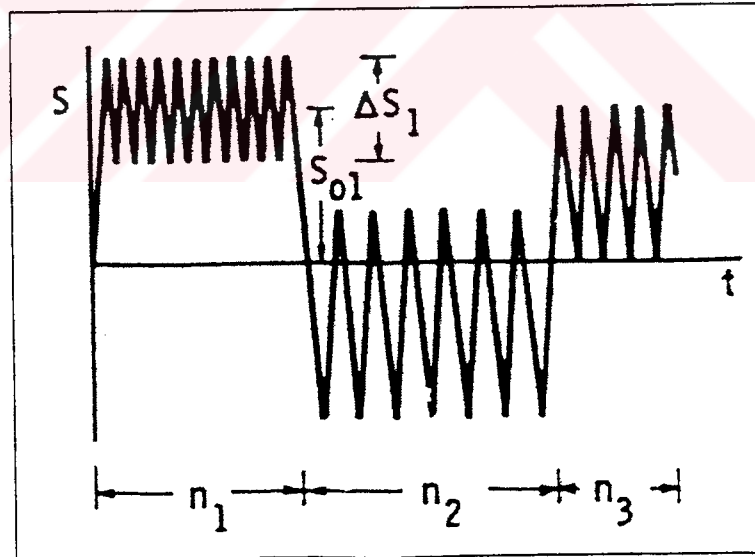


Fig. 2.7 Fatigue Loading History of Blocks of Constant Amplitude Cycles

2.2.4.2 Damage Summing Method for Stress-Life Approach

After rain-flow cycle counting procedure, blocks of well-defined constant amplitude cycles similar to Fig. 2.7 are obtained. The fatigue life is primarily affected by the stress ranges applied, such as ΔS_1 , and only secondarily affected by the mean stresses, such as S_{01} , in case of HCF conditions. A life prediction may be made by using an appropriate S-N curve, such as Figure 2.8. The Palmgren-Miner rule [27, 28] may be applied to life prediction for a repeating history by summing cycle ratios during only one repetition of the history.

$$\left[\sum_{\text{one rep.}} \left(\frac{n_i}{N_i} \right) \right] R = 1 \quad (2.25)$$

where n_i is the number of cycles applied at stress range ΔS_i , N_i is the number of cycles to failure corresponding to ΔS_i , and R is the number of repetitions of blocks of constant amplitude cycles.

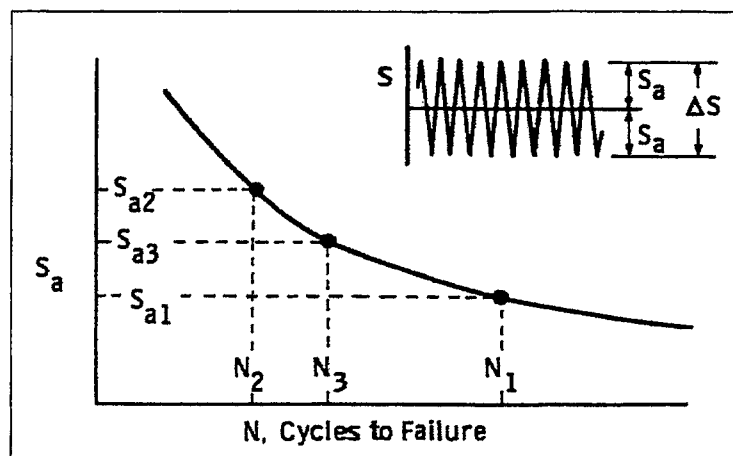


Fig. 2.8 Use of a Constant Amplitude S-N Curve with the Palmgren-Miner Rule

2.2.4.3 Damage Summing Method for Strain-Life Approach

Miner's rule may also be used in conjunction with the strain-life approach. The only difference is that the life to failure, N , in the cycle ratio n/N , is taken from the strain-life curve. Moreover, mean stresses have a significant effect on the fatigue life in case of LCF conditions. Therefore, modified strain-life equations have to be used.

2.2.4.4 Crack Propagation Under Variable Amplitude Loading

Under constant amplitude loading conditions, the increment of crack growth, Δa , is dependent only on the present crack size and the applied load, under variable amplitude loading Δa is also dependent on the preceding cyclic history. This phenomenon is known as load interaction.

Load interaction or sequence effects significantly affect the FCGR and consequently, fatigue lives. The application of single overload was observed to cause a decrease in the FCGR, as shown in Fig. 2.9. This phenomenon is termed crack retardation. Crack retardation is usually attributed to a combination of compressive residual stresses and crack closure due to residual stresses.

A number of models have been proposed [29-33] to treat retardation. These models have been discussed in literature [34,35]. Most of these models are semi-empirical and contain one or more constants to be determined from experiments.

The most commonly used crack retardation models are crack tip plasticity models proposed by Wheeler [29], by Willenborg [30] and Elber[31]. The models assume that retardation occur due to the large plastic zone developed during the overload.

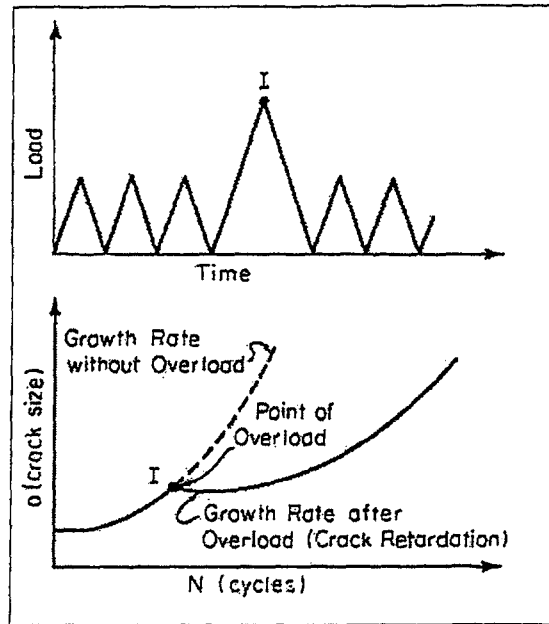


Figure 2.9 Crack Growth Retardation After an Overload

Wheeler Model:

Wheeler introduces a crack-growth reduction factor, C_p .

$$\frac{da}{dN} = C_p f(\Delta K, R) \tag{2.26}$$

where $f(\Delta K, R)$ is the usual crack-growth function. The retardation factor C_p is given as (See Figure 2.10):

$$C_p = \left[\frac{r_{pi}}{a_o + r_{po} - a_i} \right]^m = \left[\frac{r_{pi}}{s - a_i} \right]^m \tag{2.27}$$

where r_{pi} is current plastic zone in the i^{th} cycle under consideration, a_i is current crack size, r_{po} is size of the plastic zone generated by a previous overload, a_o is crack size at which overload occurred, and m is retardation exponent

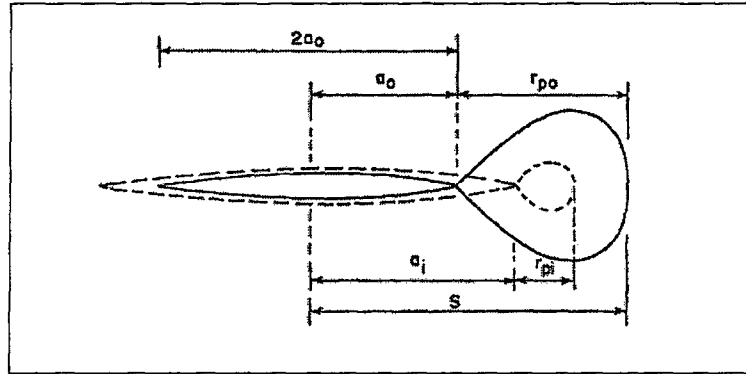


Figure 2.10 Plastic Zone Parameters Used in Wheeler and Willenborg Models

At any given crack size, a_i , only that previous overload is of importance for which $s = a_o + r_{po}$ is largest. The size of the plastic zone is

$$r_{pi} = \frac{K_{\max,i}^2}{\alpha \sigma_{ys}^2} = \frac{(\Delta K)_i^2}{(1-R)^2 \alpha \sigma_{ys}^2} ; r_{po} = \frac{K_{\max,o}^2}{\alpha \sigma_{ys}^2} \quad (2.28)$$

where $\alpha = 2\pi$ for plane stress and $\alpha = 6\pi$ for plane strain.

There is retardation as long as the current plastic zone size is contained within a previously generated plastic zone. If $r_{pi} > (s - a_i)$ then $C_p = 1$. The retarded FCGR can be determined from the constant amplitude FCGR as

$$(da/dN)_{\text{retarded}} = C_p (da/dN)_{\text{linear}} \quad (2.29)$$

Willenborg Model:

The Willenborg model makes use of an effective stress intensity factor based on the size of the yield zone in front of the crack tip. The maximum stress intensity in the i^{th} cycle, $\{K_{\max,i} = \Delta K_i / (1 - R)\}$ is reduced to $K_{\max, \text{eff}}$ as:

$$\left. \begin{aligned} K_{\max, \text{eff}} &= K_{\max} - K_{\text{red}} \\ K_{\min, \text{eff}} &= K_{\min} - K_{\text{red}} \\ K_{\text{red}} &= K_{\max, o} \sqrt{1 - \frac{a_i - a_o}{r_{po}}} - K_{\max} \\ \phi &= \left(1 - \frac{\Delta K_{\text{thres}}}{K_{\max}}\right) (\text{SOLR} - 1) \end{aligned} \right\} \quad (2.30)$$

where SOLR (Shut-off Ratio) is defined as the of overload maximum stress to the subsequent maximum stress required to arrest crack growth.

Since K_{\max} and K_{\min} are reduced by the same amount, the overload does not change ΔK but causes a reduction of the cycle ratio R , as long as $K_{\min, \text{eff}} > 0$.

When $K_{\min, \text{eff}} < 0$, it is then set to zero. In that case $R = 0$ and $\Delta K = K_{\max, \text{eff}}$.

In essence, these retardation models require a cycle-by-cycle integration of crack growth. During the i^{th} cycle at crack size a_i , a stress range $\Delta\sigma_i$ is applied. The stress intensity range is $\Delta K_i = \beta \Delta\sigma_i \sqrt{\pi a_i}$. The linear FCGR follows from constant amplitude data as $(da/dN)_{\text{linear}}$. Application of one of the retardation models gives retarded FCGR $(da/dN)_{\text{retarded}}$. This means that the crack extends to

$$a_{i+1} = a_i + \Delta a = a_i + 1 \times (da/dN)_{\text{retarded}} \quad (2.31)$$

Then, $\Delta K_{i+1} = \beta \Delta \sigma_{i+1} \sqrt{\pi a_{i+1}}$ so that the process can be repeated for the next cycle.

Elber's Closure Model:

The closure model proposed by Elber is a fairly simple single-parameter plasticity model. This model is called a closure model because it is based on the idea that the crack is closed when no load is applied and a certain load must be applied to open the crack tip. There is a significant compressive residual stress in front of the crack tip. This compressive residual stress must be overcome by applied tensile loading before the crack can extend. There is some minimal applied tensile load that must be reached before the crack may extend. This value is referred to as the opening load. There is a relationship between the maximum applied stress and this opening stress. The closure factor, C_f , was defined as the ratio of the opening stress to the maximum applied stress and is a function of stress ratio (R).

$$C_f = \frac{\sigma_{open}}{\sigma_{max}} = 1 - (1 - C_{f0})(1 + 0.6 \cdot R)(1 - R) \quad (2.32)$$

where C_{f0} is the crack opening load ratio (OLR) for $R = 0$.

Then, an effective K is determined from

$$K_{eff} = K_{max} - K_{open} \quad (2.33)$$

Since the input crack growth rate data is not based on K_{eff} , a conversion back to apparent SIF is necessary. This conversion, however, is based on the C_f value for the current load cycle.

$$\Delta K_{\text{apparent}} = \Delta K_{\text{eff}} \frac{1-R}{1-C_f} \quad (\text{for } R \geq 0) \quad (2.34)$$

$$\Delta K_{\text{apparent}} = \frac{\Delta K_{\text{eff}}}{1-C_f} \quad (\text{for } R \leq 0)$$

In this way, the result of predictions made using constant amplitude spectra will give the same results as the no retardation case.

2.3 CREEP LIFE PREDICTION

Materials are often placed in service at elevated temperatures and exposed to static mechanical stresses. Time-dependent inelastic deformation of materials under such circumstances is termed creep. Creep is an undesirable phenomenon and is often the limiting factor in the lifetime of a part. It is observed in all material types and becomes important for temperatures greater than about $0.5 T_m$ where T_m is the melting temperature of material in Kelvin.

A typical creep test consists of subjecting a specimen to a constant load or stress while maintaining the temperature constant; deformation or strain is measured and plotted as a function of elapsed time (Figure 2.11).

The figure below is a schematic representation of the typical constant load creep behaviour of metals. Upon application of the load there is an instantaneous deformation, which is mostly elastic. The resulting creep curve consists of three regions, each of which has its own distinctive strain-time feature. Primary or transient creep occurs first, typified by a continuously decreasing creep rate; that is, the slope of the curve diminishes with time. This suggests that the material is experiencing an increase in creep resistance, deformation becomes more difficult as

the material is strained (which is known as strain hardening). For secondary creep, sometimes termed steady-state creep, the rate is nearly constant; that is the plot becomes linear. This is often the stage of the creep having the longest duration. The constancy of creep rate is explained on the basis of a balance between the competing processes of strain hardening and recovery, recovery being the process whereby a material becomes softer and retains its ability to experience deformation. Finally, for tertiary creep, there is an acceleration of the rate and ultimate failure occurs. The time to failure t_r is called rupture time. This failure is frequently termed rupture and results from microstructural and/or metallurgical changes; for example, grain boundary separation, and the formation of internal cracks, cavities, and voids. Also, for tensile loads, a neck may form at some point within the deformation region. These all lead to a decrease in the effective cross-sectional area and an increase in strain rate.

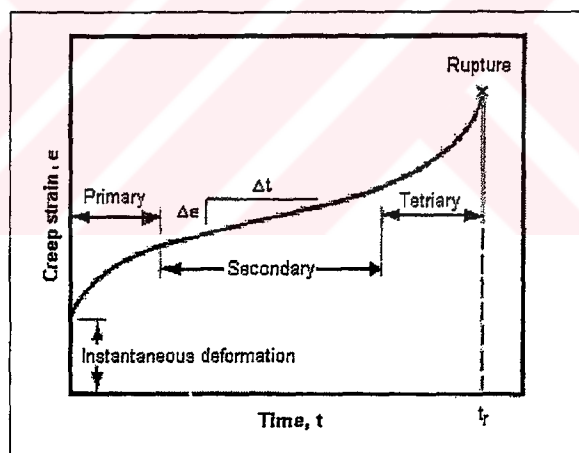


Figure 2.11 A Typical Creep Strain versus Time Curve at a Constant Stress at Elevated Temperature

Both temperature and the level of the applied stress influence the creep characteristics. With either increasing stress or temperature, the following will be

noted: (1) the instantaneous strain at the time of stress application increases, (2) the steady-state creep rate increases, and (3) the rupture lifetime diminishes.

The most commonly used parameters in creep life predictions are the steady-state creep rate $\dot{\epsilon}_s$, and the steady-state creep crack growth rate \dot{a} .

Steady-State Creep Rate ($\dot{\epsilon}_s$)

It is the slope of the secondary portion of the creep rate ($\Delta\epsilon/\Delta t$ in Figure 2.11). $\dot{\epsilon}_s$ is expressed as a function of stress and temperature as [36]:

$$\dot{\epsilon}_s = K\sigma^n \exp\left(-\frac{Q_c}{RT}\right) \quad (2.35)$$

where K and n are constants; Q_c is termed the activation energy for creep.

The following observation is frequently made in creep studies that

$$\dot{\epsilon}_s t_r = \text{constant} \quad (2.36)$$

Therefore, once $\dot{\epsilon}_s$ is calculated using equation (2.32), t_r is immediately obtained.

Creep rupture tests are generally conducted under uniaxial stress conditions. The mathematical formulations given above should therefore be modified to include multiaxial effects.

Kraus [36] modified creep rupture equations by using von Mises stress in place of uniaxial stress in equation (2.35).

Hayhurst and Leckie [37] proposed a multiaxial stress parameter as:

$$\sigma_{rup} = \alpha \sigma_1 + \beta \sigma_H + \gamma \sigma_e \quad (2.37)$$

where σ_1 is the maximum principal stress, σ_H is the hydrostatic stress, and σ_e is the von Mises stress (or effective stress).

Hayhurst and Leckie [37] have reviewed multiaxial creep rupture data for several cases and have found that the maximum principal stress, σ_1 , and the von Mises stress, σ_e are much more important than σ_H in determining creep rupture. Hence they modified equation (2.34) as:

$$\sigma_{rup} = \alpha \sigma_1 + (1 - \alpha) \sigma_e \quad (2.38)$$

Nix et al. [38] proposed another stress parameter, the principal facet stress which is defined as:

$$\sigma_F = 2.24 \sigma_1 - 0.62 (\sigma_2 + \sigma_3) \quad (2.39)$$

where $\sigma_1 > \sigma_2 > \sigma_3$ are the principal stresses.

Thus, the term σ in equation (2.32) should be replaced with one of the proposed multiaxial stress parameter to predict t_r under multiaxial loading conditions.

Steady-State Creep Crack Growth Rate (\dot{a})

Steady-State CCGR, \dot{a} is also widely used in creep life calculations. It may be expressed as a function of stress intensity factor and temperature as:

$$\dot{a} = A K^n \exp\left(-\frac{Q_c}{RT}\right) \quad (2.40)$$

where A and n are constants.

There is a parallelism between the crack growth behaviour and creep behaviour, hence it is observed in creep tests that the following equation is satisfied.

$$\dot{a} t_r = \text{constant} \quad (2.41)$$

Multiaxial effects in that case may be included by using an effective stress intensity factor in equation (2.41).

2.4 THERMO-MECHANICAL FATIGUE LIFE PREDICTION

Fatigue and creep life prediction models are described above. In order to completely assess the life of engine components subjected to thermo-mechanical loading conditions, thermo-mechanical fatigue life prediction models are proposed. These models include the effects of fatigue and creep, and also the creep-fatigue interaction. The effect of the environment is also included in those models, the most critical environmental effect being oxidation.

2.4.1 General Linear Accumulation Damage Models

Neu and Sehitoglu [2-5] have developed a general model for high-temperature fatigue, including thermal mechanical fatigue. This model incorporates damage accumulation due to fatigue, environment (oxidation), and creep processes.

Damages per cycle from fatigue, environmental attack (oxidation), and creep are summed up to obtain a total damage per cycle.

$$D^{\text{tot}} = D^{\text{fat}} + D^{\text{ox}} + D^{\text{creep}} \quad (2.42)$$

Assuming that total damage is equal to one at failure, the equation may be rewritten in terms of the initiation life, N_f , where the damage is taken as equal to $1/N_f$,

$$\frac{1}{N_f} = \frac{1}{N_f^{\text{fat}}} + \frac{1}{N_f^{\text{ox}}} + \frac{1}{N_f^{\text{creep}}} \quad (2.43)$$

Then, total life is expressed as a sum of initiation life N_f and propagation life N_f^{P}

$$N_f^{\text{tot}} = N_f + N_f^{\text{P}} \quad (2.44)$$

Fatigue Damage Term

Fatigue life term is calculated by using strain-life equation

$$\frac{\Delta \epsilon_m}{2} = C (2N_f^{\text{fat}})^d \quad (2.45)$$

where $\Delta \epsilon_m$ is the mechanical strain-range, and C and d are material constants determined from low-temperature isothermal tests.

Environmental-Damage (Oxidation) Term

The oxidation damage term is based on the crack nucleation and growth through an oxide layer. It can be expressed by:

$$\frac{1}{N_f^{ox}} = \left[\frac{h_{cr} \delta_0}{B \Phi^{ox} K_P^{eff}} \right]^{-\frac{1}{\beta}} \frac{2(\Delta \epsilon_m)^{(2/\beta)+1}}{\dot{\epsilon}^{1-(\alpha/\beta)}} \quad (2.46)$$

where h_{cr} is a critical crack length at which the environmental attack trails behind the crack tip advance, δ_0 is the ductility of the environmentally affected material, B is a coefficient, β is an exponent, and α is the strain-rate sensitivity constant. The values of all above are determined by experiments. Φ^{ox} is a phasing factor for environmental damage and is defined as:

$$\Phi^{ox} = \frac{1}{t_c} \int_0^t \phi^{ox} dt \quad (2.47)$$

$$\phi^{ox} = \exp \left[-\frac{1}{2} \left(\frac{(\dot{\epsilon}_{th} / \dot{\epsilon}_m) + 1}{\xi^{ox}} \right)^2 \right] \quad (2.48)$$

where $\dot{\epsilon}_{th} / \dot{\epsilon}_m$ is the ratio of thermal to mechanical strain rates, and ξ^{ox} is a constant as a measure of the relative amount of oxidation damage for different thermal strain to mechanical ratios and is extracted from the experiments. K_P^{eff} is a parabolic oxidation constant and can be calculated by

$$K_P^{eff} = \frac{1}{t_c} \int_0^t D_0 \exp \left(\frac{-Q}{RT(t)} \right) dt \quad (2.49)$$

where $T(t)$ is the temperature as a function of time, t_c is the cycle period, D_0 is the diffusion coefficient for oxidation, Q is the activation energy for oxidation, and R is the gas constant.

Creep-Damage Term

The creep-damage term is a function of temperature, effective stress, and hydrostatic stress components, and can be expressed by:

$$D^{\text{creep}} = \Phi^{\text{creep}} \int_0^t A e^{(-\Delta H / RT(t))} \left(\frac{\alpha_1 \bar{\sigma} + \alpha_2 \sigma_H}{K} \right)^m dt \quad (2.50)$$

where $\bar{\sigma}$ is the effective stress, σ_H is the hydrostatic stress, K is the drag stress, α_1 and α_2 are scaling factors that represent the relative amount of damage occurring in tension and compression, ΔH is the activation energy for the rate-controlled creep mechanism, and A and m are material constants.

$$\Phi^{\text{creep}} = \frac{1}{t_c} \int_0^t \phi^{\text{creep}} dt \quad (2.51)$$

$$\phi^{\text{creep}} = \exp \left[-\frac{1}{2} \left(\frac{(\dot{\epsilon}_{th} / \dot{\epsilon}_m) + 1}{\xi^{\text{creep}}} \right)^2 \right] \quad (2.52)$$

where the constant ξ^{creep} defines the sensitivity of the phasing to the creep damage.

Propagation Life

The propagation life is calculated by Paris Law

$$N_f^P = C (\Delta K)^m \quad (2.53)$$

where C and m are material constants.

Chen and colleagues [6] used linear damage summation method in order to predict the fatigue and creep-fatigue behaviour of a nickel-based superalloy at high temperature. The basis of this method is that the creep-fatigue life of the component is assumed to be governed by the independent accumulation of damage due to fatigue and creep. The fatigue damage (D_f) and the creep damage (D_c) is defined as follows:

$$D_f = \frac{N}{N_f} \quad (2.54)$$

$$D_c = \frac{N \cdot t_h}{t_r} \quad (2.55)$$

where N_f is the number of cycles to failure in pure fatigue conditions, N is the number of cycles to failure in fatigue-creep tests, t_h is the hold time and t_r is the rupture time for pure creep conditions.

Linear damage summation method assumes that the failure occurs when $D_f + D_c = 1$. In this way the method can be described by the following equation:

$$N = \frac{1}{\left[\frac{1}{N_f} + \frac{t_h}{t_r} \right]} \quad (2.56)$$

2.4.2 Damage-Rate Models

Miller and colleagues [7] used a physically measurable quantity, such as crack length, as specific definition of damage. The thermo-mechanical fatigue life (TMF) life prediction model is based on the concept of microcrack propagation and explicitly accounts for damage due to fatigue, creep and oxidation.

The general form of the equation is:

$$\frac{da}{dN} = \left(\frac{da}{dN}\right)_{\text{fat}} + \left(\frac{da}{dN}\right)_{\text{ox}} + \left(\frac{da}{dN}\right)_{\text{creep}} \quad (2.57)$$

where a is the crack length, and N is the cycle number.

The fatigue component of microcrack propagation is correlated using the ΔJ parameter

$$\left(\frac{da}{dN}\right)_{\text{fat}} = C_f \Delta J^{m_f} \quad (2.58)$$

where C_f and m_f are constants, and ΔJ is defined as:

$$\Delta J = 2\pi Y^2 \left[\frac{\Delta\sigma \Delta\varepsilon_e}{2} + \frac{f(1/n') \Delta\sigma \Delta\varepsilon_p}{2\pi} \right] \cdot a \quad (2.59)$$

where $\Delta\sigma$ is the stress range and $\Delta\varepsilon_e$ and $\Delta\varepsilon_p$ are the elastic and plastic strain ranges, respectively, n' is the cyclic-hardening exponent, Y is a geometric correction factor, and a is the crack length. The function $f(1/n')$ is given by:

$$f(1/n') = 3.85 \sqrt{\frac{1}{n'}} (1 - n') + \pi n' \quad (2.60)$$

If equation (3.17) is integrated between appropriate initial and final crack sizes, the integrated form of fatigue components is obtained

$$\frac{Z_f}{C'_f} = \alpha^{m_f} N_f \quad (2.61)$$

where

$$Z_f = \frac{a_f^{(1-m_f)} - a_0^{(1-m_f)}}{1-m_f} \quad \text{if } m_f \neq 1$$

$$Z_f = \ln(a_f) - \ln(a_0) \quad \text{if } m_f = 1$$
(2.62)

$C'_f = 2\pi Y^2 C_f$, a_0 and a_f are the initial and final crack sizes, respectively, and α is defined as:

$$\alpha = \frac{\Delta\sigma \Delta\varepsilon_e}{2} + \frac{f(1/n') \Delta\sigma \Delta\varepsilon_p}{2\pi}$$
(2.63)

The creep component of the microcrack propagation is correlated using the stress power release rate parameter, \hat{C} :

$$\left(\frac{da}{dN} \right)_{\text{creep}} = C_c \hat{C}^{m_c}$$
(2.64)

where C_c and m_c are the experimentally determined creep constant and exponent, respectively.

$$\hat{C} = \left\langle a \left[\frac{1}{t_t} \int_0^{t_t} \sigma \dot{\varepsilon}_c dt - \frac{1}{t_c} \int_0^{t_c} \sigma \dot{\varepsilon}_c dt \right] \right\rangle$$
(2.65)

where $\dot{\varepsilon}_c$ is the creep-strain rate, t_t is the time within a cycle during which tensile strain accumulates, and t_c is the time within a cycle during which compressive strain accumulates. The Macaulay brackets, $\langle \rangle$ are defined as

$$\langle f \rangle = \begin{cases} f, & \text{if } t \geq 0 \\ 0, & \text{if } t < 0 \end{cases}$$
(2.66)

The creep strain rate, $\dot{\epsilon}_c$ is determined using a viscoplastic constitutive law for the material under investigation.

The oxidation component of the microcrack propagation is also correlated using the ΔJ parameter with an additional time and temperature dependence

$$\left(\frac{da}{dN}\right)_{ox} = C_0 \Delta J^{m_0} \cdot \Delta t^\psi \quad (2.67)$$

where m_0 and ψ are experimentally determined constants, Δt is the cycle time, and the coefficient C_0 is defined as:

$$C_0 = C'_0 \exp\left[\frac{-(Q_{ox} - B\hat{\sigma}^k)}{RT_{eff}}\right] \quad (2.68)$$

where C'_0 , B , and k are experimentally determined constants, Q_{ox} is the experimentally measured activation energy of the effective crack tip oxidation and growth process; The parameter $\hat{\sigma} = \langle \sigma_{T_{min}} \rangle$; and $\sigma_{T_{min}}$ is the stress at the minimum temperature. T_{eff} is the effective temperature and is defined as :

$$\exp\left[\frac{-Q_{ox}}{RT_{eff}}\right] = \frac{1}{\Delta t} \int_{t_{min}}^{t_{max}} \exp\left[\frac{-Q_{ox}}{RT(t)}\right] dt \quad (2.69)$$

where t_{min} and t_{max} are the times at which the minimum and maximum temperatures occur during a temperature cycle, respectively, and $\Delta t = t_{max} - t_{min}$.

2.4.3 TMF/SRP Models

Among the principal alternative approaches that treat creep-fatigue interaction is the SRP approach of Manson, Halford and Hirschberg [8,9]. SRP is based on the observation that the inelastic strain range is the controlling variable on fatigue life. Specifically, SRP recognises four modes of cyclic inelastic straining. These modes are the following (Figure 2.12):

- pp : The inelastic strain range is considered to be composed of plastic strain in both tension and compression
- cp : creep strain in tension and plastic strain in compression
- pc : plastic strain in tension and creep strain compression
- cc : creep strain in both tension and compression

For each of the inelastic deformation types, a life relation is established as:

$$\Delta \epsilon_{ij} = A_{ij} (N_{ij})^{a_{ij}} \quad (2.70)$$

where $ij = p, c$ (i.e., pp, cp, pc and cc modes), and A_{ij} and a_{ij} are material-dependent parameters.

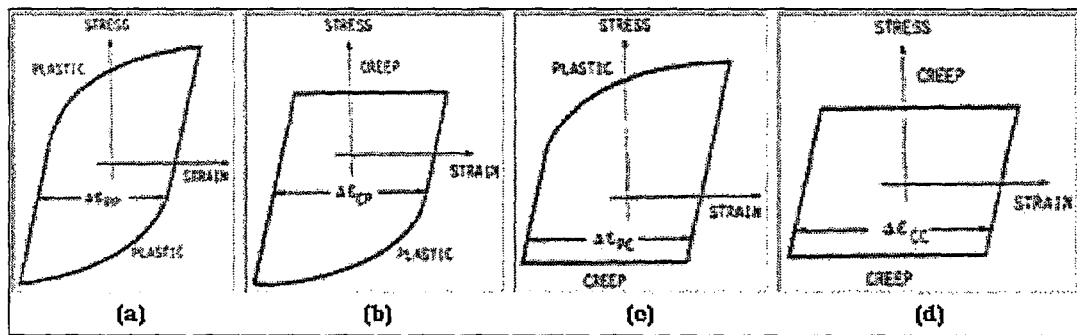


Figure 2.12 SRP Cycle Types Showing
(a) pp type, (b) cp type, (c) pc type, and (d) cc type

Life prediction is achieved by the use of interaction damage rule stated as:

$$\frac{1}{N_f} = \frac{F_{pp}}{N_{pp}} + \frac{F_{cp}}{N_{cp}} + \frac{F_{pc}}{N_{pc}} + \frac{F_{cc}}{N_{cc}} \quad (2.71)$$

where F_{pp} , F_{cp} , F_{pc} and F_{cc} correspond to the relative amount of inelastic-strain type present and the terms N_{pp} , N_{cp} , N_{pc} and N_{cc} correspond to the life levels obtained from equation (2.70).

2.4.4 Modified J-Integral Models

A model by Nissley [10] was developed to predict TMF crack initiation and estimate Mode I crack growth in gas turbine hot-section gas-path superalloys. The model is based on a strain-energy-density fracture mechanics approach modified to account for thermal exposure and single-crystal anisotropy.

An effective J-integral was developed for TMF crack-life prediction. The developed effective J-integral fracture mechanics TMF model is formulated as:

$$\frac{da}{dN} = A J_{\text{eff}} v^c \quad (2.72)$$

with

$$\frac{1}{v} = \int_{\text{cycle}} \exp \left[Q_0 \left(\frac{1}{T_0} - \frac{1}{T} \right) \right] dt \quad (2.73)$$

where A , c , Q_0 and T_0 are material constants, T is the absolute temperature, and J_{eff} is the effective J-integral defined as

$$J_{\text{eff}} = \pi(a + a_0)(J^2 f W_{\text{eff}}^{\text{tot}})^b - J_{\text{th}} \quad (2.74)$$

where a_0 is the initial material defect size (material constant), b is a material constant, β is the crack boundary correction factor, J_{th} is the threshold J-integral that may be constant or temperature dependent, f is a crystallographic strain energy correction factor, and $W_{\text{eff}}^{\text{tot}}$ is the effective total strain energy density defined as:

$$W_{\text{eff}}^{\text{tot}} = 2W_e + \gamma W_p \quad (2.75)$$

$$W_e = (\sigma_{\text{max}} - m \sigma_{\text{min}})^2 / 2E_{\text{max}} \quad (2.76)$$

$$W_p = \int_{\text{cycle}} \sigma d\varepsilon_{\text{in}} \quad (2.77)$$

where γ is a material constant, $m = 1$ if $\sigma_{\text{min}} > 0$ and $m = 0$ if $\sigma_{\text{min}} \leq 0$.

2.4.5 Empirical Models

Bernstein and colleagues [11] developed a model to predict the TMF life of industrial gas turbine blades. The model is a semi-empirical approach, similar to most engineering models that are actually used to predict LCF. The formulation does not attempt to separately model the different mechanisms (i.e., fatigue, creep, and environmental attack.)

Kanasaki and colleagues [12] have carried out axial-strain-controlled LCF tests of a carbon steel in oxygenated high-temperature water under TMF-IP and TMF-OP conditions. Based on the assumption that the fatigue damage increased in a linear proportion to the increment of strain during cycling, a fatigue-life prediction method was proposed.

CHAPTER 3

THERMAL AND STRESS ANALYSES

3.1 INTRODUCTION

The magnitudes, variations, and exposure times of the stresses and temperatures experienced are the major factors controlling the lives of jet engine components in service. The aim of thermal and stress analyses is to calculate these quantities because the application of damage models requires detailed knowledge of stress and temperature fields throughout a mission. Geometry and loading conditions are very complicated and material properties are temperature dependent. Therefore temperature and stress solutions can not be obtained analytically; numerical methods are used to get approximate solutions. Among these methods, finite element method is more suitable for computer implementation and for problems having geometrically complicated solution regions. This chapter will describe the region of the F110-GE-100 engine subject to study and the thermal and stress analyses performed on that region.

3.2 DESCRIPTION OF THE STRUCTURE ANALYZED

The F110-GE-100 augmented, mixed-flow, turbofan engine is an aerodynamically coupled, dual rotor machine consisting of a high-pressure system, an independent

mechanical low-pressure system and a variable area exhaust nozzle [50]. Engine operation is maintained by controlling the speed of a low-pressure rotor by regulating the high-pressure rotor speed to balance aerothermodynamic conditions. The first stage low pressure turbine (LPT) is the region of interest in this study and Figure 3.1 shows that region and its vicinity.

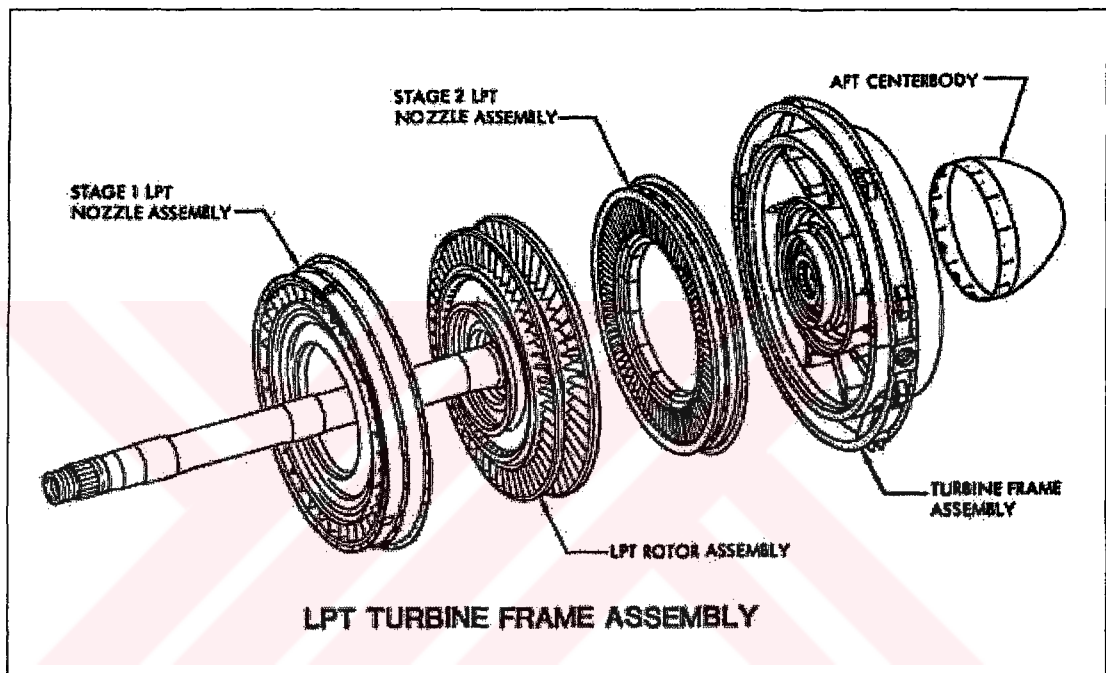


Fig 3.1 Low Pressure Turbine Frame Assembly

The low-pressure compressor section is composed of a three-stage fan driven by a two-stage low-pressure turbine. The high-pressure section is composed of a nine-stage compressor, an annular combustion chamber, and a single stage air-cooled high-pressure turbine.

During operation, air entering the engine is directed into the fan. The three-stage fan initially pressurizes the air and directs flow into the core engine and into the annular fan duct (bypass air). Air entering the core engine is compressed further

through the nine-stage compressor and is introduced into the annular combustor with fuel from twenty fuel nozzles. The fuel-air mixture is initially ignited by one of the two main spark igniters extending into the combustor. As combustion occurs, the expanding gases are directed into the turbine section to drive the single-stage high pressure turbine which powers the compressor, and into the two-stage low pressure turbine, which drives the fan. High and low pressure systems are mechanically independent of each other, but aerodynamically coupled. From the turbine section, the exhaust gases pass into the augmenter and are mixed with the fan stream flowing from the annular duct through the augmenter mixer. During augmented operation, fuel is sprayed into this mixed flow and ignited for additional thrust.

The flow rate of the fuel entering the combustion chamber is controlled by angular position of the engine power lever which is used by the pilot to adjust the power of the engine. Since the pilot of a fighter aircraft performs frequent and severe maneuvers throughout a mission, engine power lever angle (EPLA) changes frequently over a large range. In the engine, various components are integrated into the control system so that the entire engine responds to the positioning of the power lever. Therefore, EPLA is an important parameter to define the current state of the engine thermodynamically. As EPLA increases, more fuel and air are injected into the combustion chamber. As a result, temperature and pressure of the core gas flowing through the HPT and LPT increase as well as the mass flow rate and pressure of the various cooling airstreams. This action increases the thermal and mechanical loading on the engine components, usually at a high rate. As a result, various components try to expand, in particular, the outer band and impingement cover of the first stage LPT nozzle and the support for the same nozzle (Fig 3.2). The nozzle is connected to its support by 25 pins circumferentially (Figs 3.3 and 3.4). The nozzle and its support expand differentially in the radial and axial directions. In particular, axial expansions oppose each other. Such action creates bending in the pin. As EPLA travels between small and large values, a cyclic load

is applied to the pin, which causes an essentially Mode I crack to form and grow. Practical experience shows that these pins are critical components whose failure may have serious consequences.

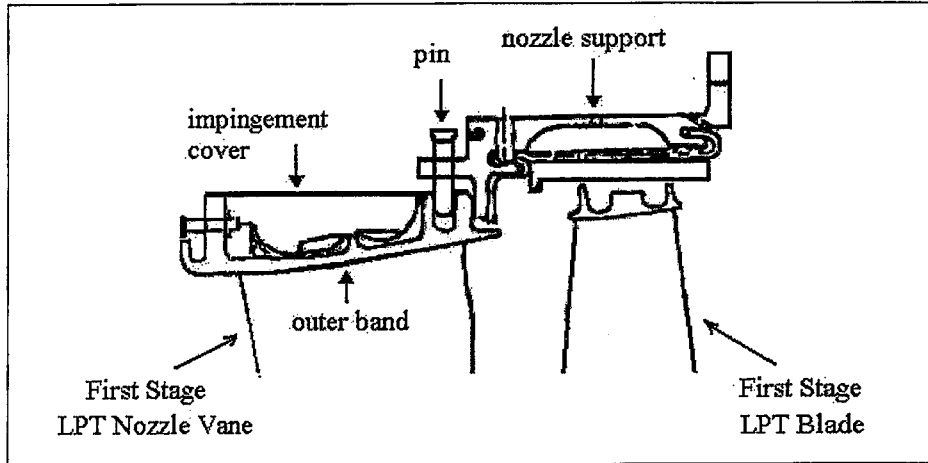


Fig 3.2 First Stage LPT Nozzle Outer Band, Impingement Cover and the Pin

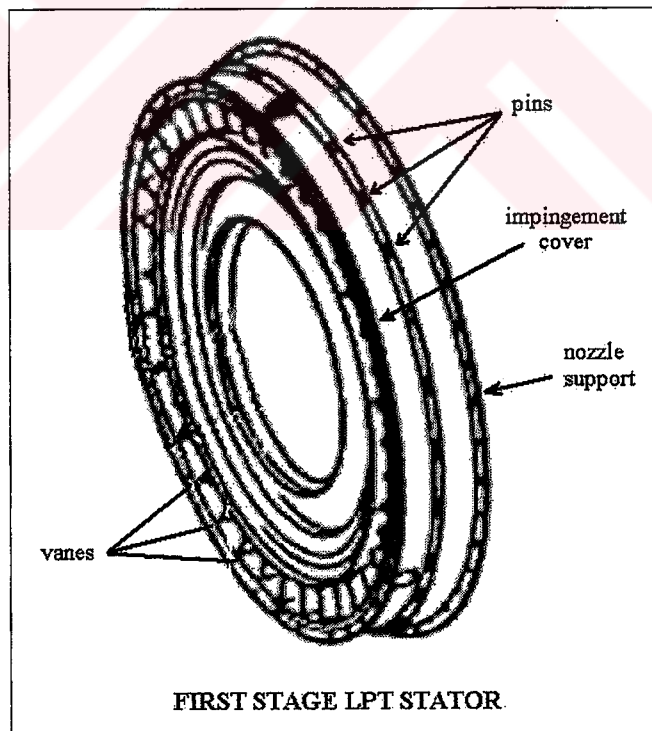


Fig 3.3 Nozzle, Nozzle Support and Pin

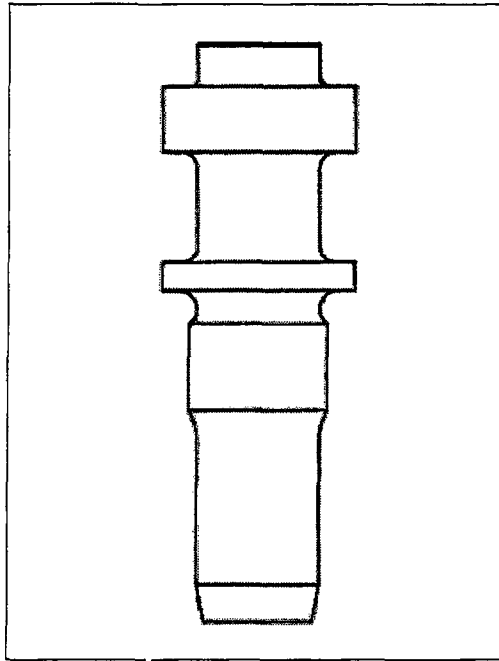


Fig 3.4 The Pin

3.3 FINITE ELEMENT METHOD

The fundamental concept of the finite element method is that any continuous field variable, such as stress, pressure or temperature can be approximated by a discrete model. The discrete model is composed of a set of piecewise continuous sections which are defined over a finite number of sub-domains of finite size known as elements. These elements are connected at specific points called nodes.

Variations of unknown field variables inside the continuum are described by approximate functions, which are also known as shape functions. These functions are defined in terms of the values the field variable at the nodal points. Field equations for every individual element are written and a set of unknowns representing the field values at the nodes is created. After assembly of the nodal values coming from different nodes, a set of equations is created. Unknown nodal values of the field variable are obtained by solving this system of equations.

3.4 THERMAL ANALYSIS

A two-dimensional (2-D) axisymmetric finite element model of the first stage LPT is generated with MARC for thermal analysis. After a stress analysis is performed, the critical region of interest is determined and a second set of models is generated for thermal analysis with a crack of varying lengths at the critical location. These models use gas stream temperatures and cooling air temperatures as boundary conditions in the thermal analysis. Convective heat transfer between the surrounding gas and the components, and heat conduction within the components are taken into account in the analysis to determine temperature variation in the components. Convection is taken into account by using gas stream and cooling air velocities.

The finite element model without crack is composed of 5830 elements. The element types used are the four-node, isoparametric, arbitrary quadrilateral element and the three-node, isoparametric, arbitrary triangular element written for axisymmetric heat transfer applications. These elements are Element Type 40, Axisymmetric Bilinear Quadrilateral Element, and Element Type 38, Arbitrary Axisymmetric Triangle in the element library of MARC. In Figure 3.5, finite element mesh of the engine components and the velocity vectors of gas stream flowing through the components are presented. The components in the figure from left to right are high pressure turbine (HPT) rotor, first stage LPT nozzle, LPT nozzle support, and LPT rotor.

Thermal analysis is performed to obtain the temperature history of our components at each phase of a given mission. In thermal analysis model, neighbouring components and assemblies are also included since they have effect on the temperature distribution of our component. The components included in the finite element models are HPT disk, HPT rotor blades, LPT stator, LPT disk, LPT rotor

blades, and shaft parts. Moreover, the surrounding gas flowing through the components is modeled with finite elements also.

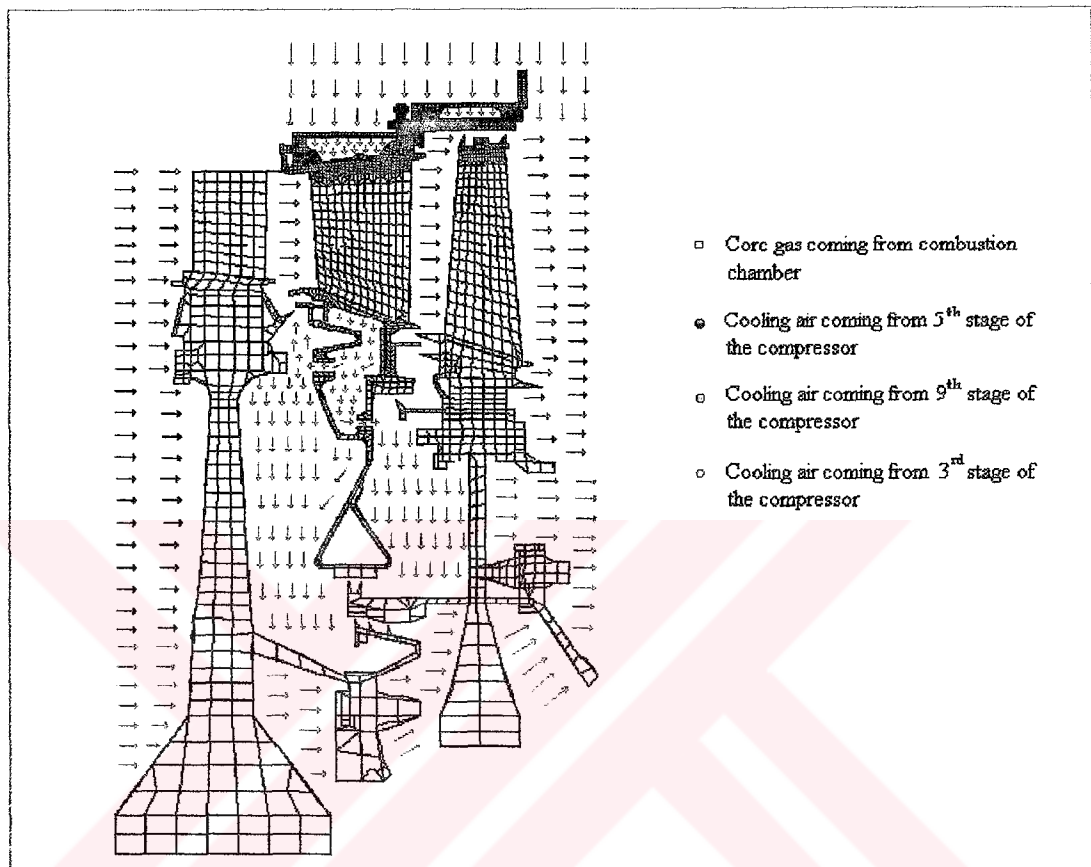


Figure 3.5 Finite Element Mesh of the Components and Velocity Vectors of Surrounding Gas

In order to solve convective heat transfer problems, MARC expects from the user to input either the convection coefficient or convective velocities. Convection coefficient is a function of fluid properties such as density, viscosity, thermal conductivity, and specific heat, as well as surface geometry and the flow conditions. For our problem, it is very difficult to find convection coefficient values. Therefore, it is decided to use convective velocities to handle the convective heat

transfer. For this purpose, convective velocities are applied to air nodes in the finite element models. In this mode, MARC solves the general convection-diffusion equation

$$\frac{\partial T}{\partial t} + \mathbf{v} \cdot \nabla T = \nabla \cdot (\kappa \nabla T + Q) \quad (3.1)$$

where \mathbf{v} is the velocity vector, T is the temperature, κ is the diffusion tensor, and Q is the source term.

All these components are modeled with axisymmetric finite elements, however blades of HPT rotor, LPT stator, LPT-rotor and pins are not axisymmetric. In view of thermal analysis, this ignores the effect of convective heat transfer from the core gas flowing through the rotors and stators tangentially to the blades. In order to handle this convective heat transfer in an axisymmetric model, the nodes of the elements of HPT rotor, LPT stator and rotor blades are assigned convective velocities. The calculation of the magnitudes of these velocities is given in Appendix A.

In thermal analysis, the velocities and the densities of gas stream and cooling air are necessary. These quantities are calculated by assuming uniform distribution of velocities on the cross-section through which gas flows and using continuity equation (3.2), and also assuming isentropic expansion of gases and using isentropic relations (3.3). The use of these equations requires the values of total and static pressures, temperatures and mass flow rates of the gases throughout the mission (See Appendix E). These quantities should be known to perform a thermal analysis. Moreover, initial temperatures of the gases are also needed in the analysis.

In the analysis, the velocities in a passageway are assumed unidirectional if the cross-section of the passage is uniform along the flow direction. If the walls of the passageway are not parallel to the main flow direction, the velocity vector in the

vicinity of the wall is assumed to be tangential (Fig. 3.5). Hence average velocity of convective air is

$$v_{ca} = \frac{\dot{m}}{\rho A} \quad (3.2)$$

where \dot{m} is the mass flow rate of gas, ρ is the density of the gas, and A is the cross-sectional area through which gas flows. Also,

$$\frac{P_0}{P} = \left[1 + \frac{\gamma-1}{2} M^2 \right]^{\frac{\gamma}{\gamma-1}} \quad (3.3)$$

where P_0 is the total pressure, P is the static pressure, γ is the ratio of specific heats which is around 1.3 for the hot gases involved and M is the mach number.

Mach number is calculated from

$$M = \frac{v_{ca}}{a} \quad (3.4)$$

where a is the local speed of sound which is calculated from

$$a = \sqrt{\gamma R T} \quad (3.5)$$

where R is the universal gas constant and T is the temperature.

To reiterate, P_0 , P , T and \dot{m} are assumed known. M and a are then computed from (3.3) and (3.5), from which v_{ca} is computed using (3.4) and, then, ρ is found from (3.2).

Temperature distributions calculated from thermal analysis are used both in stress analysis and creep damage assessment. Temperature distribution of whole model when EPLA reaches the maximum value of 130° for the first time in a certain mission type is given in Fig. 3.6.

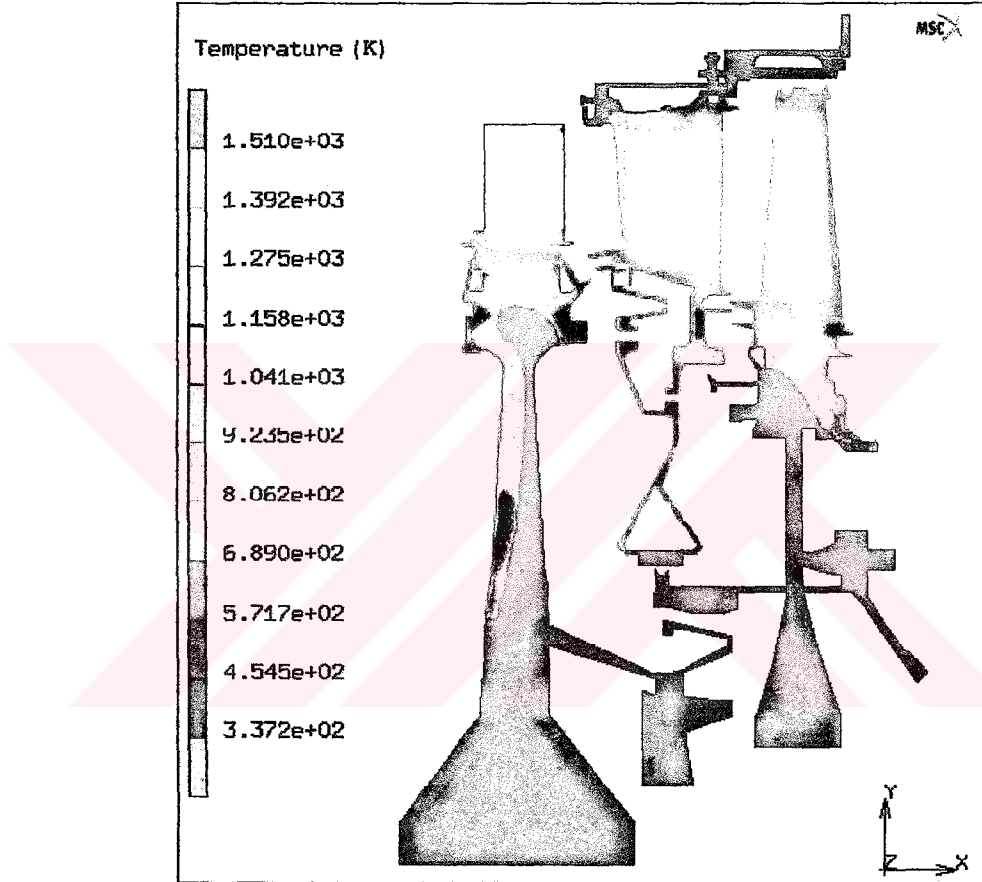


Figure 3.6 Temperature Distribution when EPLA = 130°

3.5 STRESS ANALYSIS

The same finite element meshes used in thermal analysis are also used in stress analysis with the same element class (four-node, isoparametric, arbitrary

quadrilateral element and three node, isoparametric, arbitrary triangular element) but the ones written for axisymmetric structural applications. Hence, the connectivities and the node coordinates are all the same. In stress analysis, gas stream and cooling air pressures, which are assumed known already (See Appendix E), and the thermal analysis results are used.

Since the stress analysis model is the same as the thermal analysis model, LPT rotor, LPT stator and rotor blades are modelled as axisymmetric components but in reality they are not axisymmetric; there are passageways through them. In view of stress analysis, this means that these components were modelled as more stiff than the real case. To account for this effect, a correction factor for the modulus of elasticity was introduced for axisymmetric case. The calculation of this correction factor is given in Appendix B.

MARC runs on a unix server called beluga which is located at METU-CC facilities and there is only 7 Gbytes of space for all users. Therefore a limited number of stages of the engine were modeled to keep the model size at a reasonable level. The question is then how to account for the structural effect of engine stages to the left and right of our model. Fixed displacement type boundary conditions were at first imposed at the interfaces with the rest of the engine. As expected, this resulted in much higher stresses than expected. Linear springs were then attached to the interface nodes.(Fig 3.7) In order to calculate the stiffness of these springs, the approach given in Appendix C was used.

Potentially most critical components of the engine in terms of thermo-mechanical fatigue life considerations are the combustion chamber and HPT blades, because these components are subjected to very high temperatures and temperature gradients. Although not subjected to high temperatures and temperature gradients, the pins, which connect the LPT nozzle support to the impingement cover, and which are of interest here, are also critical, since the pins are subjected to large

bending forces. Therefore, the mesh is fine around the pin, and much care is taken while modeling the connections around the pin. The components around the pin

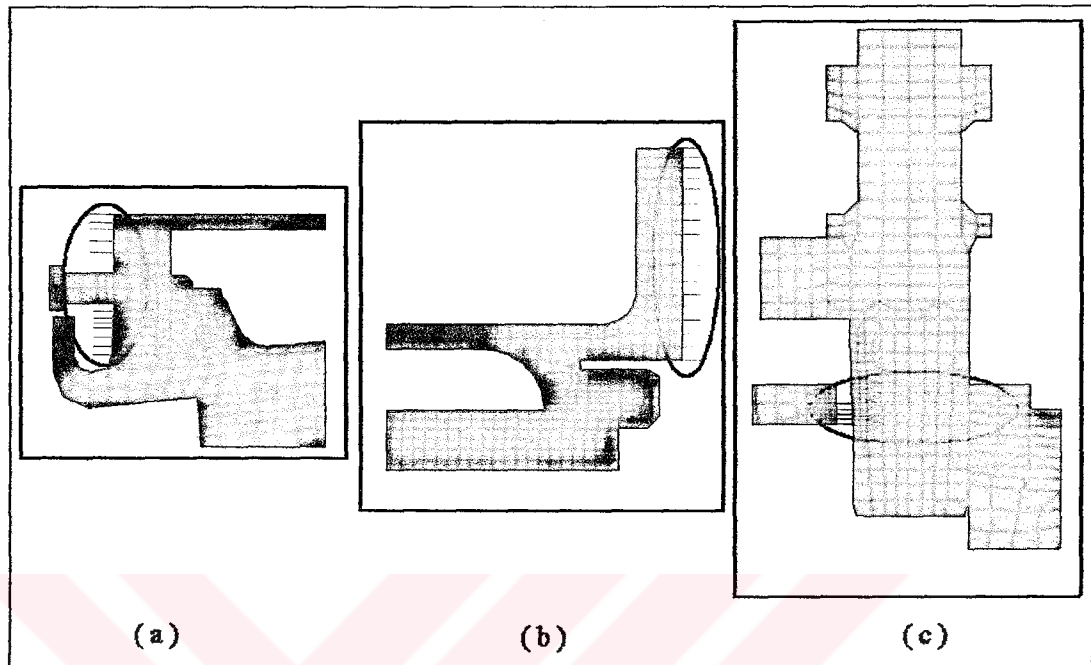


Fig 3.7 Springs Simulating the Parts not Modeled

and the pin itself was at first modeled as contact bodies. However, we faced with a problem while modeling the impingement cover and the pin as contact bodies. In order to overcome this problem we linked the impingement cover and the pin with axial and radial springs of the same stiffness. Calculations of the stiffness of these springs are given in Appendix C.

Combined with the mission profile the results of stress analysis are used to describe stress as a function of time and identify fracture critical locations based on the maximum principal stress at the pin.

CHAPTER 4

FRACTURE MECHANICS CALCULATIONS BY FEM AND LIFE ASSESSMENT

4.1 INTRODUCTION

The finite element method (FEM) has been employed extensively in fracture mechanics to model the singularity at a crack tip. In linear elastic fracture mechanics (LEFM, the determination of stress intensity factor (SIF) is often a major consideration and it has to be calculated as accurately as possible. Sections 4.2 and 4.3 describe the use of quarter point elements in FEM, and SIF calculation techniques by FEM, respectively. Section 4.4 describes fracture mechanics models generated. Finally, TMF life prediction by using AFGROW [51] is explained in Section 4.5.

4.2 USE OF QUARTER POINT ELEMENTS

A wide range of elements have been devised to simulate the stress singularity at the crack tip. One approach is to utilize singular elements, however many singular elements are difficult or impossible to incorporate into standard finite element

programs. Some cause displacement incompatibility between the singular and regular elements. In the past, several papers have appeared in the literature, which report on the application of singular point elements to fracture mechanics [39-48]. Among those, the quarter point element proposed by Barsoum [43,44] has found considerable popularity because of its simplicity and ease of implementation. By use of this element inverse square root singularity is obtained.

4.3 CALCULATION OF SIF BY FEM

In the calculations for FEM, a fit of the nodal displacements in the vicinity of the crack tip is used. The actual displacements at and near a crack for linear elastic materials are [34]

$$u = \frac{K_I}{4G} \sqrt{\frac{r}{2\pi}} \left((2\kappa - 1) \cos \frac{\theta}{2} - \cos \frac{3\theta}{2} \right) + \frac{K_{II}}{4G} \sqrt{\frac{r}{2\pi}} \left((2\kappa + 3) \sin \frac{\theta}{2} + \sin \frac{3\theta}{2} \right) \quad (4.1)$$

$$v = \frac{K_I}{4G} \sqrt{\frac{r}{2\pi}} \left((2\kappa + 1) \sin \frac{\theta}{2} - \sin \frac{3\theta}{2} \right) + \frac{K_{II}}{4G} \sqrt{\frac{r}{2\pi}} \left((2\kappa - 3) \cos \frac{\theta}{2} + \cos \frac{3\theta}{2} \right) \quad (4.2)$$

where u and v are displacements in x and y directions, respectively (Fig. 4.1) and

$$\kappa = 3 - 4\nu \quad (\text{for plain strain or axisymmetric cases})$$

$$\kappa = \frac{3 - \nu}{1 + \nu} \quad (\text{for plane stress case})$$

G is the shear modulus

Evaluating equations (4.1) and (4.2) at $\theta = -\pi$ and $\theta = \pi$ and solving for K_I and K_{II}

$$K_I = \frac{2G}{\kappa + 1} \sqrt{2\pi} \frac{\Delta v}{\sqrt{r}} \quad (4.3)$$

$$K_{II} = \frac{2G}{\kappa + 1} \sqrt{2\pi} \frac{\Delta u}{\sqrt{r}} \quad (4.4)$$

where $\Delta u = (u|_{\theta=\pi} - u|_{\theta=-\pi})$ and $\Delta v = (v|_{\theta=\pi} - v|_{\theta=-\pi})$.

One must be very careful while defining the local coordinate system. The x-axis must be along the crack and the y-axis must be perpendicular to the crack front. (Figure 4.1)

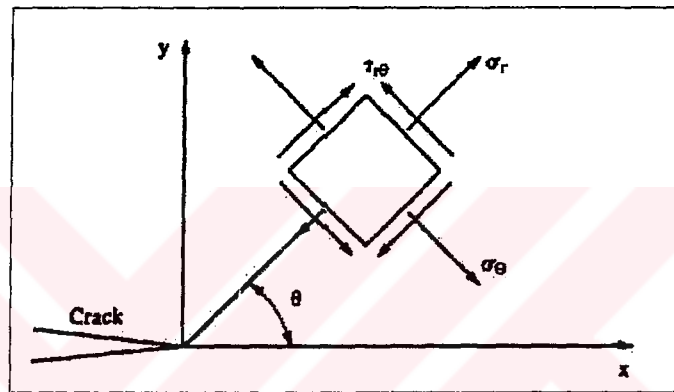


Figure 4.1 Local Coordinates Measured from a 2-D Crack Front

There are many SIF computation techniques from quarter point element displacements. In particular, displacement correlation, quarter point displacement, and displacement extrapolations techniques are popular in general LEFM analysis.

4.3.1 Displacement Correlation Technique (DCT)

In this approach, SIF is easily computed using [39]

$$K_I^{DCT} = \frac{G}{\kappa + 1} \sqrt{\frac{2\pi}{L_Q}} \{4(v'_B - v'_D) - (v'_C - v'_E)\} \quad (4.5)$$

$$K_{II}^{DCT} = \frac{G}{\kappa+1} \sqrt{\frac{2\pi}{L_Q}} \{4(u'_B - u'_D) - (u'_C - u'_E)\} \quad (4.6)$$

where L_Q is the length of quarter point element along the crack face, that is, $L_Q = |AC| = |AE|$, and u' and v' are the local displacements along and normal to the crack axis, respectively, as depicted in Fig. 4.2. The singularity in these elements is achieved by placing the mid-side node (i.e., nodes B and D) near the crack tip at the quarter point, that is the reason why these elements are called “quarter point elements”.

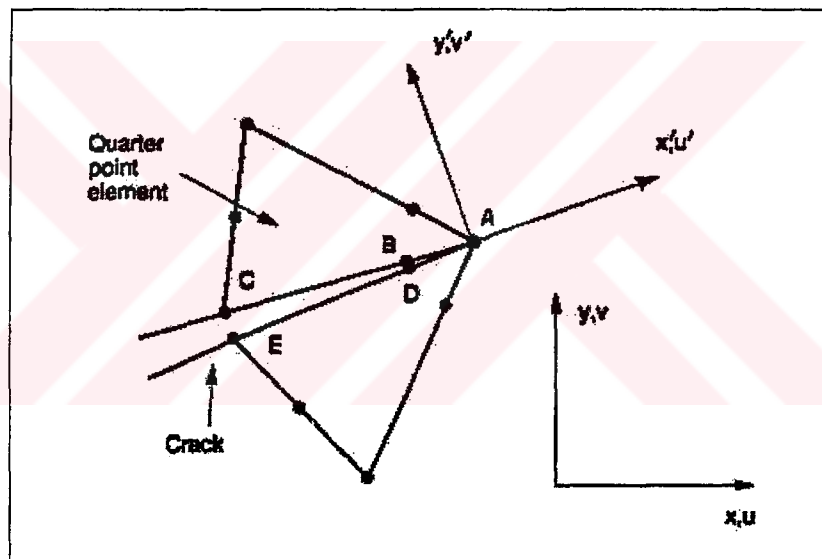


Figure 4.2 Nodal Lettering for SIF Computations

4.3.2 Quarter Point Displacement Technique (QPDT)

In this approach SIF is given by [39]

$$K_I^{QPDT} = \frac{2G}{\kappa+1} \sqrt{\frac{2\pi}{L_Q}} \{v'_B - v'_D\} \quad (4.7)$$

$$K_{II}^{QPDT} = \frac{2G}{\kappa + 1} \sqrt{\frac{2\pi}{L_Q}} \{u'_B - u'_D\} \quad (4.8)$$

4.3.3 Displacement Extrapolation Technique (DET)

In this technique, SIF values for the nodes B and D, and then C and E are calculated by using equations (4.3) and (4.4). After that, using these results SIF at the crack tip node is calculated by using direct extrapolation.

It was found that the QPDT generally performs better than the DCT [39]. It was also shown that the DET may produce erratic performance because of its sensitivity to both the distribution of nodes along the crack face and the variation of SIF at each node. Therefore, we decided to use QPDT to calculate SIFs.

4.4 FRACTURE MECHANICS MODELS GENERATED

Stress analysis of the model without crack indicated that the critical location in our component is the pin surface in contact with the impingement cover (Figs 3.2 and 4.3). A set of models were then generated for fracture mechanics calculation purposes. A crack of varying lengths, the propagation angle of which is determined by using the Maximum Tangential Stress Criterion (MTS) explained in Chapter 2, is modeled by MARC. The aim of crack modeling is to calculate geometry factors (or β factors) for various lengths of a crack. After β factors are determined, fatigue life calculations can be easily performed by a crack growth calculation program such as AFGROW, which is used in this study.

As previously mentioned in Chapter 2, SIF can be expressed as

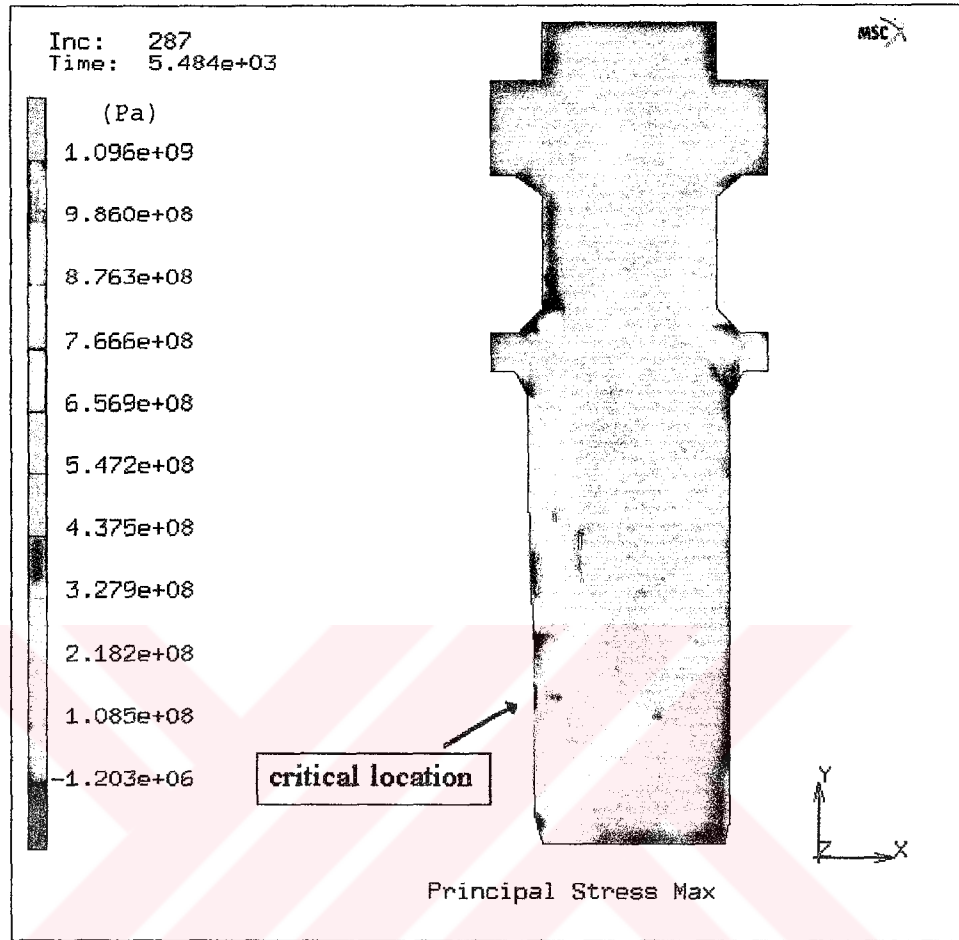


Figure 4.3 The Critical Location from Where a Crack is Expected to Initiate
(x axis points to aft of the engine)

$$K = \beta \sigma \sqrt{\pi a} \quad (2.13)$$

where β is the geometry factor, σ is the stress applied, and a is the crack length.

Since we have a multiaxial state of stress, the question is what will be the value of the reference stress σ . In calculations of crack propagation direction, MTS was used, hence it is thought to be a good idea to take the reference stress value as the

maximum tangential stress value. After performing stress analysis of no-crack models, it was seen that the maximum tangential stress is the maximum principal stress. The maximum stress variation through the mission profile under investigation is given in Figure 4.4. The numerical values of maximum principal stress profile are given in Appendix E.

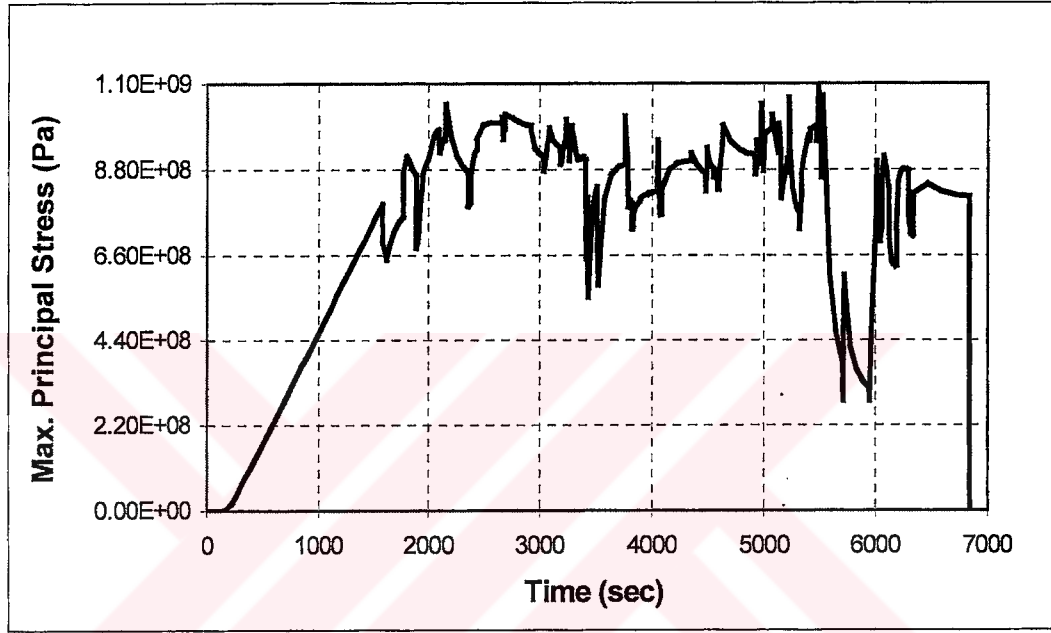


Figure 4.4 Maximum Principal Stress Profile of the Critical Location

For a set of crack lengths at the peak of the EPLA history during the mission, which occurs at $t = 1905$, the mode I and mode II SIFs were calculated using equations (4.5) and (4.6). After calculating those, an effective SIF is calculated using equation (2.19). Then, β factors were calculated using equation (2.13). As a check, for the same crack lengths β factors were then calculated at various other principal stress values. For a given crack length, β value was nearly the same under different stresses. It was expected since β factors reflect the effect of geometry to crack propagation. It means that β factors are only functions of geometry and are

models for all mission profile. Eleven different crack lengths were used to establish the dependence of β on crack length. Effective SIF and β variations with crack length are shown in Figures 4.5 and 4.6, respectively.

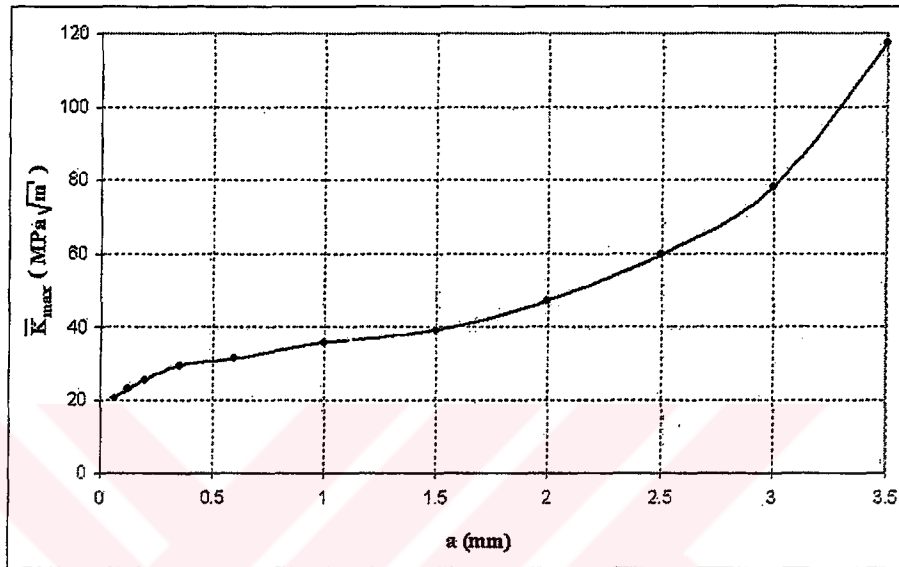


Figure 4.5 Maximum Effective SIF Variation with Crack Length

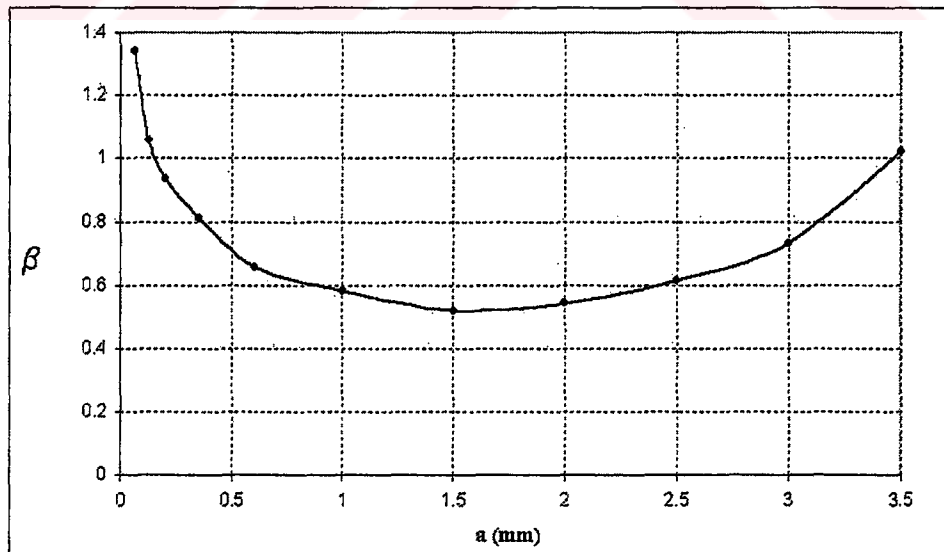


Figure 4.6 β Factor Variation with Crack Length

Although the crack changes its direction while it grows (Figure 4.7), the crack propagation was simulated as mode I type using the effective SIF.

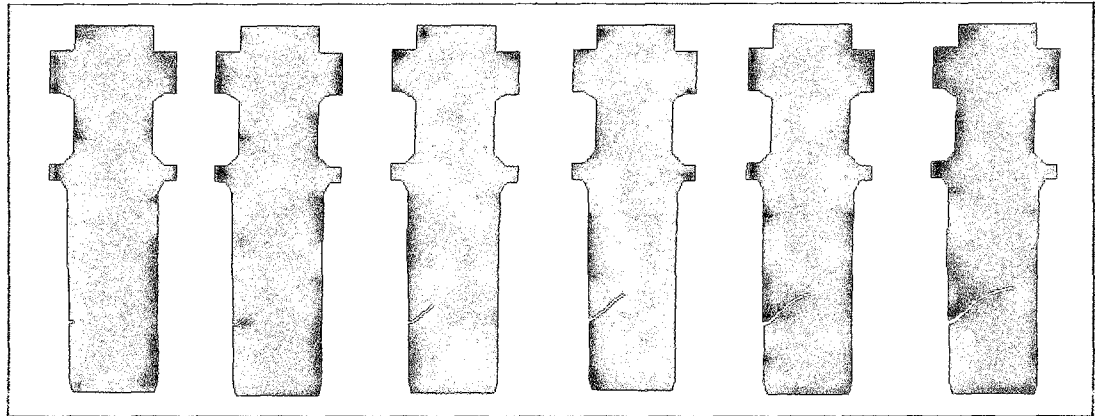


Figure 4.7 Crack Growth Direction Changing with Time

In the models, eight-noded quarter-point elements were used while modeling the cracks. SIF calculations are performed using the Quarter Point Displacement Technique (QPDT) that was explained in Section 4.2.2, since this technique can predict SIF with less than 1% error [39] if the quarter point element length (L_Q) is taken around 1/10 of the crack length. Therefore, while modeling the cracks in our models, L_Q / a ratio is kept around 1/10.

4.5 TMF LIFE PREDICTION BY AFGROW

Thermo-Mechanical Fatigue (TMF) life prediction techniques are described in Chapter 2. Among those, the model proposed by Chen and his colleagues (Section 2.4.1) [6], which is a linear damage summation method to predict the fatigue and creep-fatigue behaviour of a nickel-based superalloy at high temperature, is used here because this model is easy to implement and can be successively used in conjunction with AFGROW, which has a capability to include time dependence

conjunction with AFGROW, which has a capability to include time dependence effects in life assessment calculations. Moreover, other models require quite a few material properties that should be calculated from experiments and we don't have such data available.

In order to perform a fatigue life prediction; AFGROW expects the user to specify material properties, dimensions of geometry, crack type, stress spectrum and retardation model.

AFGROW has a broad material property database. Apart from other material properties such as yield strength, fracture toughness, and Poisson's ratio, da/dN vs. ΔK data are also included for a variety of materials.

SIF solutions for some simple geometries are included in AFGROW. A user may choose one, which is suitable for his problem, or may use his own β factors. We calculated β factors with MARC and input these values to AFGROW.

AFGROW offers the user a choice to specify the stress state. Since crack growth rates are larger in plain strain case and the pin has a fairly large diameter (4.3 mm), we specified the stress state as plain strain. Crack is assumed to be a through the thickness type of crack, which means that once the crack growth starts it extends through the thickness.

In this study, initial crack size is chosen as NDI minimum detectable flaw size, which is around 0.015 inches (0.381 mm). The maximum principal stress history at the critical point of the pin obtained from the no-crack model is input as the stress profile.

Fatigue life (N_f) predictions were performed for three cases, namely no-retardation, closure model with OLR of 0.3 (commonly taken value for most metals), and Willenborg model with SOLR of 2.5 (AFGROW's default value). The results are given on Table 4.1, and crack growth curves are shown in Fig. 4.7.

Table 4.1 Fatigue Life Prediction Results

Case	Fatigue Life (N_f)
No-retardation	4837 hours
Closure Model (OLR = 0.3)	4919 hours
Willenborg Model (SOLR = 2.5)	5136 hours

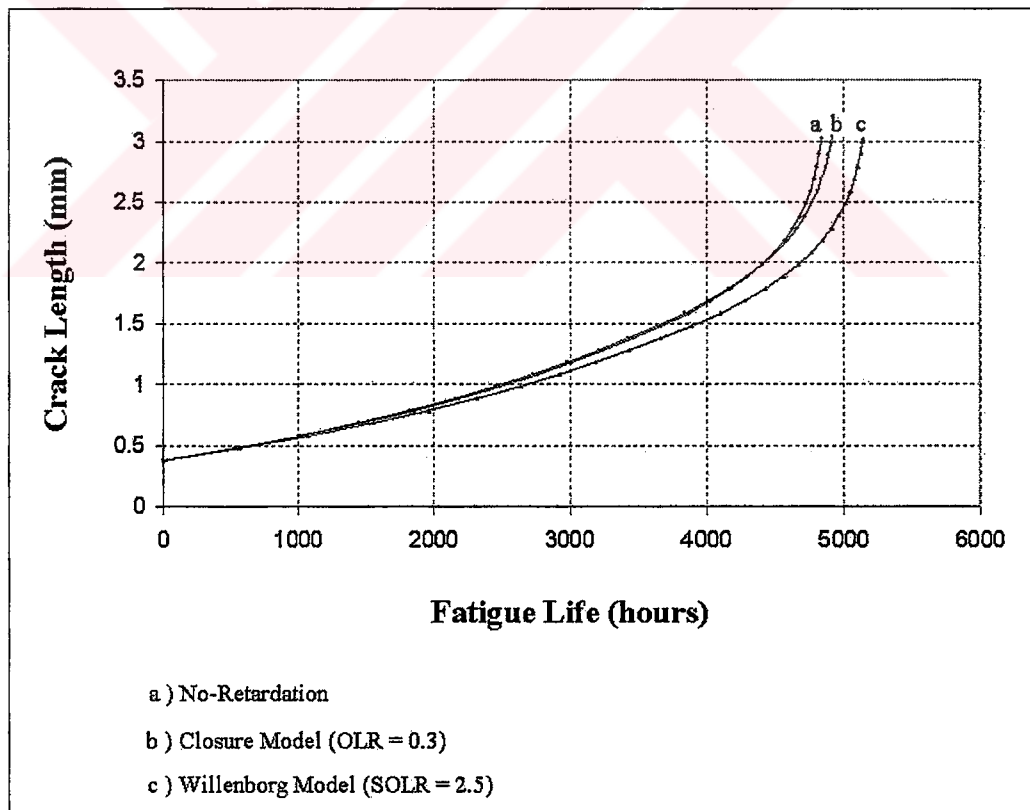


Figure 4.8 Fatigue Crack Growth Curves

Creep rupture time (t_r) of the component was calculated by invoking the time dependence option of AFGROW. Before starting calculations, hold periods of the maximum principal stress profile of the critical location were determined (Table 4.2), and creep life calculations were performed for these hold periods. AFGROW expects the user to supply steady-state creep crack growth rate (\dot{a}) vs. stress intensity factor (K) data. For the hold periods of the maximum principal stress history, temperature values were 581 K, 601 K, 638 K, 600 K, 437 K and 430 K, respectively. However, in literature we could find creep crack growth data for the pin material of our component, namely Inconel 718 (a nickel-base superalloy), for the temperature values of 537 °C (810 K), 593 °C (866 K), and 649 °C (922 K) [49]. The creep data is unavailable for temperatures the pin was subjected to because these temperature values are smaller than the half of the melting temperature of the pin material (in the range 1533-1608 K). Creep crack growth data was extrapolated to these temperatures by following the approach explained in Appendix D. After extrapolating creep data creep rupture times (t_r) were calculated corresponding to the hold periods. The results are shown in Table 4.3.

Table 4.2 Hold Periods

Hold Periods (sec)	Hold Times (t_h) (sec)	Maximum Principal Stress (MPa)	Corresponding Temperature (K)
2490 – 2920	430	1000	581
3940 – 4044	104	820	600
4220 – 4347	127	900	638
5412 – 5466	54	985	600
6231 – 6297	66	878	437
6345 – 6834	489	820	430

Table 4.3 Creep Rupture Time Results

Hold Periods (sec)	Hold Times (t_h) (sec)	Creep Rupture Times (t_r) (hours)
2490 – 2920	430	511 111
3940 – 4044	104	236 167
4220 – 4347	127	36 667
5412 – 5466	54	206 667
6231 – 6297	66	$3.2 \cdot 10^9$
6345 – 6834	489	$5.5 \cdot 10^9$

After determining hold periods and calculating creep rupture times corresponding to these stress and temperature values, thermo-mechanical fatigue (TMF) life of the component was assessed by using equation (2.56) for the same three cases performed for fatigue life calculations. TMF life prediction results for three cases are given on Table 4.2.

$$N = \frac{1}{\left[\frac{1}{N_f} + \frac{t_h}{t_r} \right]} \quad (2.56)$$

Comparing these results with fatigue life (N_f) prediction results it is seen that the values are very close to each other (Table 4.4). It was expected because the temperatures the pin was subjected was smaller than the half of the melting temperature of the pin material, that is, creep is not an effective damage mechanism at these temperatures.

Table 4.4 TMF Life Prediction Results

Case	Fatigue Life (N_f)	TMF Life (N)	% change
No retardation	4837 hours	4820 hours	-0.35
Closure Model (OLR = 0.3)	4919 hours	4902 hours	-0.35
Willenborg Model (SOLR = 2.5)	5136 hours	5116 hours	-0.39

MIL-STD-1783, ENSIP (Engine Structural Integrity Program), which was issued in 1984 by the United States Air Force, states that all engine critical parts are to be designed to twice the life requirement. When retardation effects were neglected, TMF life of the pin was calculated as 4820 hours, and therefore, the pins should be replaced at 2410 hours. The component retirement time given by Turkish Air Force is around 1500-1800 hours. Therefore the predicted TMF results is a reasonable value. We calculated a larger value compared to retirement time given by Turkish Air Force, and this is meaningful since the pins should be removed before the whole life of the pins are spent.

CHAPTER 5

CONCLUSION

In this thesis, thermo-mechanical fatigue life of pins connecting the first stage low pressure turbine (LPT) nozzle to the LPT nozzle support in a F110-GE-100 engine has been assessed.

Firstly, a 2-D axisymmetric finite element model of a segment of F110-GE-100 engine was generated by using MARC for thermal analysis. This is the engine used to power a large number of F-16 aircraft in Turkish Air Force. The segment of the engine modeled included the high pressure turbine (HPT), first stage LPT, nozzle and its support, and shaft parts. The analysis was performed over a typical sortie in a fleet and temperature history was obtained.

The same model and the output of thermal analysis were then used in a stress analysis to determine the most critical location in the component of interest, namely the pin. Since the stress model is axisymmetric, the materials of non-axisymmetric components were modeled as transversely isotropic and a correction factor for the modulus of elasticity was introduced to include 3-D effects. To simulate the structural effect of the rest of the engine on the modeled region, linear elastic springs were placed at the extreme left and right of the model.

After determining the critical location, a crack of varying lengths was modeled by using MARC. Mode I and II stress intensity factor, cumulative crack propagation angle and geometry factor β were calculated for each crack length. Functional dependence of β on crack length was thus established.

Calculated β factors and the maximum principal stress profile of the critical location without the crack were used to predict the fatigue crack propagation life by using AFGROW.

Creep life prediction was performed by extrapolating the creep crack growth rate data obtained from literature to the temperatures critical region of the pin was subjected to.

After calculating fatigue life (N_f) and creep rupture time (t_r) of the component, thermo-mechanical fatigue life prediction was assessed by using a linear damage accumulation model. Thermo-mechanical fatigue life calculated is a reasonable value compared to the component retirement time given by Turkish Air Force.

Recommendations for a Future Study

Several improvements can be made in the study. The most significant improvement would be to extend the finite element model to 3-D. The next improvement could be the modeling of a larger region of the engine. This would put the boundaries of the model further away from the pin, thus reducing the structural effect of boundary conditions on the stress results. Springs were used at the boundaries of the present model. The stiffness of these springs has a significant effect on the stress results. There are two sets of large bolts far away from the pins investigated (Fig. C.1 in App. C). Extending the model up to these bolts and imposing the boundary conditions at those bolts would improve accuracy in the computed stresses. Another improvement would be to find better creep data for the pin material.

REFERENCES

1. Cai, C., Liaw, P.K., Ye, M., and Yu, J., "Recent Developments in the Thermomechanical Fatigue Life Prediction of Superalloys," *Journal of Materials*, vol. 51, no. 4, April 1999.
URL : <http://www.tms.org/pubs/journals/JOM/9904/Cai/Cai-9904.html>
2. H. Sehitoglu, "Thermo-Mechanical Fatigue Life Prediction Methods," *Advances in Fatigue Lifetime Predictive Techniques*, ASTM STP 1122, pp. 47-76, 1992.
3. Neu, R. and Sehitoglu, H., "Thermomechanical Fatigue, Oxidation and Creep: Part 1 – Experiments," *Met. Trans. A*, 20A, pp. 1755-1767, 1989.
4. Neu, R. and Sehitoglu, H., "Thermomechanical Fatigue, Oxidation and Creep: Part 2 – Life Prediction," *Met. Trans. A*, 20A, pp. 1769-1783, 1989.
5. Sehitoglu, H. and Boismier, D.A., "Thermo-Mechanical Fatigue of Mar-M247: Part 2 – Life Prediction," *J. Eng. Mat. And Tech.*, vol.112, pp. 80-89, 1990.
6. Chen, L.J. et al, "Fatigue and Creep-Fatigue Behaviour of a Nickel-Base Superalloy at 850°C," *International Journal of Fatigue*, vol. 20, no. 7, pp. 543-548, 1998.
7. Miller, M.P. et al., "A Life Prediction Model for Thermomechanical Fatigue Based on Microcrack Propagation," *ASTM STP 1186*, 1993, pp. 35-49.

8. Manson, S.S., Halford, G. R., and Hirschberg, M.H., "Creep Fatigue Analysis by Strain-Range Partitioning," First Symposium on Design for Elevated Temperature Environment, pp.12-24, 1971.
9. Manson ,S.S., "The Challenge to Unify Treatment of High-Temperature Fatigue – A Partisan Proposal Based on Strain Range Partitioning," Fatigue at Elevated Temperatures, ASTM STP 520, pp. 744-782, 1973.
10. Nissley, D.M., "Thermomechanical Fatigue Life Prediction in Gas Turbine Superalloys: A Fracture Mechanics Approach," AIAA Journal, vol. 33, no. 6, pp. 1114-1120, 1995.
11. Bernstein, H.L. et al., "Prediction of Thermal-Mechanical Fatigue Life for Gas Turbine Blades in Electric Power Generation," Thermomechanical Fatigue Behaviour of Materials, ASTM STP 1186, pp. 212-238, 1993.
12. Kanasaki, H. et al., "Corrosion Fatigue Behaviour and Life Prediction Method under Changing Temperature Condition," Effects of the Environment on the Initiation of Crack Growth, ASTM STP 1298, pp. 267-281, 1997.
13. Basquin, O. H., "The Exponential Law of Endurance Tests," Am. Soc. Test. Mater. Proc, vol. 10, pp. 625-630, 1910.
14. Coffin, L. F. Jr., "A Study of the Effects of Cyclic Thermal Stresses on a Ductile Metal," Trans. ASME, vol. 76, pp. 931-950, 1954.
15. Manson, S. S., "Behaviour of Materials under Conditions of Thermal Stresses," Heat Transfer Symposium, University of Michigan Engineering Research Institute, pp. 9-75, 1953.

16. Morrow, J., "Fatigue Design Handbook," Advances in Engineering, vol. 4, Society of Automotive Engineers, Warrendale, Pa., Sec. 3.2, pp. 21-29, 1968.
17. Manson, S. S. and Halford, G. R. "Practical Implementation of the Double Linear Damage Rule and Damage Curve Approach for Treating Cumulative Fatigue Damage," Int. J. Fracture, vol. 17, no. 2, pp.169-172, R35-R42, 1981.
18. Smith, K. N., Watson, P. and Topper, T. H., "A Stress-Strain Function for the Fatigue of Metals," J. Mater., vol. 5, no. 4, pp. 767-778, 1970.
19. Erdogan, F. and Sih, G.C., "On the Crack Extensions in Plates under Plane Loading and Transverse Shear," Journal of Basic Engineering, ASME Transactions, vol. 91, pp. 764-769, 1963.
20. Sih, G. C., "Strain Energy Density Factor Applied to Mixed Mode Crack Problems," International Journal of Fracture, vol. 10, pp. 305-321, 1974.
21. Hellen, T. K. and Blackburn, W. S., "The Calculation of Stress Intensity Factors for Combined Tensile and Shear Loading," International Journal of Fracture, vol. 11, pp. 605-617, 1975.
22. Dowling, N. E., "Fatigue Failure Predictions for Complicated Stress-Strain Histories," Journal of Materials, ASTM, Vol. 7, No. 1, Mar., pp. 71-87, 1972.
23. Burns, A., "Fatigue Loadings in Flight: Loads in the Tailplane and Fin of a Varsity," Aeronautical Research Council Technical Report C.P. 256, London, 1956.

24. Matsuishi, M. and Endo, T., "Fatigue of Metals Subjected to Varying Stress," paper presented to Japan Society of Mechanical Engineers, Fukuoka, Japan, March 1986.
25. van Dijk, G. M., "Statistical Load Data Processing," paper presented at Sixth ICAF Symposium, Miami, Florida, May 1971.
26. Downing, S. D., and Socie, D. F., "Simplified Rainflow Counting Algorithms," International Journal of Fatigue, Vol. 4, No. 1, pp. 23-29, Jan 1982.
27. Palmgren, A., Ball and Roller Engineering, translated by G. Palmgren and B. Ruley, SKF Industries, Inc., Philadelphia, pp. 82-83, 1945.
28. Miner, M. A., "Cumulative Damage in Fatigue," ASME Journal of Applied Mechanics, Vol. 12, Sept., pp. A 159-164, 1945.
29. Wheeler, O. E., "Spectrum Loading and Crack Growth", Journal of Basic Engineering, 94 D, p. 181, 1972.
30. Willenborg, J. D., et al, "A Crack Growth Retardation Model Using an Effective Stress Concept," AFFDL-TM-71-1 FBR, 1971.
31. Elber, W., "The Significance of Fatigue Crack Closure," Damage Tolerance in Aircraft Structures, ASTM STP 486, pp. 230-242, 1971.
32. Habibie, B. J., "Fatigue Crack Growth Prediction", Messerschmidt-Bolkow-Blohm, Report No. Uh-03-71, 1971.
33. Hanel, J. J., "Crack Growth Prediction Under Variable Amplitude Loading on the Basis of a Dugdale Model," German Society for Materials Testing, 1973.

34. Bell, P. D., and Creager, M., "Crack Growth Analysis for Arbitrary Spectrum Loading", AFFDL-TR-74-129, 1975.
35. Broek, D., "Elementary Engineering Fracture Mechanics," Noordhoff, Leyden Holland, 1974.
36. Gallagher, J.P., "A Generalized Development of Yield Zone Models," AFFDL-TM-FBR 74-28, 1974.
37. Hayhurst, D.R. and Leckie, F.A., "Mechanical Behaviour of Materials, Proc. ICM4," vol 2, p.1195, Pergamon Press, Oxford, 1984.
38. Nix, W.D., Earthman, J.C., Eggeler, G., and Ilschner, B, "The Principal Facet Stress as a Parameter for Predicting Rupture Under Multiaxial Stresses," Acta Metall., vol. 37, no. 4, pp. 1067-1077, 1989.
39. Lim, I.L. and Johnston, I.W., "Comparison Between Various Displacement-Based Stress Intensity Factor Computation Techniques," International Journal of Fracture, vol.58, pp. 193-210, 1992.
40. Chan, S.K. and Tuba, I.S., "On the Finite Element Method in Linear Fracture Mechanics," Engineering Fracture Mechanics, vol. 32, pp.1-17, 1970.
41. Banks-Sills, L. and Sherman, D., "Comparison of Methods for Stress Intensity Factors with Quarter-Point Elements," International Journal of Fracture, vol.32, pp.127-140, 1986.
42. Lynn, P.P. and Ingraffea, A.R., "Transition Elements to be Used with Quarter-Point Crack-Tip Elements", Short Communications, pp.1031-1036, 1977.

43. Barsoum, R.S., " On the Use of Isoparametric Finite Elements in Linear Fracture Mechanics," International Journal for Numerical Methods in Engineering, vol. 10, pp.25- 37, 1976.
44. Barsoum, R.S.," Triangular Quarter-Point Elements as Elastic and Perfectly-Plastic Crack Tip Elements," International Journal for Numerical Methods in Engineering, vol.11, pp. 85-98, 1977.
45. Peano, A. and Pasini, A., "A Warning against Misuse of Quarter-Point Elements," John Wiley & Sons Ltd., 1982.
46. Ingraffea, A.R. and Manu, "Stress-Intensity Factor Computation in Three Dimension with Quarter-Point Elements," International Journal for Numerical Methods in Engineering, vol.15, pp.1427-1445, 1980.
47. Banks-Sills, L. and Bortman, Y., "Reappraisal of the Quarter-Point Quadrilateral Element in Linear Elastic Fracture Mechanics," vol.25, pp.169-180, 1984.
48. Zienkiewicz, O.C., "The Finite Element Method," McGraw Hill Company, 1977
49. Haritos, G.K., Miller, D.L., and Nicholas, T., "Sustained-Load Crack-Growth in Inconel 718 Under Nonisothermal Conditions," Journal of Engineering Materials and Technology, vol 107, pp.172-179, 1985.
50. "F-110-100 Student Workbook, Basic Engine," General Electric Aircraft Engine, Evendale Technical Training School, August 1989.
51. "AFGROW, A Structural Life Prediction Program,"
URL : "<http://fibec.flight.wpafb.af.mil/fibec/afgrow.html>"

APPENDIX A

CALCULATION OF CONVECTIVE VELOCITIES GIVEN TO THE BLADE NODES

In order to include the effect of convective heat transfer from surrounding air to high pressure turbine (HPT) rotor, low pressure turbine (LPT) stator and LPT rotor blades, convective velocities were given to the nodes of these solid components in the finite element model for thermal analysis. The values of these convective velocities were determined as follows.

First, 3-D finite element models of each of these three components were generated in MARC to perform a thermal analysis. In these models, both the component itself and the surrounding air were included. The blades were modeled as constant thickness plates. Plate thickness was taken as the maximum value of the blade thickness. In the thermal analysis, temperatures and velocities of gas at the inlet and at the outlet of the blades and velocity of air flowing through the blades were kept constant at the values corresponding to the EPLA value. Then, at three chosen engine power lever angle (EPLA) values, namely at 26°, 80°, and 130°, transient thermal analysis was performed to calculate the temperature distribution within the plate. The finite element mesh used for thermal analysis is given in Figure A.1

Temperature distribution in the midplane of the plate simulating LPT stator vane at an EPLA of 130° with the thermal loading explained above is given in Figure A.2.

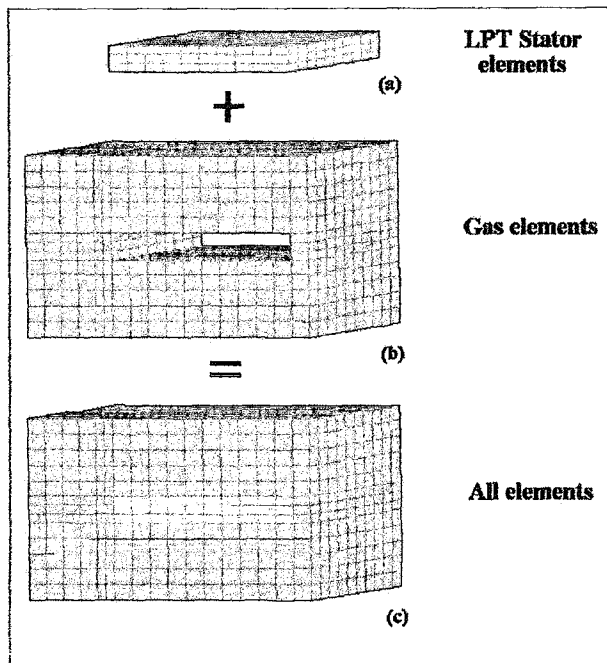


Figure A.1 3-D Finite Element Mesh
(a) LPT stator elements (b) Gas elements (c) All elements

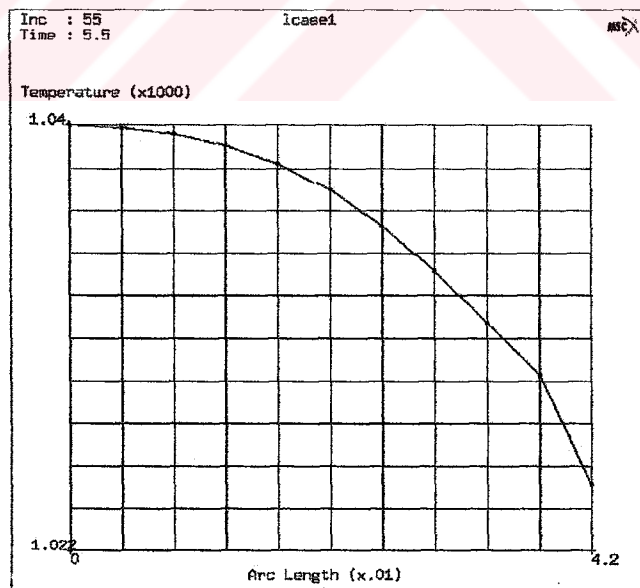


Figure A.2 Temperature Distribution in the Midplane of the Plate in Fig A.1 (a)

After that, 2-D axisymmetric finite element models of the components were generated. In these models, both the component itself and gas at the inlet and outlet of the blades were included. Since the models are axisymmetric there is no chance to model gas flowing through the blades. In the thermal analysis, the temperatures and velocities of gas at the inlet and outlet of the blades were kept constant same as in the case of 3-D models. In order to take convective heat transfer effect of gases flowing through the blades convective velocities were given to blade nodes. The value of these convective velocities was determined by trying to equate the temperature distribution of the blades to the one obtained from 3-D thermal analysis. . The relationship between the convective velocities given to blade nodes in axisymmetric model (v_{blade}) and the convective velocities given to gas nodes in 3-D models (v_{gas}) is:

$$v_{blade} = 2.5 \cdot 10^{-5} v_{gas} \quad (A.1)$$

The finite element mesh used for thermal analysis is given in Figure A.3.

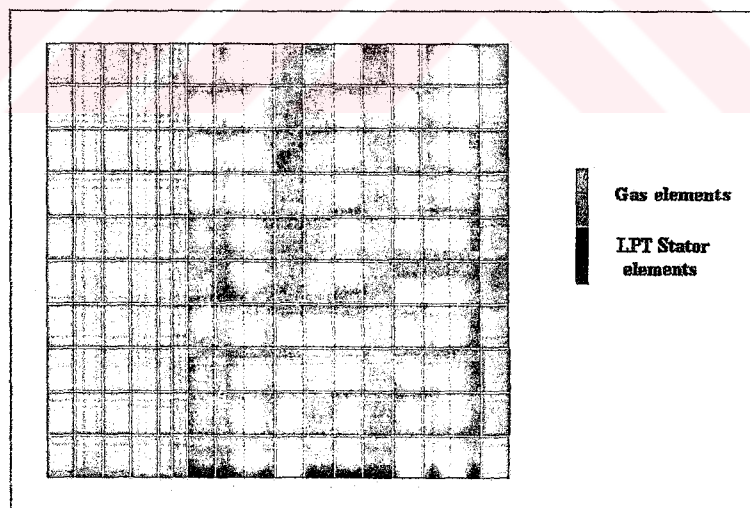


Figure A. 3 2-D Axisymmetric Finite Element Mesh

Temperature distribution along midplane of the plate obtained from thermal analysis of LPT stator vane is given in Figure A.4.

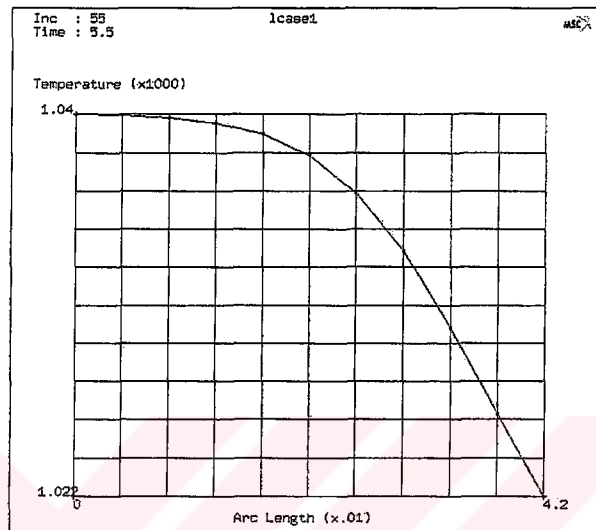


Figure A. 4 Temperature Distribution of the Midplane of the Plate with Convective Velocity Given to the Plate Nodes

Temperature distribution along midplane of the plate obtained from thermal analysis of LPT stator vane with no convective velocities imposed to the nodes of the plate is given in Figure A.5.

The approach followed here has no physical basis, however the effect of convective velocities given to the nodes of the blades is necessary to simulate the convective heat transfer. This is a peculiarity of MARC.

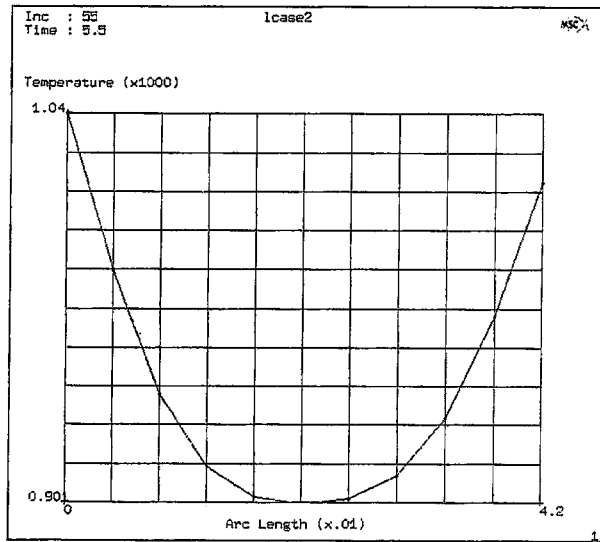


Figure A. 5 Temperature Distribution of the Midplane of the Plate with No Convective Velocity Given to the Plate Nodes

APPENDIX B

CORRECTION FACTOR FOR MODULUS OF ELASTICITY OF THE BLADES IN AXISYMMETRIC AN MODEL

HPT rotor, LPT stator and rotor blades were modelled as axisymmetric components but in reality they are not axisymmetric. This means that these components are modeled as more stiff than they really are. Therefore, a correction factor for the modulus of elasticity was introduced to account for this effect. In order to calculate this correction factor, the extensional stiffness of the blades, namely area multiplied with the modulus of elasticity is kept constant. Hence, an effective modulus of elasticity is calculated as

$$E_{\text{eff}} = \frac{A_{\text{blade}}}{A_{\text{solid}}} E_{\text{blade}} \quad (\text{B.1})$$

where E_{eff} is the value of the modulus of elasticity that was used in an axisymmetric model, E_{blade} is the actual value of the modulus of elasticity of the blade material, A_{solid} is the cross-sectional area normal to the engine axis in an axisymmetric model, and A_{blade} is the total cross-sectional area of the blades normal to the engine axis in the actual three-dimensional case. Then, the required correction factor is the ratio $\frac{A_{\text{solid}}}{A_{\text{blade}}}$.

The cross-sectional areas of the blades in axisymmetric modeling and actual three-dimensional case are calculated as

$$A_{\text{solid}} = \pi(r_o^2 - r_i^2) \quad \text{and} \quad A_{\text{blade}} = (r_o - r_i)t_{\text{blade}} N_{\text{blade}} \quad (\text{B.2})$$

where N_{blade} is the number of blades, t_{blade} is the maximum thickness of the blades, r_o and r_i are the radial position of the outermost and innermost points on the blades, respectively.

- Correction factor for HPT rotor blades

Substituting the values $r_i = 0.31957$ m., $r_o = 0.36449$ m., $t_{\text{blade}} = 6 \cdot 10^{-3}$ m., and $N_{\text{blade}} = 72$, it is found that the modulus of elasticity of the axisymmetric model in terms of the real one is $E_{\text{eff}} = 0.201 E_{\text{blade}}$.

- Correction factor for LPT stator blades

Substituting the values $r_i = 0.305402$ m., $r_o = 0.36725$ m., $t_{\text{blade}} = 6 \cdot 10^{-3}$ m., and $N_{\text{blade}} = 77$, we can express the modulus of elasticity of the axisymmetric model in terms of the real one as $E_{\text{eff}} = 0.218 E_{\text{blade}}$.

- Correction factor for LPT rotor blades

Substituting the values $r_i = 0.288065$ m., $r_o = 0.37912$ m., $t_{\text{blade}} = 6 \cdot 10^{-3}$ m., and $N_b = 90$, the modulus of elasticity of the axisymmetric model in terms of the real one is calculated as $E_{\text{eff}} = 0.258 E_{\text{blade}}$.

In addition when a plate-like component is modeled as an axisymmetric element, stress distribution in the component is not realistic. That is, extra hoop stresses are created and radial and axial stresses are in error. If the component is heated up, it can not expand in hoop direction in an axisymmetric model and compressive hoop stresses are created so that the axial and radial stresses are calculated to be larger than the real case. The reverse is true if the component is cooled down. In order to account for this effect, the materials of these blades are modeled as transversely isotropic materials, and hence the stress state of the components approaches to a plane stress case. The material properties of a transversely isotropic material used in modeling the blades are taken as follows:

$$E_{11} = E_{22} = E_{\text{eff}}, \quad E_{33} = 0.01E_{\text{eff}}, \quad \nu_{12} = \nu, \quad \nu_{13} = \nu_{23} = 0.01 \nu,$$

$$\text{and } G_{12} = G_{13} = G_{23} = G_{\text{eff}} = \frac{E_{\text{eff}}}{2(1+\nu)} \quad (\text{B.3})$$

where ν is the actual Poisson's ratio for the blade material and 3 is the hoop direction.

APPENDIX C

CALCULATION OF SPRING STIFFNESSES AT THE MODEL INTERFACE

In the study, a limited number of engine stages are modeled to keep the model simple. In the following descriptions, the engine orientation is such that, the engine inlet is at the left end while the exhaust is at the right. The right side of the second stage LPT nozzle support (which is not modeled) is fixed to the engine casing with bolts (point 5 in Fig. C.1), and therefore, axial and radial displacements are expected to be very small there. The right side of the first stage LPT nozzle support is connected to the left side of the second stage LPT nozzle support with bolts (point 1) and, therefore, axial displacements of the right of the first stage nozzle support are constrained. Linear elastic springs in the axial direction are used there as boundary conditions to simulate the effect of the second stage LPT nozzle stator. The displacements in radial direction are restricted too but the temperature values at the components and also thermal expansion coefficients of these materials are close to each other, therefore we did not place radial springs there. The stiffness values for the axial springs are estimated as follows. The first stage LPT nozzle and the second stage LPT nozzle are more or less similar components. Therefore the ratio of the stress value obtained at the intersection of the impingement cover and pin (point 4) by fixing the right side of the first stage nozzle support (point 1) and the stress value at the same location obtained by fixing the left side of first stage nozzle support should be close to the ratio of the stress value obtained at the very left of the right side of the first stage nozzle support (point 2) by fixing the right

side of the second stage nozzle support (point 3) and the stress value at the same location obtained by fixing the right side of the first stage nozzle support (point 1). In mathematical form, we have the equation below.

$$\frac{\sigma_{4-1}}{\sigma_{4-3}} = \frac{\sigma_{2-5}}{\sigma_{2-1}} \quad (C.1)$$

where

σ_{4-1} is the stress value at the intersection of the impingement cover and pin (point 4) obtained by fixing the right side of the first stage nozzle support (point 1)

σ_{4-3} is the stress value at the same location (point 4) by fixing the left side of the first stage nozzle support (point 3)

σ_{2-5} is the stress value at the the right side of the first stage nozzle support (point 2) by fixing the right side of second stage nozzle support (point 5)

σ_{2-1} is the stress value at the same location (point 2) by fixing the right side of first stage nozzle support (point 1).

Since we have a multiaxial problem, von Mises stress is used as the stress value to compare the locations mentioned.

In equation (C.1) only the term σ_{2-5} is unknown, since all other values can be calculated by imposing the fixed displacement boundary conditions to the proper places. After calculating this value the stiffness of the axial springs placed at location 1 can be determined by varying the stiffness values so that the calculated σ_{2-5} value is obtained at the fixed end of the springs.

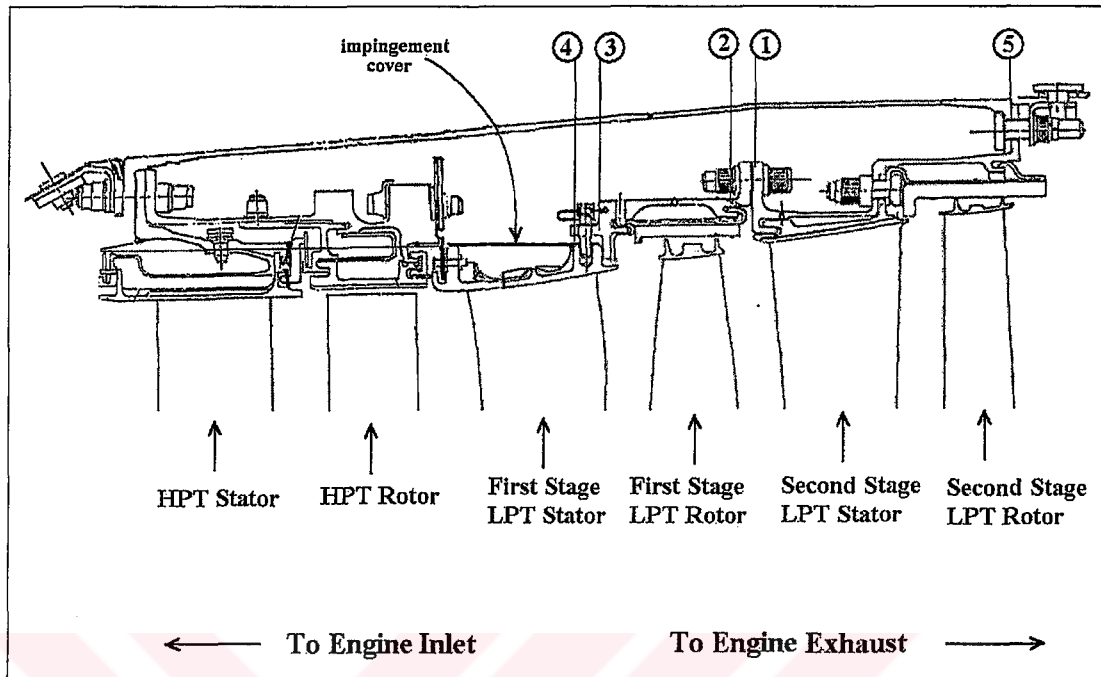


Figure C.1 First Stage and Second Stage LPT Nozzle Support

By imposing the proper boundary conditions explained, the terms obtained in the analysis are calculated as: $\sigma_{4-1} = 990$ MPa, $\sigma_{4-3} = 2.253$ GPa, and $\sigma_{2-1} = 2.039$ GPa. Then, from equation. C.1 σ_{2-5} is calculated as $\sigma_{2-5} = 1.05$ GPa. The stiffness values used and the stress values obtained at location 5 are given below.

k (N/m)	σ (GPa)
Stiffness of the springs	Stress calculated at location 5
$5 \cdot 10^7$	0.952
$1 \cdot 10^8$	0.987
$2.5 \cdot 10^8$	1.096
$5 \cdot 10^8$	1.133
$1 \cdot 10^9$	1.188

From these calculations, the value of the stiffness of the springs used there is decided to be taken as $2.5 \cdot 10^8$ N/m, since it gives the closest result to 1.05 GPa.

Apart from the springs used at the right of the first stage LPT nozzle support, we also used axial linear elastic springs at the left side of the outer band of LPT stator. The left side of the outer band of the LPT stator has a contact with HPT stator, but the interaction of these two parts are not so rigid, there is only a weak connection between these two. Therefore, we used axial springs of stiffness $1 \cdot 10^8$ N/m.

Thirdly, the impingement cover and the pin itself were modeled as contact bodies. However, after a stress analysis, it was seen that the impingement cover and the pin had lost their contact which is not expected to be the case, because the pins are cooled in liquid nitrogen to have a tight fit before they are placed in holes drilled on the impingement cover. But what is important is, in an axisymmetric model the impingement cover appears in two different pieces, one on each side of the pin (and the pin appears like a ring). This error in modeling leads to a separation of the impingement cover and the pin also. In order to overcome this problem we linked the impingement cover and the pin with springs and also the two pieces of the impingement cover on the two sides of a hole with axial and radial springs of the same stiffness. While calculating the values of the stiffness of these springs, we approach the problem as follows. The impingement cover is nominally an axisymmetric component with discontinuities in the axial and circumferential directions at the pin holes only. If a portion of the impingement cover is laid out flat, a figure like Figure C.2 is obtained.

If the impingement cover is then treated like a plate, the stiffness of these springs can be calculated from the equation given below.

$$k = \frac{AE}{D_{pin}(1-\nu^2)} = \frac{(a - D_{pin})tE}{D_{pin}(1-\nu^2)} \quad (C.2)$$

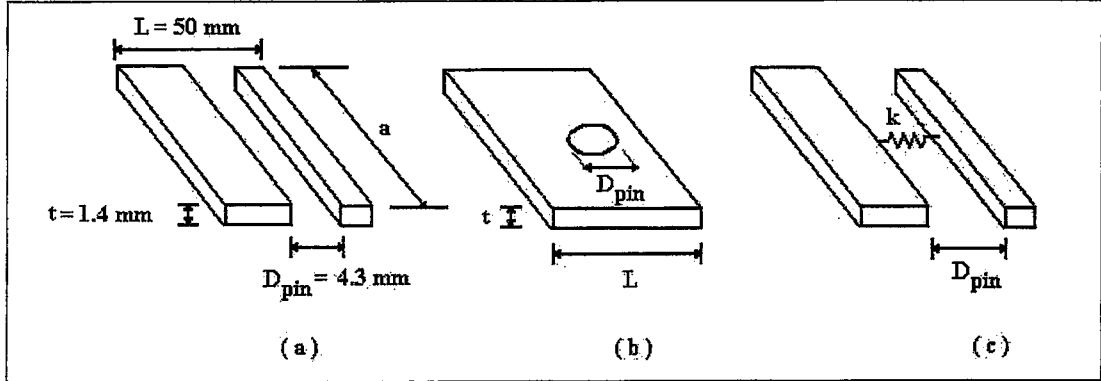


Figure C.2 Impingement Cover Laid Out Flat

a) Impingement Cover as Effectively Appears in an Axisymmetric Model with No Spring b) Real Impingement Cover c) Effective Spring to Correct the Situation in (a)

where t is the thickness of the impingement cover

E is the modulus of elasticity of the impingement cover

D_{pin} is the diameter of the pin

$$a = \left(\frac{2\pi}{N_{pin}} \right) r_{imp} \quad (C.3)$$

N_{pin} is the number of pins in 360°

r_{imp} is the radial distance to the impingement cover from the engine axis.

The variables in equations (C.2) and (C.3) have the values given below.

$$t = 0.0014 \text{ m}, E = 170 \text{ GPa}, D_{pin} = 0.0043 \text{ m}, N_{pin} = 25, \text{ and } r_{imp} = 0.38 \text{ m}$$

Then, using equations (C.2) and (C.3) the stiffness of the springs are calculated as

$$k = 5.809 \cdot 10^9 \text{ N/m}, \text{ and this value is used in the model.}$$

APPENDIX D

CREEP CRACK GROWTH DATA CALCULATIONS

For creep damage calculations, hold periods of the maximum principal stress profile of the critical location were determined, and creep life calculations were performed for these hold periods. Hold periods are time periods in which stress values are constant (Figure D.1). Since creep is defined as the time-dependent inelastic deformation of materials under constant stresses, creep is effective during hold periods only according to the linear damage summation method used in the thesis [6].

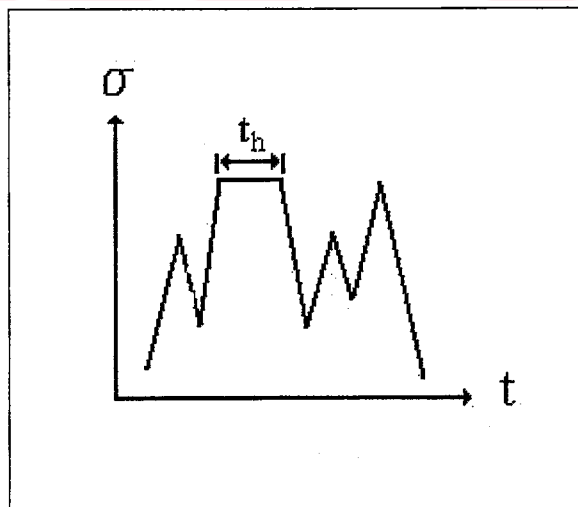


Figure D.1 Hold Time (t_h) in an Arbitrary Stress Profile

When the maximum principal stress history is considered, it is seen that there are 6 hold periods. The values of maximum principal stresses and corresponding temperatures along these hold periods are given on Table 4.2. The data obtained from literature [49] for Inconel 718 is suitable for temperatures of 537 °C (810 K), 593 °C (866 K), and 649 °C (922 K) (Figure D.2). For the hold periods of the maximum principal stress history, temperature values were 581 K, 601 K, 638 K, 600 K, 437 K and 430 K, respectively (See Fig. D.3). Therefore, creep crack growth rate at these temperature values was calculated by linear extrapolation of the data obtained from literature. First, creep crack growth rate (CCGR) data were fit to third order polynomials for each of the temperatures 810 K and 866 K, respectively. Then, CCGRs were calculated for 810 K and 866 K using these polynomials and varying SIF values from 35 MPa√m to 76 MPa√m. The minimum of these SIFs is 35 MPa√m, because the threshold (K_{th}), the SIF value below which no crack growth is observed, was around 35 MPa√m. The maximum of these SIFs was 76 MPa√m, which is the plane strain fracture toughness (K_{IC}) of the pin material, Inconel 718. Then, using logarithm values of CCGR and temperature, linear extrapolation was performed to calculate CCGR for the desired temperatures (hold time temperature values). CCGR curves used in extrapolation (for the temperatures of 810 K and 866 K) and the curves calculated by extrapolation (for the temperatures of 430 K, 437 K, 581 K, 600 K and 638 K) are shown in Fig. D.4. Data are fit with the following polynomials.

$$\dot{a} = -1.712 \cdot 10^{-10} K^2 + 3.957 \cdot 10^{-8} K - 1.056 \cdot 10^{-6} \quad (\text{for } T = 866 \text{ K})$$

$$\dot{a} = -1.192 \cdot 10^{-11} K^2 + 2.331 \cdot 10^{-9} K - 4.625 \cdot 10^{-8} \quad (\text{for } T = 810 \text{ K})$$

$$\dot{a} = -1.788 \cdot 10^{-14} K^2 + 4.134 \cdot 10^{-12} K - 1.104 \cdot 10^{-10} \quad (\text{for } T = 638 \text{ K})$$

$$\dot{a} = -2.834 \cdot 10^{-15} K^2 + 6.55 \cdot 10^{-13} K + 1.749 \cdot 10^{-11} \quad (\text{for } T = 600 \text{ K})$$

$$\dot{a} = -1.079 \cdot 10^{-15} K^2 + 2.495 \cdot 10^{-13} K - 6.661 \cdot 10^{-12} \quad (\text{for } T = 581 \text{ K})$$

$$\dot{a} = -2.1 \cdot 10^{-19} K^2 + 4.885 \cdot 10^{-17} K + 1.296 \cdot 10^{-15} \quad (\text{for } T = 437 \text{ K})$$

$$\dot{a} = -1.294 \cdot 10^{-19} K^2 + 2.991 \cdot 10^{-17} K - 7.985 \cdot 10^{-16} \quad (\text{for } T = 430 \text{ K})$$

where \dot{a} is the CCGR in m/s and K is the SIF in $\text{MPa}\sqrt{\text{m}}$.

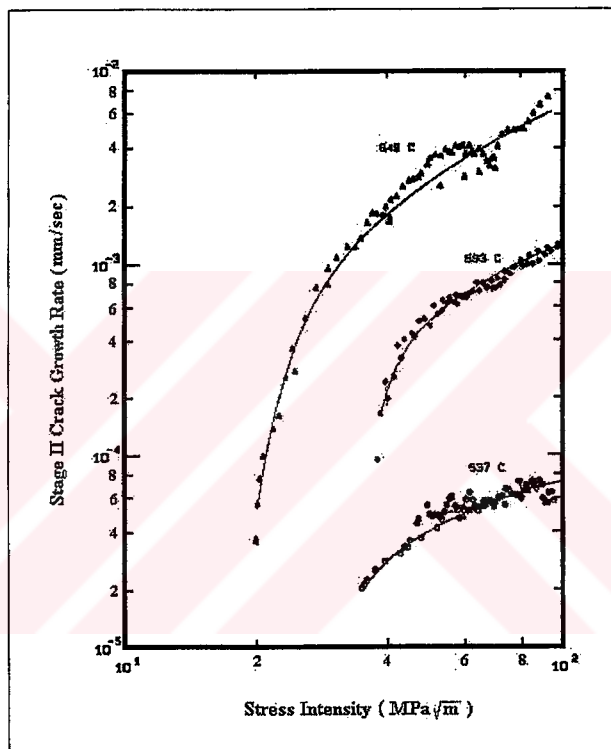


Figure D.2 Creep Crack Growth Curves for Inconel 718 at 800 K, 866 K, and 922 K, [49]

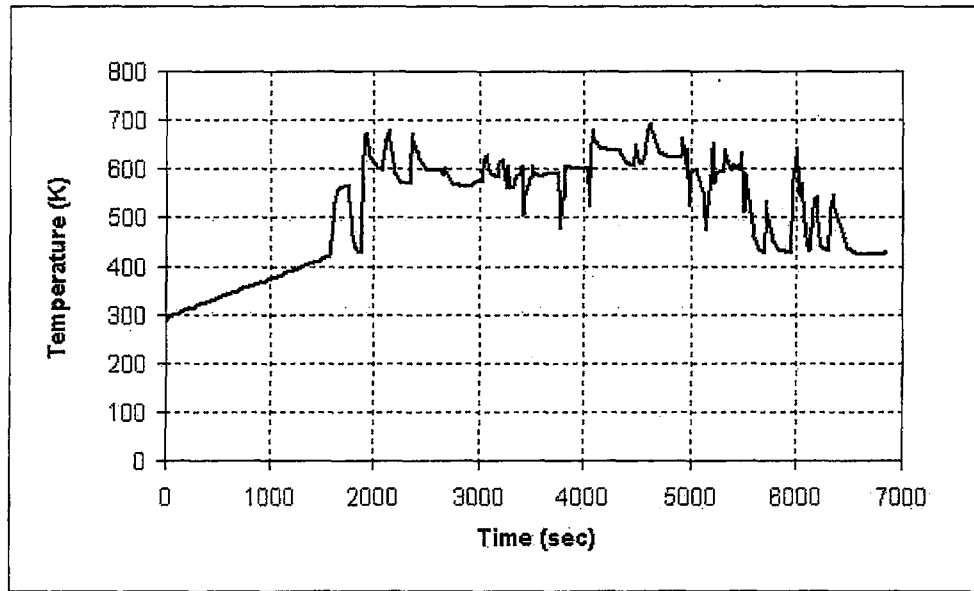


Figure D.3 Temperature History of the Critical Location

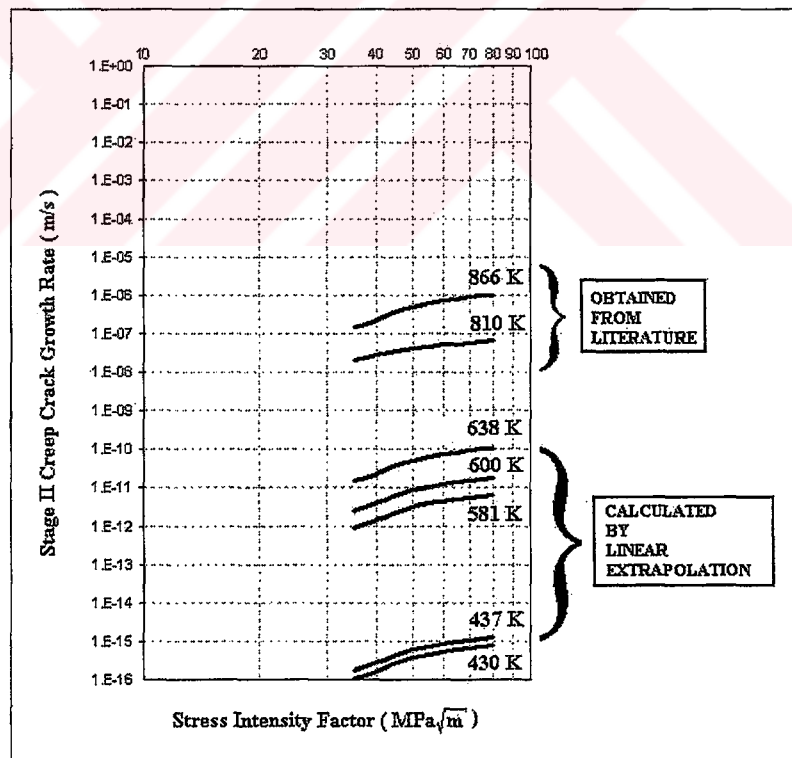


Figure D.4 Creep Crack Growth Curves Obtained by Linear Extrapolation

APPENDIX E

TEMPERATURE AND PRESSURE VALUES OF GAS STREAM, COOLING AIR, AND CRITICAL LOCATION

In thermal analysis, the velocities and the densities of gas stream and cooling air were used. These quantities were calculated by assuming uniform distribution of velocities on the cross-section through which gas flows and using continuity equation, and also assuming isentropic expansion of gases and using isentropic relations. The use of these equations requires the values of total and static pressures, temperatures and mass flow rates of the gases throughout the mission. Temperature and total pressure profiles (and also the numerical values) of gas stream entering first stage low pressure turbine (LPT) stator vanes (T_1 and P_{t1}), leaving LPT stator vanes (T_2 and P_{t2}), and cooling air impinging on LPT outer band (T_3 and P_{t3}) are given on Figures E.1-6 and Tables A.1-6. Then, stress analysis was performed and the critical location was determined based on the maximum principal stress. Temperature and maximum principal stress profiles at the critical location (T_{cr} and P_{cr}) are given on Figure D.3, Figure 4.4 and Tables A.7-8.

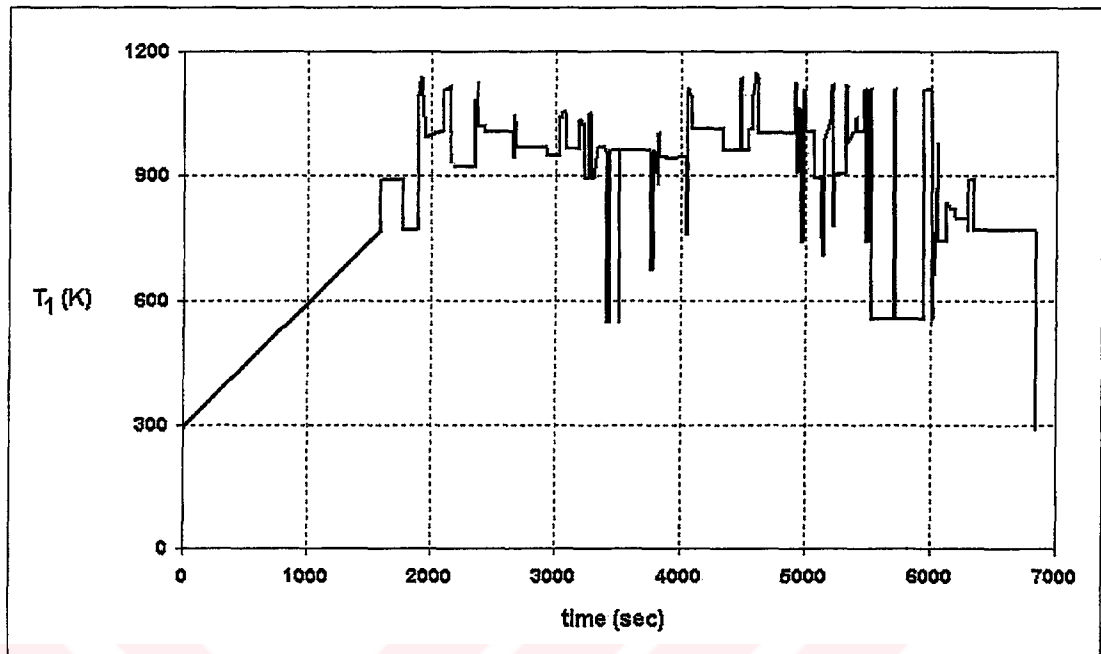


Figure E.1 Temperature Profile of Gas Stream Entering LPT Stator Vanes

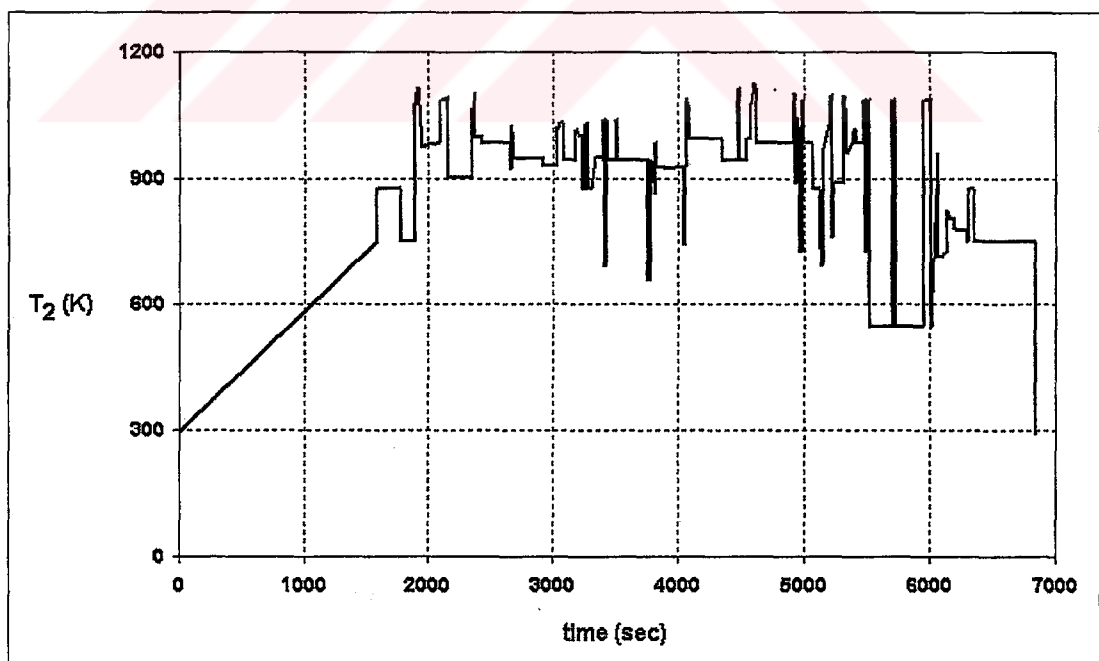


Figure E.2 Temperature Profile of Gas Stream Leaving LPT Stator Vanes

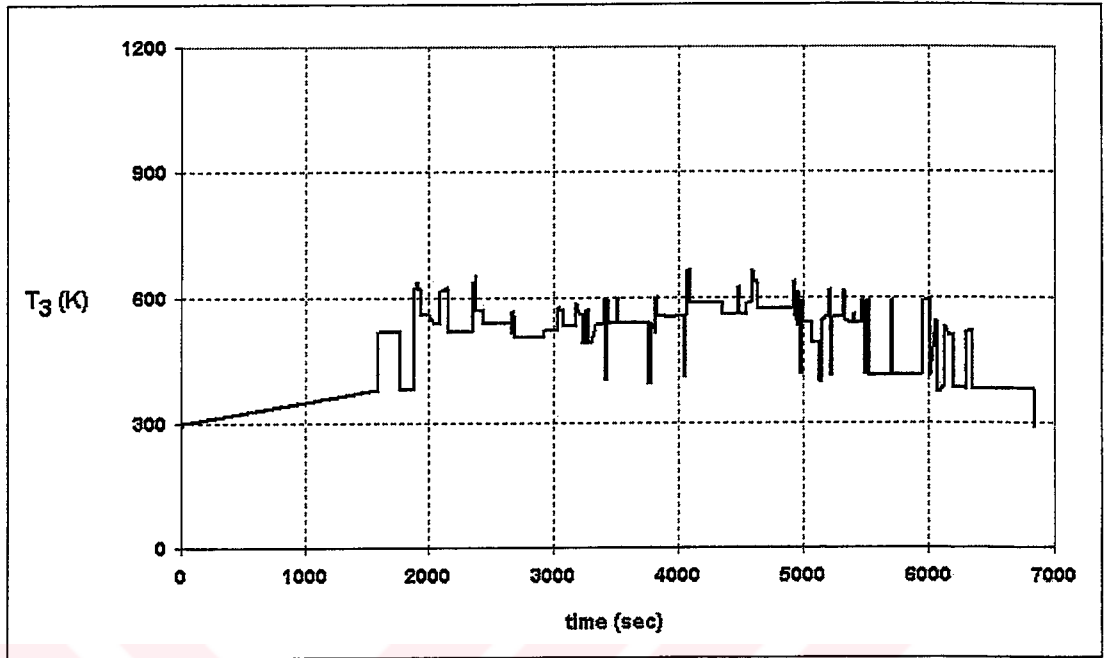


Figure E.3 Temperature Profile of Cooling Air Impinging on LPT Outer Band

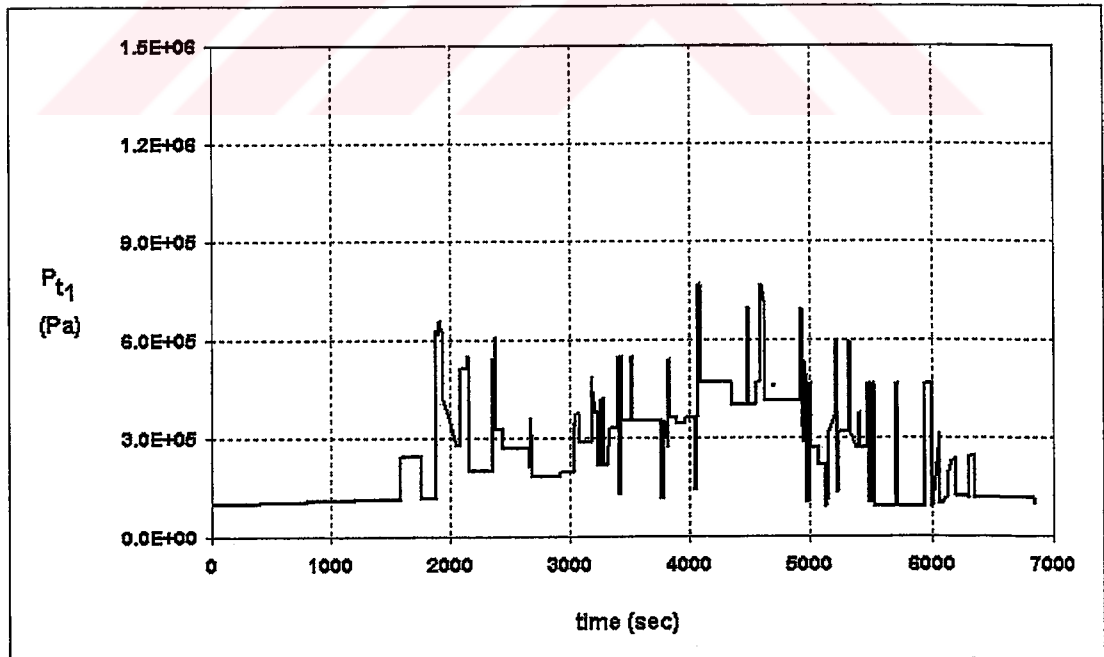


Figure E.4 Total Pressure Profile of Gas Stream Entering LPT Stator Vanes

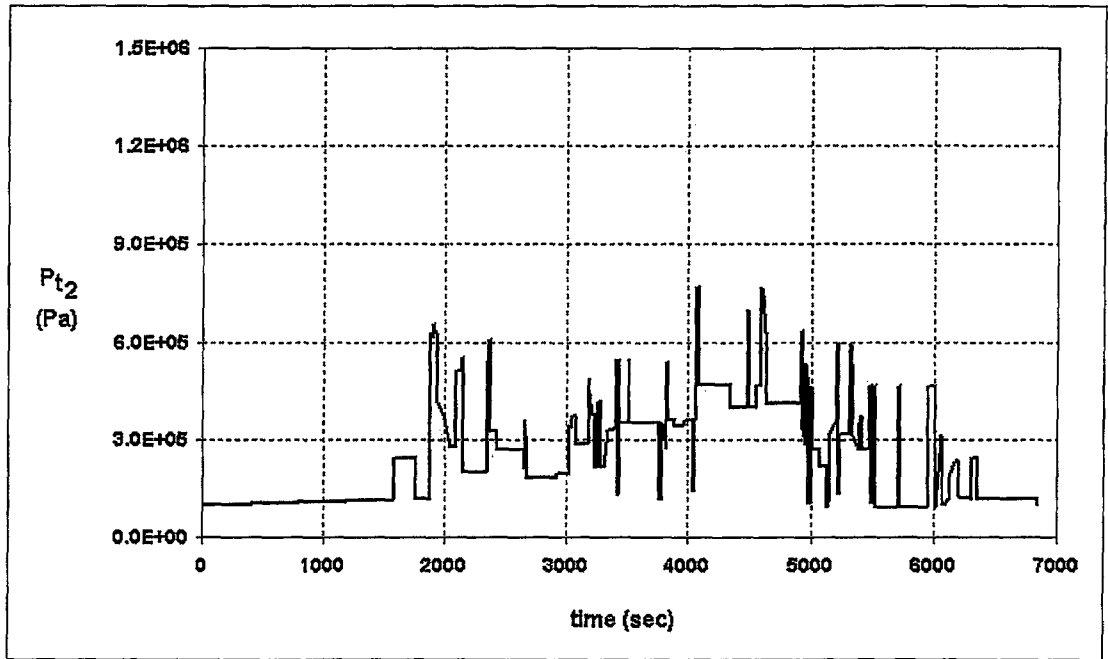


Figure E.5 Total Pressure Profile of Gas Stream Leaving LPT Stator Vanes

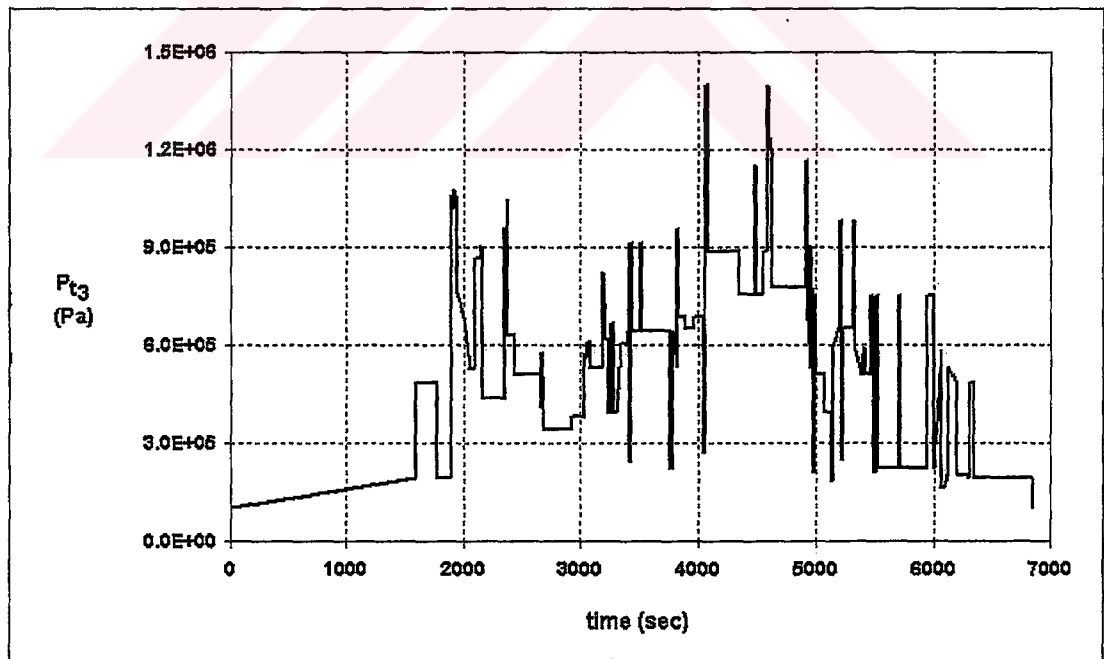


Figure E.6 Total Pressure Profile of Cooling Air Impinging on LPT Outer Band

**Table E.1 Numerical Values of the Temperature Profile of Gas Stream Entering
LPT Stator Vanes**

Time(sec)	T1(K)	Time(sec)	T1(K)	Time(sec)	T1(K)	Time(sec)	T1(K)
0	290.0	3048	1041.0	4044	944.2	5316	1117.4
12	300.0	3051	1054.9	4047	759.2	5328	1090.3
1587	768.0	3063	1054.9	4056	759.2	5331	980.3
1590	891.0	3078	1054.9	4059	944.2	5376	1006.0
1770	891.0	3084	964.5	4065	1110.7	5394	1006.0
1773	768.0	3099	964.5	4068	1094.0	5397	1031.7
1887	768.0	3102	964.5	4086	1094.0	5400	1031.7
1890	1095.9	3114	964.5	4092	1014.3	5403	1040.9
1902	1095.9	3183	964.5	4347	1014.3	5409	1040.9
1905	1126.6	3186	1034.3	4350	963.0	5412	1006.0
1911	1126.6	3195	1035.2	4476	963.0	5466	1006.0
1914	1138.0	3216	1022.6	4479	1135.8	5469	1107.8
1917	1138.0	3234	1022.6	4488	1135.8	5481	1107.8
1926	1122.8	3237	895.0	4491	963.0	5484	739.6
1932	1095.9	3261	895.0	4548	963.0	5505	739.6
1947	993.9	3264	1050.6	4551	1014.3	5508	1107.8
1998	999.3	3282	1050.6	4584	1014.3	5520	1107.8
2049	1005.9	3288	895.0	4587	1094.0	5523	553.7
2091	1005.9	3306	895.0	4602	1148.1	5703	553.7
2094	1106.5	3339	968.7	4629	1126.5	5706	1107.8
2100	1106.5	3354	968.7	4632	1004.0	5715	1107.8
2139	1106.5	3378	968.7	4917	1004.0	5718	553.7
2142	1116.7	3393	968.7	4920	1126.5	5943	553.7
2151	1116.7	3408	963.5	4929	1126.5	5949	1107.8
2154	922.8	3411	544.4	4932	906.0	6006	1107.8
2346	922.8	3417	548.4	4950	964.5	6009	553.7
2349	933.0	3420	707.3	4953	1065.6	6060	980.3
2352	1085.2	3429	707.3	4968	1024.0	6063	741.2
2367	1085.2	3432	548.4	4974	739.6	6084	741.2
2370	1123.7	3435	548.4	4986	739.6	6114	740.6
2373	1123.7	3438	963.5	4992	1107.8	6123	740.6
2376	1019.9	3510	963.5	5001	1107.8	6129	837.9
2430	1019.9	3516	548.4	5004	1006.0	6161.4	819.0
2433	1006.0	3519	548.4	5067	1006.0	6168	819.0
2652	1006.0	3522	963.5	5070	895.0	6189	823.2
2655	943.7	3759	963.5	5124	895.0	6192	801.2
2661	943.7	3762	672.9	5127	750.7	6198	801.2
2664	1046.4	3783	672.9	5139	708.3	6210	795.7
2667	1046.4	3786	963.5	5145	708.3	6231	795.7
2670	1027.7	3817.8	880.7	5148	989.9	6291	795.7
2679	1027.7	3819	1003.0	5202	1046.2	6297	768.0
2682	967.6	3831	1003.0	5205	1117.4	6300	891.0
2919	967.6	3834	944.2	5217	1117.4	6342	891.0
2922	948.2	3891	944.2	5220	778.0	6345	768.0
3030	948.2	3894	942.4	5226	778.0	6834	768.0
3033	1044.2	3963	942.4	5229	905.3	6840	290.0
3045	1044.2	3966	944.2	5313	905.3		

**Table E.2 Numerical Values of the Temperature Profile of Gas Stream Leaving
LPT Stator Vanes**

Time(sec)	T2(K)	Time(sec)	T2(K)	Time(sec)	T2(K)	Time(sec)	T2(K)
0	290.0	3048	1018.4	4044	925.3	5316	1093.5
12	300.0	3051	1031.3	4047	742.3	5328	1067.3
1587	749.2	3063	1031.3	4056	742.3	5331	959.3
1590	873.1	3078	1031.8	4059	925.3	5376	983.6
1770	873.1	3084	943.6	4065	1086.9	5394	983.6
1773	749.2	3099	943.6	4068	1073.3	5397	1008.9
1887	749.2	3102	943.6	4086	1073.3	5400	1008.9
1890	1073.2	3114	943.6	4092	993.6	5403	1017.9
1902	1073.2	3183	943.6	4347	993.6	5409	1017.9
1905	1103.2	3186	1012.7	4350	943.5	5412	983.6
1911	1103.2	3195	1013.0	4476	943.5	5466	983.6
1914	1114.0	3216	1000.3	4479	1111.4	5469	1083.2
1917	1114.0	3234	1000.3	4488	1111.4	5481	1083.2
1926	1098.9	3237	875.5	4491	943.5	5484	723.9
1932	1073.2	3261	875.5	4548	943.5	5505	723.9
1947	973.2	3264	1027.6	4551	993.6	5508	1083.2
1998	978.1	3282	1027.6	4584	993.6	5520	1083.2
2049	983.6	3288	875.5	4587	1073.3	5523	546.7
2091	983.6	3306	875.5	4602	1123.9	5703	546.7
2094	1083.2	3339	947.8	4629	1103.1	5706	1083.2
2100	1083.2	3354	947.8	4632	983.2	5715	1083.2
2139	1083.2	3378	947.8	4917	983.2	5718	546.7
2142	1093.2	3393	947.8	4920	1103.1	5943	546.7
2151	1093.2	3408	943.1	4929	1103.1	5949	1083.2
2154	903.3	3411	1036.8	4932	889.0	6006	1083.2
2346	903.3	3417	1036.8	4950	943.6	6009	546.7
2349	913.6	3420	692.5	4953	1043.8	6060	959.3
2352	1063.6	3429	692.5	4968	1003.3	6063	713.3
2367	1063.6	3432	1036.8	4974	723.9	6084	713.3
2370	1101.2	3435	1036.8	4986	723.9	6114	723.4
2373	1101.2	3438	943.1	4992	1083.2	6123	723.4
2376	998.2	3510	943.1	5001	1083.2	6129	823.0
2430	998.2	3516	1036.8	5004	983.6	6161.4	803.9
2433	983.6	3519	1036.8	5067	983.6	6168	803.9
2652	983.6	3522	943.1	5070	875.5	6189	807.9
2655	923.1	3759	943.1	5124	875.5	6192	781.1
2661	923.1	3762	659.3	5127	733.8	6198	781.1
2664	1023.6	3783	659.3	5139	693.2	6210	775.8
2667	1023.6	3786	943.1	5145	693.2	6231	775.8
2670	1004.9	3817.8	863.1	5148	968.6	6291	775.8
2679	1004.9	3819	983.6	5202	1023.1	6297	749.2
2682	945.4	3831	983.6	5205	1093.5	6300	873.1
2919	945.4	3834	925.3	5217	1093.5	6342	873.1
2922	927.7	3891	925.3	5220	760.4	6345	749.2
3030	927.7	3894	923.6	5226	760.4	6834	749.2
3033	1021.9	3963	923.6	5229	888.2	6840	290.0
3045	1021.9	3966	925.3	5313	888.2		

Table E.3 Numerical Values of the Temperature Profile of Cooling Air Impinging on LPT Outer Band

Time(sec)	T3(K)	Time(sec)	T3(K)	Time(sec)	T3(K)	Time(sec)	T3(K)
0	290.0	3048	569.9	4044	554.6	5316	617.5
12	300.0	3051	570.0	4047	412.1	5328	610.3
1587	379.4	3063	570.0	4056	412.1	5331	544.8
1590	520.7	3078	570.0	4059	554.6	5376	539.0
1770	520.7	3084	531.3	4065	610.8	5394	539.0
1773	379.4	3099	531.3	4068	662.8	5397	558.2
1887	379.4	3102	531.3	4086	662.8	5400	558.2
1890	622.1	3114	531.3	4092	585.2	5403	560.3
1902	622.1	3183	531.3	4347	585.2	5409	560.3
1905	635.5	3186	585.9	4350	558.2	5412	539.0
1911	635.5	3195	572.9	4476	558.2	5466	539.0
1914	633.6	3216	558.3	4479	625.1	5469	591.9
1917	633.6	3234	558.3	4488	625.1	5481	591.9
1926	621.4	3237	493.4	4491	558.2	5484	417.2
1932	622.1	3261	493.4	4548	558.2	5505	417.2
1947	561.2	3264	569.6	4551	585.2	5508	591.9
1998	558.0	3282	569.6	4584	585.2	5520	591.9
2049	540.4	3288	493.4	4587	662.8	5523	413.1
2091	540.4	3306	493.4	4602	641.2	5703	413.1
2094	617.8	3339	536.5	4629	636.7	5706	591.9
2100	617.8	3354	536.5	4632	571.8	5715	591.9
2139	617.8	3378	536.5	4917	571.8	5718	413.1
2142	624.6	3393	536.5	4920	636.7	5943	413.1
2151	624.6	3408	538.9	4929	636.7	5949	591.9
2154	520.4	3411	597.0	4932	556.4	6006	591.9
2346	520.4	3417	597.0	4950	531.3	6009	413.1
2349	531.7	3420	403.8	4953	611.8	6060	544.8
2352	636.9	3429	403.8	4968	595.8	6063	372.5
2367	636.9	3432	597.0	4974	417.2	6084	372.5
2370	652.8	3435	597.0	4986	417.2	6114	386.3
2373	652.8	3438	538.9	4992	591.9	6123	386.3
2376	570.5	3510	538.9	5001	591.9	6129	532.2
2430	570.5	3516	597.0	5004	539.0	6161.4	509.7
2433	539.0	3519	597.0	5067	539.0	6168	509.7
2652	539.0	3522	538.9	5070	493.4	6189	509.0
2655	517.4	3759	538.9	5124	493.4	6192	383.8
2661	517.4	3762	394.9	5127	401.8	6198	383.8
2664	567.8	3783	394.9	5139	397.6	6210	383.0
2667	567.8	3786	538.9	5145	397.6	6231	383.0
2670	553.0	3817.8	517.1	5148	545.4	6291	383.0
2679	553.0	3819	601.4	5202	561.2	6297	379.4
2682	506.8	3831	601.4	5205	617.5	6300	520.7
2919	506.8	3834	554.6	5217	617.5	6342	520.7
2922	523.2	3891	554.6	5220	415.3	6345	379.4
3030	523.2	3894	552.9	5226	415.3	6834	379.4
3033	577.5	3963	552.9	5229	553.8	6840	290.0
3045	577.5	3966	554.6	5313	553.8		

**Table E.4 Numerical Values of the Total Pressure Profile of Gas Stream Entering
LPT Stator Vanes**

Time(sec)	Pt1(Pa)	Time(sec)	Pt1(Pa)	Time(sec)	Pt1(Pa)	Time(sec)	Pt1(Pa)
0	1.01E+05	3048	3.37E+05	4044	3.60E+05	5316	5.94E+05
12	1.01E+05	3051	3.72E+05	4047	1.44E+05	5328	5.35E+05
1587	1.18E+05	3063	3.72E+05	4056	1.44E+05	5331	3.13E+05
1590	2.41E+05	3078	3.72E+05	4059	3.60E+05	5376	2.69E+05
1770	2.41E+05	3084	2.86E+05	4065	6.02E+05	5394	2.69E+05
1773	1.18E+05	3099	2.86E+05	4068	7.66E+05	5397	3.52E+05
1887	1.18E+05	3102	2.86E+05	4086	7.66E+05	5400	3.52E+05
1890	6.31E+05	3114	2.86E+05	4092	4.69E+05	5403	3.73E+05
1902	6.31E+05	3183	2.86E+05	4347	4.69E+05	5409	3.73E+05
1905	6.15E+05	3186	4.88E+05	4350	3.98E+05	5412	2.69E+05
1911	6.15E+05	3195	4.41E+05	4476	3.98E+05	5466	2.69E+05
1914	6.54E+05	3216	3.77E+05	4479	7.00E+05	5469	4.62E+05
1917	6.54E+05	3234	3.77E+05	4488	7.00E+05	5481	4.62E+05
1926	6.30E+05	3237	2.16E+05	4491	3.98E+05	5484	1.04E+05
1932	6.31E+05	3261	2.16E+05	4548	3.98E+05	5505	1.04E+05
1947	4.14E+05	3264	4.14E+05	4551	4.69E+05	5508	4.62E+05
1998	3.65E+05	3282	4.14E+05	4584	4.69E+05	5520	4.62E+05
2049	2.79E+05	3288	2.16E+05	4587	7.66E+05	5523	9.18E+04
2091	2.79E+05	3306	2.16E+05	4602	7.44E+05	5703	9.18E+04
2094	5.14E+05	3339	3.28E+05	4629	6.94E+05	5706	4.62E+05
2100	5.14E+05	3354	3.28E+05	4632	4.11E+05	5715	4.62E+05
2139	5.14E+05	3378	3.28E+05	4917	4.11E+05	5718	9.18E+04
2142	5.49E+05	3393	3.28E+05	4920	6.94E+05	5943	9.18E+04
2151	5.49E+05	3408	3.53E+05	4929	6.94E+05	5949	4.62E+05
2154	1.99E+05	3411	5.48E+05	4932	3.35E+05	6006	4.62E+05
2346	1.99E+05	3417	5.48E+05	4950	2.86E+05	6009	9.18E+04
2349	2.20E+05	3420	1.29E+05	4953	5.34E+05	6060	3.13E+05
2352	5.41E+05	3429	1.29E+05	4968	4.51E+05	6063	9.94E+04
2367	5.41E+05	3432	5.48E+05	4974	1.04E+05	6084	9.94E+04
2370	6.07E+05	3435	5.48E+05	4986	1.04E+05	6114	1.15E+05
2373	6.07E+05	3438	3.53E+05	4992	4.62E+05	6123	1.15E+05
2376	3.27E+05	3510	3.53E+05	5001	4.62E+05	6129	1.97E+05
2430	3.27E+05	3516	5.48E+05	5004	2.69E+05	6161.4	2.30E+05
2433	2.69E+05	3519	5.48E+05	5067	2.69E+05	6168	2.30E+05
2652	2.69E+05	3522	3.53E+05	5070	2.16E+05	6189	2.37E+05
2655	2.12E+05	3759	3.53E+05	5124	2.16E+05	6192	1.25E+05
2661	2.12E+05	3762	1.16E+05	5127	9.12E+04	6198	1.25E+05
2664	3.58E+05	3783	1.16E+05	5139	1.11E+05	6210	1.23E+05
2667	3.58E+05	3786	3.53E+05	5145	1.11E+05	6231	1.23E+05
2670	3.03E+05	3817.8	2.72E+05	5148	3.17E+05	6291	1.23E+05
2679	3.03E+05	3819	5.38E+05	5202	3.63E+05	6297	1.18E+05
2682	1.80E+05	3831	5.38E+05	5205	5.94E+05	6300	2.41E+05
2919	1.80E+05	3834	3.60E+05	5217	5.94E+05	6342	2.41E+05
2922	1.96E+05	3891	3.60E+05	5220	1.34E+05	6345	1.18E+05
3030	1.96E+05	3894	3.43E+05	5226	1.34E+05	6834	1.18E+05
3033	3.41E+05	3963	3.43E+05	5229	3.16E+05	6840	1.01E+05
3045	3.41E+05	3966	3.60E+05	5313	3.16E+05		

**Table E.5 Numerical Values of the Total Pressure Profile of Gas Stream Leaving
LPT Stator Vanes**

Time(sec)	Pt2(Pa)	Time(sec)	Pt2(Pa)	Time(sec)	Pt2(Pa)	Time(sec)	Pt2(Pa)
0	1.01E+05	3048	3.37E+05	4044	3.60E+05	5316	5.94E+05
12	1.01E+05	3051	3.72E+05	4047	1.44E+05	5328	5.35E+05
1587	1.18E+05	3063	3.72E+05	4056	1.44E+05	5331	3.13E+05
1590	2.41E+05	3078	3.72E+05	4059	3.60E+05	5376	2.69E+05
1770	2.41E+05	3084	2.86E+05	4065	6.02E+05	5394	2.69E+05
1773	1.18E+05	3099	2.86E+05	4068	7.66E+05	5397	3.52E+05
1887	1.18E+05	3102	2.86E+05	4086	7.66E+05	5400	3.52E+05
1890	6.31E+05	3114	2.86E+05	4092	4.69E+05	5403	3.73E+05
1902	6.31E+05	3183	2.86E+05	4347	4.69E+05	5409	3.73E+05
1905	6.15E+05	3186	4.88E+05	4350	3.98E+05	5412	2.69E+05
1911	6.15E+05	3195	4.41E+05	4476	3.98E+05	5466	2.69E+05
1914	6.54E+05	3216	3.77E+05	4479	7.00E+05	5469	4.62E+05
1917	6.54E+05	3234	3.77E+05	4488	7.00E+05	5481	4.62E+05
1926	6.30E+05	3237	2.16E+05	4491	3.98E+05	5484	1.04E+05
1932	6.31E+05	3261	2.16E+05	4548	3.98E+05	5505	1.04E+05
1947	4.14E+05	3264	4.14E+05	4551	4.69E+05	5508	4.62E+05
1998	3.65E+05	3282	4.14E+05	4584	4.69E+05	5520	4.62E+05
2049	2.79E+05	3288	2.16E+05	4587	7.66E+05	5523	9.18E+04
2091	2.79E+05	3306	2.16E+05	4602	7.44E+05	5703	9.18E+04
2094	5.14E+05	3339	3.28E+05	4629	6.34E+05	5706	4.62E+05
2100	5.14E+05	3354	3.28E+05	4632	4.11E+05	5715	4.62E+05
2139	5.14E+05	3378	3.28E+05	4917	4.11E+05	5718	9.18E+04
2142	5.49E+05	3393	3.28E+05	4920	6.34E+05	5943	9.18E+04
2151	5.49E+05	3408	3.53E+05	4929	6.34E+05	5949	4.62E+05
2154	1.99E+05	3411	5.48E+05	4932	3.35E+05	6006	4.62E+05
2346	1.99E+05	3417	5.48E+05	4950	2.86E+05	6009	9.18E+04
2349	2.20E+05	3420	1.29E+05	4953	5.34E+05	6060	3.13E+05
2352	5.41E+05	3429	1.29E+05	4968	4.51E+05	6063	9.94E+04
2367	5.41E+05	3432	5.48E+05	4974	1.04E+05	6084	9.94E+04
2370	6.07E+05	3435	5.48E+05	4986	1.04E+05	6114	1.15E+05
2373	6.07E+05	3438	3.53E+05	4992	4.62E+05	6123	1.15E+05
2376	3.27E+05	3510	3.53E+05	5001	4.62E+05	6129	1.97E+05
2430	3.27E+05	3516	5.48E+05	5004	2.69E+05	6161.4	2.30E+05
2433	2.69E+05	3519	5.48E+05	5067	2.69E+05	6168	2.30E+05
2652	2.69E+05	3522	3.53E+05	5070	2.16E+05	6189	2.37E+05
2655	2.12E+05	3759	3.53E+05	5124	2.16E+05	6192	1.25E+05
2661	2.12E+05	3762	1.16E+05	5127	9.12E+04	6198	1.25E+05
2664	3.58E+05	3783	1.16E+05	5139	1.11E+05	6210	1.23E+05
2667	3.58E+05	3786	3.53E+05	5145	1.11E+05	6231	1.23E+05
2670	3.03E+05	3817.8	2.72E+05	5148	3.17E+05	6291	1.23E+05
2679	3.03E+05	3819	5.38E+05	5202	3.63E+05	6297	1.18E+05
2682	1.80E+05	3831	5.38E+05	5205	5.94E+05	6300	2.41E+05
2919	1.80E+05	3834	3.60E+05	5217	5.94E+05	6342	2.41E+05
2922	1.96E+05	3891	3.60E+05	5220	1.34E+05	6345	1.18E+05
3030	1.96E+05	3894	3.43E+05	5226	1.34E+05	6834	1.18E+05
3033	3.41E+05	3963	3.43E+05	5229	3.16E+05	6840	1.01E+05
3045	3.41E+05	3966	3.60E+05	5313	3.16E+05		

**Table E.6 Numerical Values of the Total Pressure Profile of Cooling Impinging to
LPT Outer Band**

Time(sec)	Pt3(Pa)	Time(sec)	Pt3(Pa)	Time(sec)	Pt3(Pa)	Time(sec)	Pt3(Pa)
0	1.01E+05	3048	5.63E+05	4044	6.88E+05	5316	9.82E+05
12	1.01E+05	3051	6.09E+05	4047	2.69E+05	5328	8.98E+05
1587	1.92E+05	3063	6.09E+05	4056	2.69E+05	5331	5.84E+05
1590	4.85E+05	3078	6.09E+05	4059	6.88E+05	5376	5.08E+05
1770	4.85E+05	3084	5.33E+05	4065	1.04E+06	5394	5.08E+05
1773	1.92E+05	3099	5.33E+05	4068	1.40E+06	5397	5.71E+05
1887	1.92E+05	3102	5.33E+05	4086	1.40E+06	5400	5.71E+05
1890	1.06E+06	3114	5.33E+05	4092	8.88E+05	5403	5.93E+05
1902	1.06E+06	3183	5.33E+05	4347	8.88E+05	5409	5.93E+05
1905	1.02E+06	3186	8.24E+05	4350	7.55E+05	5412	5.08E+05
1911	1.02E+06	3195	7.29E+05	4476	7.55E+05	5466	5.08E+05
1914	1.08E+06	3216	6.18E+05	4479	1.15E+06	5469	7.49E+05
1917	1.08E+06	3234	6.18E+05	4488	1.15E+06	5481	7.49E+05
1926	1.04E+06	3237	3.93E+05	4491	7.55E+05	5484	2.12E+05
1932	1.06E+06	3261	3.93E+05	4548	7.55E+05	5505	2.12E+05
1947	7.61E+05	3264	6.65E+05	4551	8.88E+05	5508	7.49E+05
1998	6.86E+05	3282	6.65E+05	4584	8.88E+05	5520	7.49E+05
2049	5.29E+05	3288	3.93E+05	4587	1.40E+06	5523	2.24E+05
2091	5.29E+05	3306	3.93E+05	4602	1.24E+06	5703	2.24E+05
2094	8.64E+05	3339	6.05E+05	4629	1.17E+06	5706	7.49E+05
2100	8.64E+05	3354	6.05E+05	4632	7.77E+05	5715	7.49E+05
2139	8.64E+05	3378	6.05E+05	4917	7.77E+05	5718	2.24E+05
2142	9.05E+05	3393	6.05E+05	4920	1.17E+06	5943	2.24E+05
2151	9.05E+05	3408	6.42E+05	4929	1.17E+06	5949	7.49E+05
2154	4.36E+05	3411	9.14E+05	4932	6.78E+05	6006	7.49E+05
2346	4.36E+05	3417	9.14E+05	4950	5.33E+05	6009	2.24E+05
2349	4.76E+05	3420	2.43E+05	4953	9.03E+05	6060	5.84E+05
2352	9.58E+05	3429	2.43E+05	4968	7.74E+05	6063	1.65E+05
2367	9.58E+05	3432	9.14E+05	4974	2.12E+05	6084	1.65E+05
2370	1.05E+06	3435	9.14E+05	4986	2.12E+05	6114	2.00E+05
2373	1.05E+06	3438	6.42E+05	4992	7.49E+05	6123	2.00E+05
2376	6.30E+05	3510	6.42E+05	5001	7.49E+05	6129	5.33E+05
2430	6.30E+05	3516	9.14E+05	5004	5.08E+05	6161.4	5.08E+05
2433	5.08E+05	3519	9.14E+05	5067	5.08E+05	6168	5.08E+05
2652	5.08E+05	3522	6.42E+05	5070	3.93E+05	6189	4.91E+05
2655	4.10E+05	3759	6.42E+05	5124	3.93E+05	6192	2.07E+05
2661	4.10E+05	3762	2.24E+05	5127	1.82E+05	6198	2.07E+05
2664	5.75E+05	3783	2.24E+05	5139	2.07E+05	6210	2.03E+05
2667	5.75E+05	3786	6.42E+05	5145	2.07E+05	6231	2.03E+05
2670	4.97E+05	3817.8	5.38E+05	5148	5.94E+05	6291	2.03E+05
2679	4.97E+05	3819	9.54E+05	5202	6.69E+05	6297	1.92E+05
2682	3.42E+05	3831	9.54E+05	5205	9.82E+05	6300	4.85E+05
2919	3.42E+05	3834	6.88E+05	5217	9.82E+05	6342	4.85E+05
2922	3.81E+05	3891	6.88E+05	5220	2.47E+05	6345	1.92E+05
3030	3.81E+05	3894	6.51E+05	5226	2.47E+05	6834	1.92E+05
3033	5.75E+05	3963	6.51E+05	5229	6.49E+05	6840	1.01E+05
3045	5.75E+05	3966	6.88E+05	5313	6.49E+05		

Table E.7 Numerical Values of the Temperature Profile of the Critical Location

Time(sec)	Tcr(K)	Time(sec)	Tcr(K)	Time(sec)	Tcr(K)	Time(sec)	Tcr(K)
0	290.0	3048	614.2	4044	602.1	5328	639.2
12	291.2	3051	617.0	4047	570.1	5331	629.4
1587	422.2	3063	624.4	4056	525.5	5376	602.1
1590	453.0	3078	628.5	4059	545.1	5394	598.9
1770	565.4	3084	615.4	4065	581.4	5397	603.0
1773	534.6	3099	598.9	4068	607.8	5400	605.5
1887	426.8	3102	596.3	4086	679.4	5403	608.0
1890	469.0	3114	590.1	4092	663.4	5409	611.8
1902	572.9	3183	585.2	4347	638.4	5412	608.5
1905	595.4	3186	597.7	4350	631.8	5466	598.6
1911	627.9	3195	611.4	4476	608.5	5469	610.5
1914	641.4	3216	616.3	4479	623.9	5481	633.1
1917	652.7	3234	616.6	4488	649.1	5484	597.6
1926	669.4	3237	601.7	4491	640.1	5505	510.9
1932	674.9	3261	561.6	4548	610.9	5508	539.8
1947	646.8	3264	575.2	4551	616.5	5520	592.2
1998	615.3	3282	607.1	4584	633.0	5523	561.9
2049	601.3	3288	587.1	4587	652.6	5703	429.8
2091	599.0	3306	561.7	4602	681.9	5706	469.0
2094	616.9	3339	577.9	4629	695.1	5715	534.5
2100	635.9	3354	584.6	4632	679.9	5718	511.7
2139	671.9	3378	588.5	4917	625.2	5943	429.1
2142	675.3	3393	589.3	4920	640.5	5949	489.8
2151	680.5	3408	590.8	4929	663.5	6006	644.3
2154	656.9	3411	603.5	4932	650.1	6009	606.3
2346	570.0	3417	608.3	4950	610.0	6060	569.6
2349	572.3	3420	563.9	4953	623.6	6063	535.6
2352	598.2	3429	504.9	4968	639.9	6084	461.8
2367	652.5	3432	533.7	4974	580.0	6114	435.1
2370	664.3	3435	549.3	4986	523.7	6123	431.5
2373	673.5	3438	544.8	4992	563.6	6129	477.8
2376	660.8	3510	586.4	5001	598.0	6161.4	533.2
2430	629.2	3516	603.2	5004	595.4	6168	537.6
2433	621.1	3519	606.2	5067	597.6	6189	543.3
2652	597.4	3522	592.7	5070	587.4	6192	516.6
2655	592.4	3759	590.7	5124	547.0	6198	490.8
2661	586.8	3762	559.0	5127	526.4	6210	462.3
2664	595.9	3783	478.3	5139	486.8	6231	442.7
2667	601.0	3786	501.1	5145	473.1	6291	432.6
2670	601.4	3817.8	549.0	5148	498.8	6297	431.0
2679	605.7	3819	560.4	5202	607.0	6300	460.8
2682	596.5	3831	607.2	5205	623.2	6342	547.9
2919	565.1	3834	604.0	5217	653.2	6345	520.4
2922	568.5	3891	602.4	5220	611.7	6834	424.4
3030	575.9	3894	602.0	5226	572.6	6840	433.1
3033	588.3	3963	600.6	5229	586.1		
3045	611.5	3966	601.0	5313	595.9		

**Table E.8 Numerical Values of the Maximum Principal Stress Profile of the
Critical Location**

Time(sec)	Pcr(Pa)	Time(sec)	Pcr(Pa)	Time(sec)	Pcr(Pa)	Time(sec)	Pcr(Pa)
0	0.00E+00	3048	9.05E+08	4044	8.23E+08	5328	8.14E+08
12	1.50E+05	3051	9.11E+08	4047	9.39E+08	5331	8.72E+08
1587	7.90E+08	3063	9.37E+08	4056	9.47E+08	5376	9.47E+08
1590	6.93E+08	3078	9.60E+08	4059	8.28E+08	5394	9.65E+08
1770	7.58E+08	3084	9.85E+08	4065	8.00E+08	5397	9.54E+08
1773	8.72E+08	3099	9.68E+08	4068	7.78E+08	5400	9.55E+08
1887	8.65E+08	3102	9.65E+08	4086	7.66E+08	5403	9.56E+08
1890	6.80E+08	3114	9.58E+08	4092	8.33E+08	5409	9.63E+08
1902	6.98E+08	3183	9.36E+08	4347	9.02E+08	5412	9.82E+08
1905	6.96E+08	3186	8.95E+08	4350	9.22E+08	5466	9.90E+08
1911	7.14E+08	3195	9.08E+08	4476	8.69E+08	5469	9.52E+08
1914	7.26E+08	3216	9.43E+08	4479	8.25E+08	5481	9.79E+08
1917	7.39E+08	3234	9.57E+08	4488	8.77E+08	5484	1.10E+09
1926	7.85E+08	3237	1.01E+09	4491	9.35E+08	5505	1.00E+09
1932	7.99E+08	3261	9.62E+08	4548	8.81E+08	5508	8.59E+08
1947	8.64E+08	3264	9.04E+08	4551	8.60E+08	5520	9.15E+08
1998	9.07E+08	3282	9.38E+08	4584	8.77E+08	5523	1.07E+09
2049	9.66E+08	3288	9.91E+08	4587	8.29E+08	5703	3.82E+08
2091	9.81E+08	3306	9.55E+08	4602	8.71E+08	5706	2.83E+08
2094	9.24E+08	3339	9.07E+08	4629	9.39E+08	5715	4.47E+08
2100	9.24E+08	3354	9.07E+08	4632	9.92E+08	5718	6.09E+08
2139	9.59E+08	3378	9.10E+08	4917	9.18E+08	5943	3.17E+08
2142	9.57E+08	3393	9.11E+08	4920	8.69E+08	5949	2.84E+08
2151	9.65E+08	3408	9.05E+08	4929	8.90E+08	6006	7.40E+08
2154	1.05E+09	3411	8.53E+08	4932	9.53E+08	6009	9.00E+08
2346	8.75E+08	3417	6.51E+08	4950	9.51E+08	6060	7.31E+08
2349	8.65E+08	3420	7.19E+08	4953	8.94E+08	6063	8.81E+08
2352	7.87E+08	3429	8.08E+08	4968	9.02E+08	6084	9.05E+08
2367	8.02E+08	3432	6.66E+08	4974	1.05E+09	6114	8.48E+08
2370	7.97E+08	3435	5.61E+08	4986	1.00E+09	6123	8.34E+08
2373	8.04E+08	3438	5.51E+08	4992	8.77E+08	6129	6.95E+08
2376	8.72E+08	3510	8.35E+08	5001	9.22E+08	6161.4	6.38E+08
2430	9.32E+08	3516	6.92E+08	5004	9.70E+08	6168	6.34E+08
2433	9.59E+08	3519	5.94E+08	5067	9.85E+08	6189	6.32E+08
2652	9.98E+08	3522	5.83E+08	5070	1.02E+09	6192	6.33E+08
2655	1.01E+09	3759	8.94E+08	5124	9.23E+08	6198	7.29E+08
2661	1.00E+09	3762	1.02E+09	5127	9.95E+08	6210	8.25E+08
2664	9.58E+08	3783	9.08E+08	5139	9.60E+08	6231	8.64E+08
2667	9.60E+08	3786	7.83E+08	5145	9.32E+08	6291	8.79E+08
2670	9.76E+08	3817.8	7.92E+08	5148	8.07E+08	6297	8.78E+08
2679	9.83E+08	3819	7.37E+08	5202	9.06E+08	6300	8.76E+08
2682	1.02E+09	3831	7.31E+08	5205	8.71E+08	6342	7.13E+08
2919	9.92E+08	3834	7.66E+08	5217	8.92E+08	6345	7.08E+08
2922	9.77E+08	3891	8.00E+08	5220	1.06E+09	6834	8.14E+08
3030	9.15E+08	3894	8.03E+08	5226	1.04E+09	6840	8.10E+08
3033	8.77E+08	3963	8.19E+08	5229	9.26E+08		
3045	8.95E+08	3966	8.18E+08	5313	7.65E+08		